Tensor network algorithms for three-dimensional quantum systems

Vlaar, P.C.G.

Publication date
2023
Document Version
Final published version


Tensor Network Algorithms
for Three-Dimensional
Quantum Systems
Patrick Vlaar

Tensor Network Algorithms for Three-Dimensional Quantum Systems

UNIVERSITEIT VAN AMSTERDAM

European Research Council

Established by the European Commission

The research presented in this thesis was carried out in the group of dr. P. Corboz at the Institute of Theoretical Physics (ITFA) of the University of Amsterdam (UvA). The research of this doctoral thesis received financial assistance from the European Research Council (ERC) under the European Union's Horizon 2020 research and innovation programme (Grant Agreements No. 677061 and No. 101001604).

ISBN: 978-94-93330-31-3

Tensor Network Algorithms for Three-Dimensional Quantum Systems

ACADEMISCH PROEFSCHRIFT

ter verkrijging van de graad van doctor
aan de Universiteit van Amsterdam
op gezag van de Rector Magnificus
prof. dr. ir. P.P.C.C. Verbeek
ten overstaan van een door het College voor Promoties ingestelde commissie,
in het openbaar te verdedigen in de Agnietenkapel
op woensdag 1 november 2023, te 13.00 uur

door Patrick Cornelis Gerardus Vlaar
geboren te Hoorn

Promotiecommissie

Promotor:	dr. P.R. Corboz	Universiteit van Amsterdam
Copromotor:	prof. dr. J.S. Caux	Universiteit van Amsterdam
Overige leden:	prof. dr. N. Schuch	Universität Wien
	dr. D. Schuricht	Universiteit Utrecht
	prof. dr. C.J.M. Schoutens	Universiteit van Amsterdam
	dr. J. van Wezel	Universiteit van Amsterdam
	dr. C.M.C. de Mulatier	Universiteit van Amsterdam

Faculteit der Natuurwetenschappen, Wiskunde en Informatica

List of Publications

The thesis is based on the following publications:

[1] *Simulation of three-dimensional quantum systems with projected entangled-pair states*
P. C. G. Vlaar and P. Corboz
Physical Review B 103, 205137 (2021)

Presented in Chapter 3

[2] *Efficient tensor network algorithm for layered systems*
P. C. G. Vlaar and P. Corboz
Physical Review Letters 130, 130601 (2023)

Presented in Chapter 4

[3] *Tensor network study of the Shastry-Sutherland model with weak interlayer coupling*
P. C. G. Vlaar and P. Corboz
arXiv:2302.07894 [cond-mat.str-el], (submitted to SciPost Physics)

Presented in Chapter 5

Other publications by the author of this thesis:

[4] *Tapered amplifier laser with frequency-shifted feedback*
A. Bayerle, S. Tzanova, P. Vlaar, B. Pasquiou and F. Schreck
SciPost Physics 1, 2 (2016)

Contents

CHAPTER 1

Introduction

The twentieth century has seen pivotal discoveries in physics that greatly enhanced our understanding of nature at the microscopic level. The theoretical description of Brownian motion [1,2] provided conclusive evidence for the atomic hypothesis, which was followed by the discovery of the atomic nucleus [3] and theoretical descriptions of the atom such as the Bohr model [4]. At the same time, the development of quantum mechanics, and later quantum field theories, led to a groundbreaking new understanding of the microscopic laws of physics. New subatomic fundamental particles were discovered, like quarks and neutrinos [5–7]. Together with the weak- and strong nuclear forces and electromagnetism, these particles constitute the standard model of particle physics, which forms our best description of the microscopic physics of ordinary matter to date.

Despite this detailed understanding of the physical laws that describe individual particles, applying them to the study of many-body systems is far from trivial. A well-known case from classical mechanics is the dynamics of three bodies with known initial position and momenta under gravity, also known as the three-body problem [8]. While the equations of motion are simple to formulate, no closed-form solution is known already for this small system, and it can, moreover, give rise to chaotic behavior. In a similar fashion, to describe materials consisting of many particles ($N \sim 10^{23}$) it is also not difficult to write down Hamiltonians

of relatively broad generality

$$H = \underbrace{-\sum_I \frac{\hbar^2 \vec{\nabla}^2}{2M_I} + \sum_{I<J} \frac{Z_I Z_J}{\left|\vec{R}_I - \vec{R}_J\right|}}_{H_{nucl.}} \underbrace{-\sum_i \frac{\hbar^2 \vec{\nabla}^2}{2m} + \sum_{i<j} \frac{e^2}{|\vec{r}_i - \vec{r}_j|}}_{H_{el.}} \underbrace{+\sum_{iI} \frac{Z_I e}{\left|\vec{R}_I - \vec{r}_i\right|}}_{H_{int.}}, \tag{1.1}$$

with $\vec{R}_I$ ($\vec{r}_i$), M_I (m), and Z_I (e) corresponding to the position, mass, and charge of the ions (electrons), respectively. $H_{nucl.}$ describes the nuclei and the interactions between them, $H_{el.}$ does the same for the electrons, and $H_{int.}$ corresponds to the interactions between the electrons and the nuclei. For simplicity, we ignore attributes like spin. Solving this model in general turns out to be impossible in practice, which necessitates the use of numerous approximations. Furthermore, although the interactions between the individual particles are well understood, their mere number can give rise to new phenomena that are very complex and extremely hard to describe based on these microscopic laws. These effects are referred to as emergent phenomena [9]. Emergence is well-known throughout the sciences and it describes the fact that the laws of meso- or macroscopic systems can be fundamentally different from the laws of the underlying microscopic system. Examples include how the weather is formed from the interactions of individual molecules, how consciousness emerges from the activity of large numbers of neurons, and how swarm behavior arises in flocks of birds or schools of fish. In condensed matter physics, emergent behavior can be found in the form of collective excitations such as skyrmions, superconductivity, the fractional quantum Hall effect, or numerous exotic magnetic phases.

These phenomena can be studied by considering simplified Hamiltonians that only take the dominant interactions in Eq. 1.1 into account. A paradigmatic example is the Hubbard model [10, 11], which is a lattice model valid in the tight-binding limit where the overlap of orbitals at neighboring sites is small. It contains a kinetic hopping term that allows electrons to move between nearest-neighbor sites and an on-site Coulomb repulsion term that gives a positive energy contribution when two electrons are located at the same site. The Hubbard model has very rich physics and it, and its extensions, are commonly used to study quantum magnetism and superconductivity. Despite the many simplifications compared to the general Hamiltonian in Eq. 1.1 it remains a challenging model to solve and many sophisticated theoretical and numerical techniques have been developed to study its properties [12, 13]. In certain limits, it can be reduced further to even simpler Hamiltonians, for example at half-filling in

the limit where the on-site potential term is dominant the model reduces to the spin-1/2 Heisenberg model which we use extensively in this thesis. The Hubbard model can also be formulated with bosonic particles in which case it is known as the Bose-Hubbard model [14].

The range of models that can be solved exactly is relatively small, notable exceptions include the Ising model in one dimension (1D) [15] and two dimensions (2D) [16], and models that allow for a Bethe ansatz solution like the 1D Heisenberg [17, 18] and the 1D Hubbard models [19]. The majority of cases require sophisticated analytical and numerical tools to analyze their properties. For finite systems that are sufficiently small, it is possible to numerically do an exact diagonalization (ED). The obvious benefit of this method is that it provides direct access to many quantities, like the exact eigenstates. The system sizes that can be studied are relatively small, however, due to the exponential growth of Hilbert space d^N with N the number of particles and d the dimension of the local Hilbert space at each lattice site. To achieve larger N, sparse matrices and symmetries can be used, however, the attainable system sizes remain limited. Another commonly used numerical technique is quantum Monte Carlo (QMC) which encompasses a broad family of algorithms based on the Monte Carlo approach, i.e., methods based on random sampling. The quantity that is being sampled differs for the various formulations. The accuracy of these approaches can be systematically improved by increasing the number of samples taken. For fermionic systems and models with frustration negative probabilities arise in QMC methods though, which is known as the negative sign problem. Although workarounds exist for specific models, it has been shown that the problem is NP-hard for the general case [20].

In this thesis, we make use of tensor network methods. The density matrix renormalization group (DMRG) algorithm [21, 22] is the best-known example of a tensor network method. The approach was originally proposed in terms of reduced density matrices, but it was later realized that DMRG can be reformulated in terms of matrix product states (MPS) [23, 24]. The MPS is a variational wave function ansatz consisting of a product of rank-3 tensors, the accuracy of which is systematically controlled by the dimension of the auxiliary space, called the bond dimension. A central role in the success of DMRG is played by entanglement. A broad range of ground states obey a so-called area law in the entanglement entropy [25], i.e., the entanglement entropy between two subsystems scales with their boundary. The MPS ansatz implicitly encodes the 1D area law, which is an important reason for its success in the study of 1D quantum systems.

The projected entangled-pair state (PEPS) [26–30] is a generalization of MPS for higher-dimensional systems. Algorithms for PEPS are significantly more complex than for MPS, but despite this, major progress has been achieved in

the 2D case since their introduction. These developments have turned PEPS into a powerful tool for the study of 2D strongly-correlated systems [31–53]. An important advantage of PEPS, and tensor network methods in general, is that they do not suffer from the negative sign problem. Another benefit is that it is possible to formulate the ansatz in such a way that the thermodynamic limit can be directly studied. This type of ansatz is known as an infinite projected entangled-pair state (iPEPS) [54].

The success of tensor network methods for both 1D and 2D quantum systems raises the question of whether these methods can also be used for the study of three-dimensional (3D) quantum systems. Such methods would be highly desirable to numerically study 3D strongly-correlated systems, such as quantum magnets like the pyrochlore Heisenberg models [55], ultra-cold atoms in optical lattices [56, 57], but also layered 2D systems with a non-negligible interlayer coupling [58–63]. They can also be of interest to high-energy physics, e.g., for lattice gauge theories [64–66].

The main difficulty facing these simulations is that they generally have a significantly higher computational scaling in the bond dimension compared to the algorithms for lower-dimensional systems, which limits the bond dimensions that can be simulated accurately in a reasonable amount of time. For accurate studies of 3D systems, however, lower bond dimensions are typically required compared to the 1D and 2D cases. This is because 3D ground states are typically closer to a product state than their 2D counterparts. One way to understand this is from the monogamy property of entanglement. Let us consider a system consisting of three qubits. When two of these qubits are entangled with each other, the entanglement that they can have with the third qubit is constrained [67]. A similar statement has been proven for systems consisting of N-qubits [68]. For higher-dimensional lattices, the monogamy property suggests that the entanglement between each pair of lattice sites is generally smaller because each site can be entangled with more sites along the different axes of the lattice. As we will show later, the bond dimension determines the maximum amount of entanglement that the iPEPS ansatz can describe. Hence higher dimensional systems generally require a smaller bond dimension.

The main objective of this thesis is to develop iPEPS methods that can be used to simulate ground states of 3D quantum systems. We will develop algorithms both for the study of general 3D models as well as for the subclass of anisotropic 3D systems, which have a weak coupling in one direction. Finally, we will apply the latter method to study the effect of the interlayer coupling in the Shastry-Sutherland model (SSM), which is an effective model for the compound $SrCu_2(BO_3)_2$.

The rest of this thesis is organized in the following way. Chapter 2 gives a

technical introduction to tensor network algorithms, with a focus on (i)MPS and (2D) (i)PEPS. It starts by discussing the area law of entanglement entropy in more detail. After this, we elaborate on several aspects of the 1D MPS ansatz and the canonical form. This is followed by a discussion on the generalization of the MPS to higher dimensions in the form of PEPS. One of the main numerical challenges for PEPS is the evaluation of expectation values, which is treated next for the 2D case. After this, we deal with ground-state algorithms for MPS and PEPS. The chapter ends by treating two practical aspects: incorporating $U(1)$ symmetries into tensor network ansätze to improve computational efficiency and how to perform accurate extrapolations.

In Chap. 3, we focus on iPEPS simulations for general 3D quantum systems, for which we introduce two contraction approaches. In the first approach, only a finite cluster of tensors is contracted exactly, while the rest of the network is considered approximately. The main advantage of this approach is that it allows for an evaluation of the network with a limited computational effort. The second approach performs a full contraction of the network, which is more accurate, but it also comes at a significantly higher numerical cost. The accuracy of the approaches is assessed for the Heisenberg and Bose-Hubbard models through a comparison to QMC and bosonic dynamical mean-field theory (B-DMFT).

After this, Chap. 4 shifts focus to a subset of 3D systems, namely layered 2D systems with weak interlayer coupling. These systems are widely studied, the most famous example being the cuprate high-T_c superconductors [58]. Often these systems are analyzed by ignoring the interlayer coupling such that they can be treated as a 2D problem. The interlayer coupling can, however, play an important role on the quantitative level. We develop a specially designed algorithm to treat these systems that is more efficient than the algorithm for general 3D systems developed in Chap. 3. The method is subsequently benchmarked for the 3D Heisenberg model with anisotropic intra- and interlayer couplings and the dimer singlet to antiferromagnetic Néel state transition in the SSM.

Finally, in Chap. 5, the method from Chap. 4 is used to study the phase diagram of the SSM with interlayer coupling. The SSM is a 2D frustrated spin system, and it is physically remarkably well realized in the compound $SrCu_2(BO_3)_2$. Some discrepancies exist, however. One of these is that the extent of the intermediate plaquette phase in the compound is experimentally measured to be significantly smaller than in the theoretical model [63, 69]. We study the effect of the interlayer coupling on the extent of this phase and find that it disappears already for a coupling around $J''/J \sim 0.04 - 0.05$, which is smaller than predicted in earlier studies based on series expansion (SE) [70]. Additionally, we estimate the interlayer coupling in $SrCu_2(BO_3)_2$ to be around $J''/J \sim 0.027$ at ambient pressure.

CHAPTER 2

Introduction to projected entangled-pair states

In this chapter, we give an overview of tensor network methods with an emphasis on PEPS. In Sec. 2.1, we first explain why tensor networks are especially well-suited to describe ground states for many Hamiltonians, which is related to the area law of entanglement entropy. Then we introduce a diagrammatic notation for tensor networks which is commonly used. Section 2.2 discusses the 1D MPS ansatz and its main properties. A special emphasis is put on a particularly useful gauge of the MPS, which is known as the canonical form. In Sec. 2.3, we introduce the projected-entangled pair states (PEPS), which is a higher-dimensional generalization of the MPS. Contraction methods for 2D PEPS, which are required to evaluate observables, are discussed in Sec. 2.4. Section 2.5 covers algorithms that allow one to find an approximate MPS or PEPS representation of the ground state. We end the chapter by going through some practical considerations for PEPS algorithms. In Sec. 2.6, we explain how to incorporate symmetries into our simulations to improve their numerical efficiency. Finally, in Sec. 2.7 we briefly discuss extrapolations.

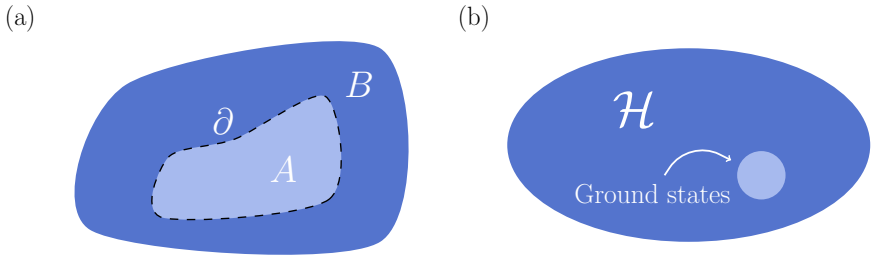

Figure 2.1: (a) Partitioning of a quantum system into two subsystems A and B, with their boundary indicated by ∂. (b) Ground states typically have a significantly smaller entanglement compared to random states. Tensor networks directly target this sector of Hilbert space.

2.1. Preliminaries

2.1.1. Area law

One of the main difficulties in many-body systems is that representing a state quickly becomes problematic for a large number of particles. Let us consider a system consisting of N particles, each having a d-dimensional local Hilbert space. The total Hilbert space of the system is

$$\mathcal{H} = \bigotimes_{k=1}^{N} \mathcal{H}_k, \tag{2.1}$$

where $\mathcal{H}_k$ is the local Hilbert space for particle k. The dimension of this space grows exponentially as d^N. A naive computation shows that already for $N \sim \mathcal{O}(100)$ the required number of basis states becomes larger than the number of atoms in the observable universe. A more efficient representation is thus required.

One property that sets ground states and low-energy states apart is that they are much less entangled than a typical state in Hilbert space. More precisely, for many models it can be shown that ground states satisfy the area law of entanglement entropy [25]. Let us consider a quantum system that we partition into two subsystems A and B, see Fig. 2.1(a). The von Neumann entanglement entropy between A and B is defined as

$$S_{A|B} = -\operatorname{Tr} \rho_A \log \rho_A = -\operatorname{Tr} \rho_B \log \rho_B, \tag{2.2}$$

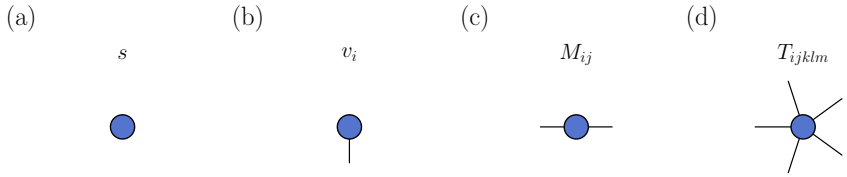

Figure 2.2: Examples of tensors represented in the diagrammatic notation. (a) Scalar s. (b) Vector v_i. (c) Matrix M_{ij}. (d) Rank-5 tensor T_{ijklm}.

where $\rho_{A/B}$ are the reduced density matrices of subsystems A and B, respectively. The area law states that the entanglement entropy S between the subsystems scales as their boundary, i.e., $S \propto \partial$. For example, when a 1D chain is split into two subsystems (that are much longer than the correlation length), S scales as a constant and is thus independent of the number of particles.

For 1D quantum systems, the area law has been proven to hold for local and gapped Hamiltonians [71]. For higher dimensional systems, proofs of area law behavior are much more limited. The area law is widely believed to hold for local and gapped Hamiltonians in higher dimensions too, however [25]. Critical systems can have a mild logarithmic violation of the area law. This is known to be the case for models in 1D [72, 73] and for some models in higher dimensions.

The MPS and PEPS ansätze by construction satisfy the 1D and higher-dimensional area laws, respectively. This means that they can directly target the region of Hilbert space that is relevant for ground states and low-energy states, see Fig. 2.1(b). This property makes them especially well-suited to describe these states, and it is an important reason for their success.[1]

2.1.2. Diagrammatic notation

Equations in the field of tensor networks can quickly become unwieldy, therefore they are commonly represented by diagrams instead. In this language, a shape represents a tensor while its indices are indicated by lines connecting to the shape. Figures 2.2(a)-(d) show examples of a scalar, a vector, a matrix, and a rank-5 tensor, respectively. By connecting the lines of two shapes a summation over the respective index is implied, as is shown in Fig. 2.3(a) for a matrix-vector multiplication. Some mathematical properties become immediately transparent

[1] Other types of tensor network ansätze also exist, such as the multiscale entanglement renormalization ansatz (MERA) [74, 75] (which can describe logarithmic corrections to the area law) and tree tensor networks (TTN) [76]. These ansätze are outside the scope of this thesis.

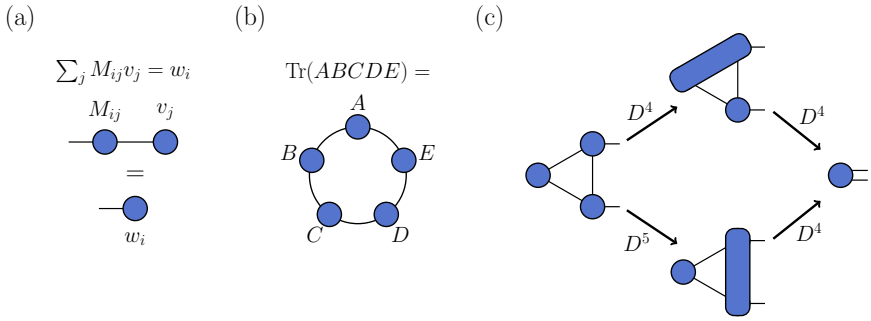

Figure 2.3: Contractions in the diagrammatic notation. (a) A matrix-vector multiplication. When a line connects two objects a summation is implied. (b) A trace over 5 matrices. (c) It is important to choose the contraction order with the lowest computational cost. When we assume the dimension of each index is D, the contraction path at the top has a dominant scaling of $\mathcal{O}(D^4)$, which is preferable to the contraction order on the bottom which scales as $\mathcal{O}(D^5)$.

through this language, such as the cyclic property of the trace which is shown in Fig. 2.3(b). In our algorithms, we make use of the NCON function [77] to contract diagrams. Note that the order in which a contraction is done can have a significant impact on the computational scaling, as can be seen in the example in Fig. 2.3(c). Assuming that the dimension of each index is D, two contraction paths can be found with a dominant computational scaling of either $\mathcal{O}\left(D^5\right)$ or $\mathcal{O}\left(D^4\right)$, the latter being preferable. For complex diagrams, determining the optimal contraction order can be difficult to determine by hand. For such cases, algorithms like NETCON [78] can be used to find the optimal order.

2.2. Matrix product state

The most famous example of a tensor network ansatz is the matrix product state (MPS) [22–24]. The MPS lies at the basis of many powerful numerical methods, including the DMRG approach [21], the time-evolving block decimation (TEBD) method [79, 80], and the variational unitary matrix product state (VUMPS) algorithm [81]. In this section, we discuss some of its main properties and core concepts that are important for later sections as well.

Let us consider a chain consisting of N sites with open boundary conditions.

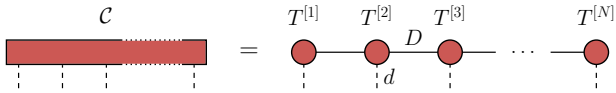

Figure 2.4: An MPS ansatz represents the wave function coefficient $\mathcal{C}_{s_1 s_2 \ldots s_N}$ as a trace over a product of tensors $T^{[i]}$. The initial tensor $T^{[1]}$ and final tensor $T^{[N]}$ are rank-2 tensors, while the others are rank-3 tensors. The physical legs, corresponding to the local Hilbert spaces, are indicated by dashed lines, while solid lines represent virtual bonds.

The wave function of this system can, in general terms, be written as

$$|\psi\rangle = \sum_{s_1 s_2 \ldots s_N} \mathcal{C}_{s_1 s_2 \ldots s_N} |s_1 s_2 \ldots s_N\rangle \,, \tag{2.3}$$

in which s_i corresponds to the local basis states at site i of a d-dimensional Hilbert space and $\mathcal{C}_{s_1 s_2 \ldots s_N}$ is a coefficient assigning a weight to each basis state of the full system. An MPS is a variational wave function ansatz in which the coefficient in Eq. 2.3 is represented by a product of tensors

$$\mathcal{C}_{s_1 s_2 \ldots s_N} = \sum_{a_1 a_2 \ldots a_{N-1}} \left(T^{[1]}\right)^{a_1}_{s_1} \left(T^{[2]}\right)^{a_1 a_2}_{s_2} \cdots \left(T^{[N]}\right)^{a_{N-1}}_{s_N} , \tag{2.4}$$

with $T^{[i]}$ a tensor at site i. In the diagrammatic notation, this MPS can be written as shown in Fig. 2.4. The dashed, vertical lines correspond to the local d-dimensional Hilbert space of each site, and they are called physical indices. Note that each coefficient, which is obtained when the physical index at each site is fixed, is given by a product of matrices (with vectors at the open boundaries), hence the name matrix product states. The horizontal lines connecting the tensors with each other are called virtual bonds, and they introduce an auxiliary space with dimension D, which is called the bond dimension. For example, for $D = 1$ the ansatz corresponds to a product state. The size of the bond dimension can be varied to systematically control the accuracy of the ansatz.

An advantage of MPS is that it is possible to directly represent a wave function in the thermodynamic limit by choosing a supercell of tensors and repeating it infinitely many times. This type of MPS is also known as an infinite matrix product state (iMPS). For example, an iMPS with a supercell consisting of two tensors T^A and T^B results in a coefficient

$$\mathcal{C} = \mathrm{Tr}\Big(\ldots T^A_{s_{2n}} T^B_{s_{2n+1}} T^A_{s_{2(n+1)}} T^B_{s_{2(n+1)+1}} \ldots\Big), \tag{2.5}$$

where n counts the supercells. It is worth mentioning that for gapped systems, thanks to the supercell, the number of variational parameters of an iMPS is typically significantly smaller than for a finite MPS.

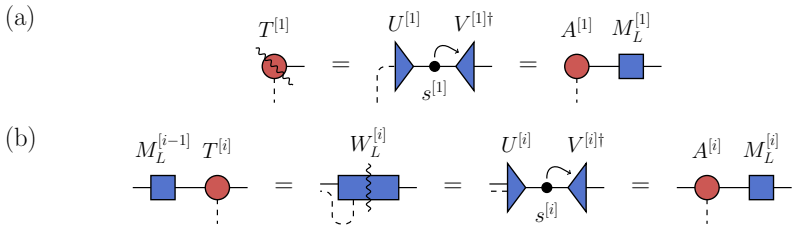

Figure 2.5: The procedure to make the left-hand side of the MPS orthogonal, as required in the Schmidt decomposition. (a) The transformation of the first tensor $T^{[1]}$ using an SVD. (b) M_L is moved from the left-hand side of tensor $T^{[i]}$ to the right-hand side, while transforming the tensor into $A^{[i]}$.

2.2.1. Canonical form

An MPS representation of a state is not unique. This can easily be seen by introducing an identity $M^{-1}M = \mathbb{I}$ on one of the virtual bonds of the MPS and by absorbing M^{-1} into the tensor on the left-hand side and M into the tensor on the right-hand side. This gives us a different MPS without changing the state it represents, an MPS thus has a large gauge freedom. In this section, we will show how an MPS can be transformed into a gauge called the canonical form which has some particularly useful properties.

Let us start by discussing the Schmidt decomposition. Imagine that we have the state from Eq. 2.3, and we want to partition it into two sides A and B around bond n (between sites n and $n+1$). The Schmidt decomposition of this state around bond n is given by

$$|\psi\rangle = \sum_k \lambda_k^{[n]} |a_k\rangle_{s_1 s_2 \ldots s_n} |b_k\rangle_{s_{n+1} \ldots s_N} , \tag{2.6}$$

with $\lambda_k^{[n]}$ the Schmidt coefficients, and $|a_k\rangle_{s_1 s_2 \ldots s_n}$ and $|b_k\rangle_{s_{n+1} \ldots s_N}$ forming orthonormal bases for A and B, respectively. It is possible to directly obtain the Schmidt decomposition by performing a singular value decomposition (SVD) on the wave function coefficient from Eq. 2.3. We first reshape the coefficient into a matrix by combining the physical legs $s_1 \ldots s_n$ and $s_{n+1} \ldots s_N$ into two legs, and then we perform an SVD

$$\mathcal{C}_{s_1 \ldots s_n, s_{n+1} \ldots s_N} = U s V^\dagger, \tag{2.7}$$

with U and V unitary matrices and s a diagonal matrix with positive entries called singular values. We use the convention that the singular values in s are sorted by decreasing magnitude. By identifying $\lambda = s$, $|a\rangle = U$, and $|b\rangle = V^\dagger$ we obtain Eq. 2.6.

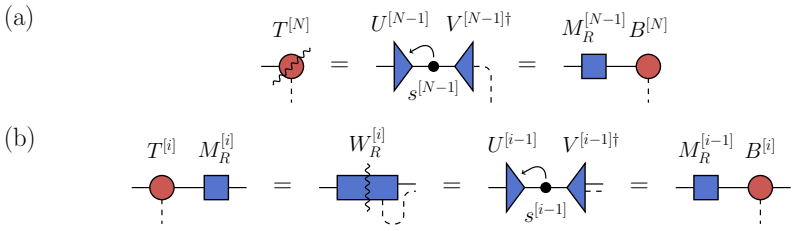

Figure 2.6: The method to make the right-hand side of the chain orthogonal as required in the Schmidt decomposition. (a) The final tensor $T^{[N]}$ is transformed to an orthogonal tensor $B^{[N]}$ using an SVD. (b) M_R is moved from the right-hand side of tensor $T^{[i]}$ to the left-hand side. The tensor $T^{[i]}$ becomes $B^{[i]}$.

We would now like to transform the MPS in Eq. 2.4 to this form as well. Let us start by considering the left-hand side of the chain. An SVD of tensor $T^{[1]}$ allows us to rewrite it as

$$T^{[1]} = U^{[1]} s^{[1]} V^{[1]\dagger} = A^{[1]} M_L^{[1]}, \tag{2.8}$$

where $A^{[1]} = U^{[1]}$ and $M_L^{[1]} = s^{[1]} V^{[1]\dagger}$, see also Fig. 2.5(a). Note that, since $U^{[1]}$ is unitary, $A^{[1]\dagger} A^{[1]} = \mathbb{I}$.

We can now move M_L through the MPS until we reach bond $n-1$. In Fig. 2.5(b), we show how M_L can be moved from the left-hand side of tensor $T^{[i]}$ at site i to the right-hand side. We start by applying $M_L^{[i-1]}$ to $T^{[i]}$

$$M_L^{[i-1]} T^{[i]} = W_L^{[i]}, \tag{2.9}$$

where $W_L^{[i]}$ is a $D \times D \times d$ tensor, which we can reshape to a $dD \times D$ matrix $W_L^{[i]}$ by combining the physical and left-side virtual legs into one. This allows us to perform an SVD

$$W_L^{[i]} = U^{[i]} s^{[i]} V^{[i]\dagger} = A^{[i]} M_L^{[i]}, \tag{2.10}$$

where $A^{[i]}$ is obtained by reshaping $U^{[i]}$ back into a $D \times D \times d$ tensor and $M_L^{[i]} = s^{[i]} V^{[i]\dagger}$. This process can be iterated until we arrive at the desired bond. In the following, reshaping before and after SVDs is done implicitly.

A similar procedure can be used on the right-hand side of the MPS. First, we perform an SVD on the final tensor

$$T^{[N]} = U^{[N-1]} s^{[N-1]} V^{[N-1]\dagger} = M_R^{[N-1]} B^{[N]}, \tag{2.11}$$

with $M_R^{[N-1]} = U^{[N-1]} s^{[N-1]}$ and $B^{[N]} = V^{[N-1]\dagger}$, as is shown in Fig. 2.6(a). After this, we move M_R to the left through the MPS until we reach bond $n+1$

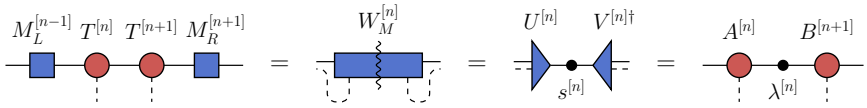

Figure 2.7: After M_L and M_R have been moved to the center, a final transformation using an SVD is necessary to bring the MPS to a Schmidt decomposition.

by iterating

$$T^{[i]}M_R^{[i]} = W_R^{[i]} = U^{[i-1]}s^{[i-1]}V^{[i-1]\dagger} = M_R^{[i-1]}B^{[i]}, \tag{2.12}$$

with $M_R^{[i-1]} = U^{[i-1]}s^{[i-1]}$ and $B^{[i]} = V^{[i-1]\dagger}$, see Fig. 2.6(b).

After we move M_L and M_R towards the desired bond, a special treatment is required at bond n itself

$$M_L^{[n-1]}T^{[n]}T^{[n+1]}M_R^{[n+1]} = W_M^{[n]} = U^{[n]}s^{[n]}V^{[n]\dagger} = A^{[n]}s^{[n]}B^{[n+1]}, \tag{2.13}$$

where $A^{[n]}$ and $B^{[n+1]}$ correspond to the unitaries $U^{[n]}$ and $V^{[n]\dagger}$ reshaped back into rank-3 tensors, see Fig. 2.7.

We have now transformed the MPS into a Schmidt decomposition. To see this, we first note that, because $A^{[i]}$ and $B^{[j]}$ correspond to unitary matrices from the SVD decomposition, they obey the conditions

$$A^{[i]\dagger}A^{[i]} = \mathbb{I}, \tag{2.14}$$

$$B^{[j]}B^{[j]\dagger} = \mathbb{I}, \tag{2.15}$$

for $i \in 1, \ldots, n$ and $j \in n+1, \ldots, N$, as shown in Fig. 2.8. These conditions imply that the bases of A and B in Eq. 2.6 can be identified as $|a\rangle = A^{[1]} \ldots A^{[n]} |s_1 \ldots s_n\rangle$ and $|b\rangle = B^{[n+1]} \ldots B^{[N]} |s_{n+1} \ldots s_N\rangle$, which are orthonormal. The singular values $s^{[n]}$ can be identified with the Schmidt coefficients $\lambda^{[n]}$. An MPS forming a Schmidt decomposition around bond n is also called canonical around this bond.

There are several motivations why it is convenient to write an MPS in this form. A first motivation is that computing local observables simplifies considerably. As an example, consider computing the expectation value of a one-site observable at site n, $\langle\psi|O_n|\psi\rangle$, which is shown in Fig. 2.9. Using the conditions in Eqs. 2.14 and 2.15 starting from the first and final tensors we reduce the computation to the contraction of the diagram on the right side in Fig. 2.9, thus simplifying the contraction significantly.

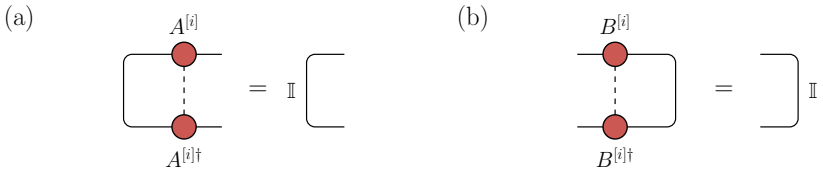

Figure 2.8: The conditions obeyed by the tensors in an MPS when it is in canonical form. (a) The left-canonical condition from Eq. 2.14. (b) The right-canonical condition from Eq. 2.15.

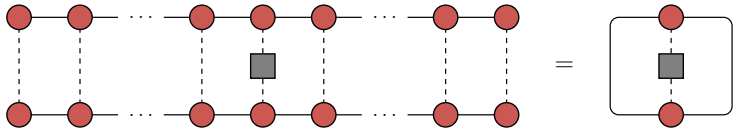

Figure 2.9: The computation of a one-site observable $\langle\psi| O_n |\psi\rangle$ at site n. This contraction simplifies significantly to the diagram on the right by making use of the canonical conditions from Eqs. 2.14 and 2.15.

A second motivation for writing the MPS as a Schmidt decomposition is that it provides direct access to the reduced density matrices

$$\rho_A = \sum_k \lambda_k^2 |a_k\rangle \langle a_k| \qquad \rho_B = \sum_k \lambda_k^2 |b_k\rangle \langle b_k| . \tag{2.16}$$

From these, quantities like the von Neumann entanglement entropy can be directly computed

$$S_{A|B} = -\operatorname{Tr} \rho_A \log \rho_A = -\sum_k \lambda_k^2 \log\big(\lambda_k^2\big). \tag{2.17}$$

When we choose the Schmidt coefficients in such a way that they are all equal (but normalized), $\lambda_k = 1/\sqrt{D}$, we see that the maximum amount of entanglement entropy for the bipartition of the MPS is $S = \log(D)$. The entanglement entropy thus is independent of N and we find that the ansatz satisfies the 1D area law. For models that are local and gapped, the ground state can be approximated well by an MPS with a non-diverging D.

A final motivation for writing the MPS in the form of a Schmidt decomposition is that it allows one to truncate a bond to a lower bond dimension

$$|\psi\rangle = \sum_{k=1}^{D} \lambda_k |a_k\rangle |b_k\rangle \approx \sum_{k=1}^{D'<D} \lambda_k |a_k\rangle |b_k\rangle , \tag{2.18}$$

with $D' < D$. It can be shown that this provides the optimal rank-D' approximation of the rank-D wave function in the Frobenius norm. Truncations of MPS play an important role in numerical algorithms, as we will see later.

Canonical form around other bonds

In the previous part of this section, we have explained how the canonical form around bond n can be obtained. To obtain the canonical form around another bond, $\lambda^{[n]}$ can be shifted through the MPS in a similar way to how M_L and M_R are moved to the right (Eqs. 2.9 and 2.10) and left (Eq. 2.12), respectively, until we reach the desired bond. It is, however, also possible to use a more convenient notation, that was introduced by Vidal [79], in which this transformation is not necessary. To convert the MPS to this notation we make use of the singular value matrices which were obtained from the transformation of the MPS to the canonical form in Eqs. 2.8-2.12. We introduce the identities $s^{[i]} \left(s^{[i]}\right)^{-1} = \mathbb{I}$ and $\left(s^{[i]}\right)^{-1} s^{[i]} = \mathbb{I}$ on bonds to the left and right of bond n, respectively. We then rewrite

$$s^{[i-1]} \left(s^{[i-1]}\right)^{-1} A^{[i]} = \lambda^{[i-1]} \Gamma^{[i]}, \tag{2.19}$$

$$B^{[i]} \left(s^{[i]}\right)^{-1} s^{[i]} = \Gamma^{[i]} \lambda^{[i]}, \tag{2.20}$$

where $\Gamma^{[i]} = \left(s^{[i-1]}\right)^{-1} A^{[i]}$ or $\Gamma^{[i]} = B^{[i]} \left(s^{[i]}\right)^{-1}$ and $\lambda^{[i]} = s^{[i]}$. The resulting MPS is shown in Fig. 2.10(a). The canonical conditions in Eqs. 2.14 and 2.15 become

$$\Gamma^{[i]\dagger} \left(\lambda^{[i-1]}\right)^2 \Gamma^{[i]} = \mathbb{I}, \tag{2.21}$$

$$\Gamma^{[i]} \left(\lambda^{[i]}\right)^2 \Gamma^{[i]\dagger} = \mathbb{I}, \tag{2.22}$$

which are also shown in Figs. 2.10(c)-(d).[2] The diagram for the computation of the one-site observable in Fig. 2.9 transforms to the diagram in Fig. 2.10(b). When an MPS is put in this form every possible partition is in a Schmidt decomposition with Schmidt coefficients $\lambda^{[i]}$.

Canonical form for iMPS

Let us now discuss how an iMPS can be converted to a canonical form. In this case, it is not possible to follow the method discussed before because of the

[2] Note that for the first and final tensor we have $\Gamma^{[1]} = A^{[1]}$ and $\Gamma^{[N]} = B^{[N]}$. They still obey the conditions $\Gamma^{[1]\dagger}\Gamma^{[1]} = \mathbb{I}$ and $\Gamma^{[N]}\Gamma^{[N]\dagger} = \mathbb{I}$.

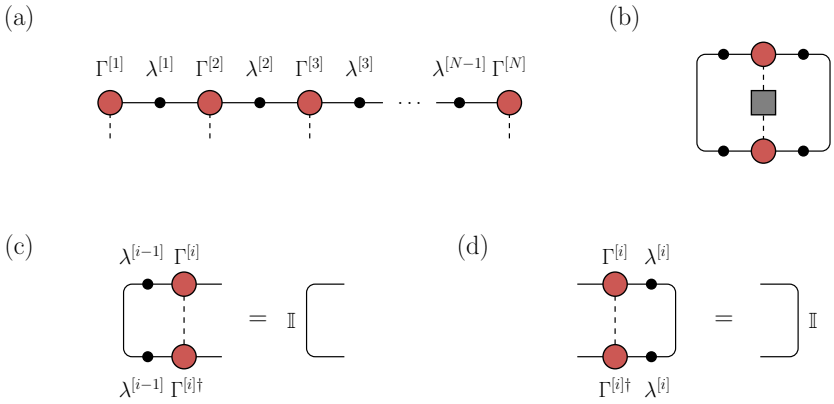

Figure 2.10: (a) The MPS from Eq. 2.4 is represented in the notation introduced in Eqs. 2.19 and 2.20. (b) The contraction from Fig. 2.9 is represented in this notation. (c) The left-canonical condition from Eq. 2.21. (d) The right-canonical conditions from Eq. 2.22.

absence of a first and final tensor. Therefore, a different procedure must be used to transform it to a canonical form, i.e., to make it satisfy Eqs. 2.21 and 2.22. This can be achieved by following the procedure from Ref. [82], which we will discuss in more detail. Note that alternative schemes exist like Ref. [83].

Let us assume the iMPS has a supercell containing one tensor Γ with a singular value matrix λ on the bond. The method consists of iterating the following steps, which are also shown in Fig. 2.11:

(i) Compute the diagram shown on the left-hand side of Fig. 2.11(a). When the iMPS is non-canonical this gives a matrix $v_L \neq \mathbb{I}$. We then perform an eigendecomposition

$$v_L = W_L D_L W_L^\dagger = X_L^\dagger X_L, \tag{2.23}$$

where we identify $X_L^\dagger = W_L \sqrt{D_L}$. On the right-hand side we follow a similar procedure, shown in Fig. 2.11(b), i.e., $v_R = W_R D_R W_R^\dagger = X_R X_R^\dagger$ with $X_R = W_R \sqrt{D_R}$.

(ii) Now we can insert the identities $\left(X_L^T\right)^{-1} X_L^T = \mathbb{I}$ and $X_R X_R^{-1} = \mathbb{I}$ into the iMPS bonds in the way shown in Fig. 2.11(c). We then can take an SVD of

$$X_L^T \lambda X_R = U \tilde{\lambda} V^\dagger, \tag{2.24}$$

with $\tilde{\lambda}$ the new singular value matrix. We obtain the new tensor $\tilde{\Gamma}$ by contracting the diagram in Fig. 2.11(d).

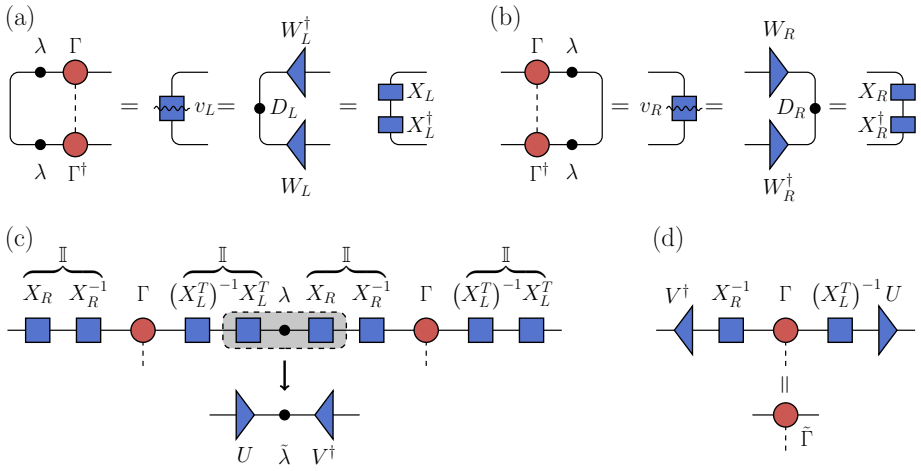

Figure 2.11: The steps described in Ref. [82] to convert an iMPS to satisfy the canonical form conditions in Eqs. 2.21 and 2.22, as described in the main text. (a) The first step of the process consists of computing the matrix X_L through an eigendecomposition of the left-canonical condition. (b) The same procedure is followed as in (a) starting from the right-canonical condition. (c) The identities $\left(X_L^T\right)^{-1} X_L^T$ and $X_R X_R^{-1}$ are inserted into the virtual bonds, and an SVD is done. This gives the updated singular value matrix $\tilde{\lambda}$. (d) The updated tensor $\tilde{\Gamma}$ is computed by contracting the given diagram.

These steps are iterated until the canonical conditions in Eqs. 2.21 and 2.22 are sufficiently satisfied.

2.3. Projected entangled-pair states

Because of the success of MPS in 1D, attempts were made early on to apply it to 2D systems [84, 85]. A common way to do this is to take a finite-width cylinder and wrap the MPS around it, as shown in Fig. 2.12(a). Interactions with sites that are not connected directly through the MPS are treated as further-neighbor couplings. By performing a careful extrapolation in the cylinder width, it is often possible to make a reliable approximation of the result in the thermodynamic limit [86].

An important benefit of this approach is that the properties that make MPS so convenient to use in 1D, like the canonical form, are still present in 2D. The

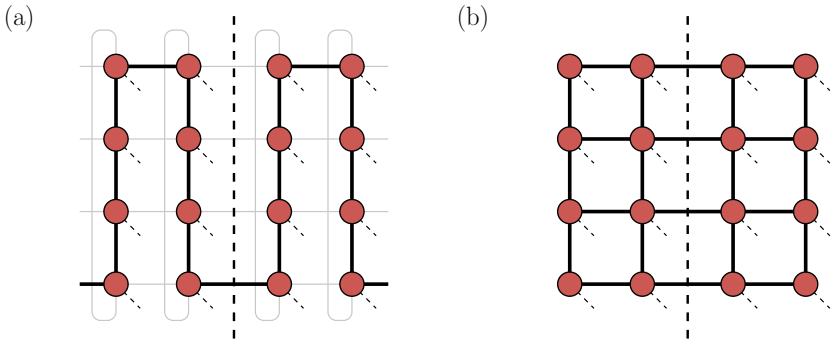

Figure 2.12: Tensor network ansätze in 2D. (a) A "snake" MPS ansatz is shown for a cylinder of width $L_y = 4$. The black lines correspond to the virtual bonds of the MPS, while the gray lines indicate the nearest-neighbor couplings that must be encoded by further-neighbor interactions in the MPS ansatz. For a partition of the system along the dashed line, the interactions are carried over one MPS bond. (b) A 4×4 PEPS is given in which each tensor is directly connected to all its nearest-neighbor tensors through a virtual bond. A partition between the left- and right-hand sides of the state, indicated by the dashed line, shows that the number of cut PEPS bonds scales with the length of the boundary, in correspondence with the 2D area law.

method does come with a significant drawback though. Ground states of 2D quantum systems are expected to satisfy the 2D area law, i.e., when we consider a system of size $L_x \times L_y$ and divide it into two subsystems in the way shown in Fig. 2.12(a), the entanglement entropy should scale with the length of the boundary L_y. The MPS, however, is an intrinsically 1D ansatz satisfying the 1D area law, i.e., for the partition in Fig. 2.12(a), the maximal entanglement entropy that the MPS can reproduce is $S = \log(D)$, independent of the cylinder width. As a consequence, to keep a fixed accuracy, it is necessary to scale the bond dimension exponentially with the width of the cylinder [84]. This severely limits the cylinder widths that can be studied reliably. Despite these limitations, MPS have proven to be a successful tool to study challenging 2D systems, see, e.g., Refs. [87–90].

A more natural ansatz for higher-dimensional systems is the projected entangled-pair state (PEPS) [29, 30] (also known as tensor product state [26–28]). The PEPS is a variational ansatz that generalizes the 1D MPS to higher dimensions, and it is defined as

$$|\psi\rangle = \sum_{s_1 \ldots s_N = 1}^{d} \mathrm{Tr}\left(T_{s_1}^{[\vec{r}_1]} \ldots T_{s_N}^{[\vec{r}_N]} \right) |s_1 \ldots s_N\rangle \,, \tag{2.25}$$

with $T_{s_i}^{[\vec{r}_i]}$ corresponding to a tensor at site $\vec{r}_i$ and with s_i denoting the basis states of the local Hilbert space. In this chapter, we limit ourselves to 2D square lattices. Figure 2.12(b) shows an example of a 4×4 PEPS ansatz. Each (central) tensor has five indices, four virtual indices connecting the tensors in a square pattern and one physical index connecting to the local Hilbert space. The accuracy of the ansatz is again controlled by the bond dimension D of the virtual indices. Similar to the MPS case, it is possible to directly represent states in the thermodynamic limit by infinitely repeating a supercell of tensors which is known as an infinite projected entangled-pair state (iPEPS) [54].

The most important difference between PEPS and MPS is that PEPS satisfy the higher-dimensional area law. When we consider the examples in Fig. 2.12, we see that for a partition of the MPS in Fig. 2.12(a) the entanglement entropy did not scale with the system size, while for the cut of the PEPS in Fig. 2.12(b) we have $S \propto \mathcal{O}(L_y \log(D))$. This property strongly suggests that PEPS are better suited to describe gapped ground states of two- or higher-dimensional models.

A second difference is that PEPS can describe polynomially decaying correlations [91], which are characteristic of certain types of critical points. This is in contrast to MPS, which can only represent exponential decay.

The final difference between MPS and PEPS that we want to mention here is that no canonical form is known for PEPS, which is due to the presence of loops in the ansatz. These loops make it impossible to define a Schmidt decomposition by cutting one bond as in the MPS case. Note that loops already arise in 1D MPS when periodic boundary conditions are introduced, which make it impossible to partition the MPS when cutting one bond. This is an important reason why it is preferable to do MPS simulations with open boundary conditions. The absence of a canonical form makes performing contractions or truncations of the PEPS ansatz significantly more challenging in numerical algorithms.

In past decades, there has been substantial progress in the development of efficient approximate contraction approaches, however, which have allowed PEPS to become a very competitive tool for the simulation of strongly-correlated 2D quantum systems. In the next section, several families of these approaches are discussed in detail.

2.4. Contraction of iPEPS

To evaluate expectation values of an (i)PEPS, it is necessary to contract the corresponding network. Unlike the MPS case, however, where we can make use

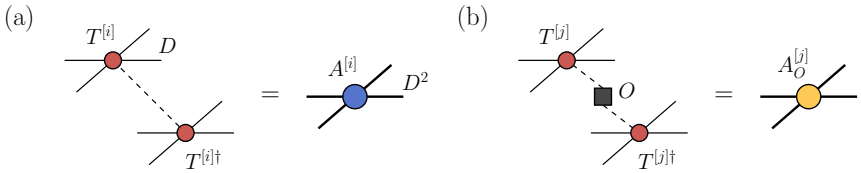

Figure 2.13: (a) The norm tensor is obtained by contracting over the physical leg of a tensor. In each direction, the legs are combined into one leg with bond dimension D^2. (b) A one-site observable can be computed by replacing the norm tensor at the desired location with a tensor that has an operator applied to the physical leg.

of the canonical form, the exact contraction of a PEPS scales exponentially with the number of tensors. To be more precise, it has been proven that contractions of PEPS belong to the #P-complete complexity class [92]. To evaluate a PEPS, we therefore rely on methods that perform the contraction approximately.

In this section, we consider the evaluation of the norm $\langle\psi|\psi\rangle$, with $|\psi\rangle$ a square lattice iPEPS. To simplify the discussion, we define a norm tensor which is obtained by contracting the physical leg at each site. For site i, the norm tensor is defined as

$$A^{[i]} = \sum_{s_i} T^{[i]}_{s_i} \otimes T^{[i]\dagger}_{s_i}, \tag{2.26}$$

see Fig. 2.13(a). This gives us a 2D network. Note that an observable $\langle\psi| O |\psi\rangle$ can be computed by inserting O before contracting the physical legs. For example, a one-site observable at site j can be evaluated by replacing the norm tensor $A^{[j]}$ by

$$A^{[j]}_O = \sum_{s_j s'_j} \left(T^{[j]}_{s_j} O_{s_j s'_j} \right) \otimes T^{[j]\dagger}_{s'_j}, \tag{2.27}$$

which is shown in Fig. 2.13(b).

2.4.1. Corner transfer matrix renormalization group

The first contraction approach that we discuss is the corner transfer matrix renormalization group method (CTM). The CTM formalism was introduced by Baxter [93] in the context of 2D classical statistical mechanics problems, and it was later adapted by Nishino and Okunishi [94] to numerically contract 2D classical partition functions. The CTM procedure approximates the environment around a specific site by corner and edge tensors, representing quadrants and half-rows of the network, respectively, see Fig. 2.14. By varying the bond

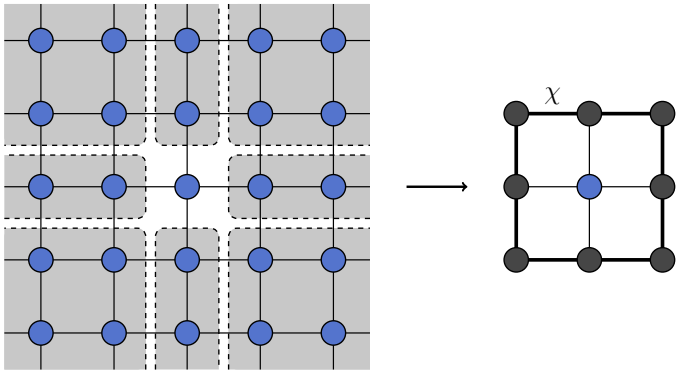

Figure 2.14: The general idea of the CTM is to approximate each quadrant of the tensor network by a corner tensor and each half-row by an edge tensor. The accuracy is controlled through the boundary bond dimension χ.

dimension of the environment tensors χ, the accuracy of the contraction can be systematically controlled.

Various versions of the CTM exist. Let us first discuss the version originally introduced by Nishino and Okunishi [94] to establish the main idea. We consider the contraction of a network consisting of one tensor A with real entries that obeys rotational and mirror symmetry. These symmetries allow us to only use one corner tensor C and one edge tensor T in all directions. The corner and edge tensors can be obtained with an iterative procedure:

(i) The corner is enlarged by absorbing a row and column in the way shown on the left-hand side of Fig. 2.15, which we call $\tilde{C}$. This increases the bond dimension of the corner to $D^2\chi \times D^2\chi$. Note that $\tilde{C}$ is symmetric.

(ii) An eigendecomposition of the enlarged corner is done

$$\tilde{C} = WDW^T \approx W'D'W'^T, \tag{2.28}$$

with D a diagonal matrix containing the eigenvalues and W a matrix with the orthonormal eigenvectors, see Fig. 2.15. We approximate W and D by W' and D', respectively, which are obtained by keeping only the largest χ eigenvalues.

(iii) The renormalized corner C' and edge T' tensors are obtained by inserting the approximate identities $W'W'^T \approx \mathbb{I}$ on the enlarged bonds in the way shown in Figs. 2.16(a) and 2.16(b), respectively. The W' and W'^T tensors act as projectors to reduce the bond dimension of C' to $\chi \times \chi$.

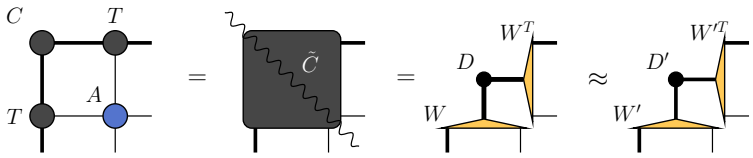

Figure 2.15: To obtain the projectors that renormalize the enlarged corner $\tilde{C}$ in the CTM algorithm, an eigendecomposition of the enlarged corner is performed. Only the χ largest magnitude eigenvalues are kept, as is shown in the final step.

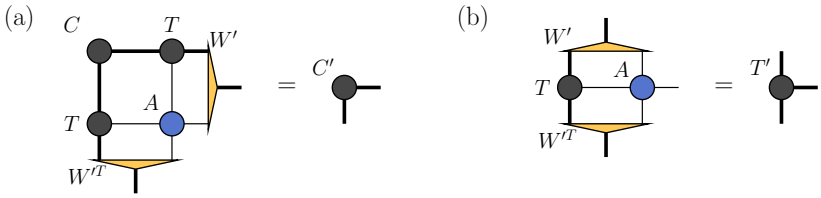

Figure 2.16: The CTM tensors are renormalized by inserting approximate identities $W'W'^T \approx \mathbb{I}$ on the enlarged bonds. (a) The renormalized corner tensor. (b) The renormalized edge tensor.

Note that the corner tensor reduces to $C' = D'$. These steps are iterated until convergence is reached.

Although this version of the CTM is simple and efficient, it can unfortunately not be applied to more general iPEPS which do not have symmetric tensors, and which can consist of larger supercells. In the rest of this thesis, we therefore make use of the directional CTM method which was introduced in Ref. [95]. Instead of updating all the environment tensors at the same time, the idea of the directional CTM is to iteratively perform an update over each axis of the network independently. As an illustration, we consider a left move which is shown in Fig. 2.17. The left move consists of the following steps:

(i) Insert a column on the left-hand side of the network.

(ii) Absorb the additional column into the boundary tensors. This gives us enlarged environment tensors on the left-hand side with a bond dimension in the vertical direction of χD^2.

(iii) To avoid exponential growth of the bond dimension we insert projectors to truncate the vertical bonds back to χ.

Similar moves are done in the right-, up-, and down-directions which together complete one update iteration. The iterations are repeated until sufficient con-

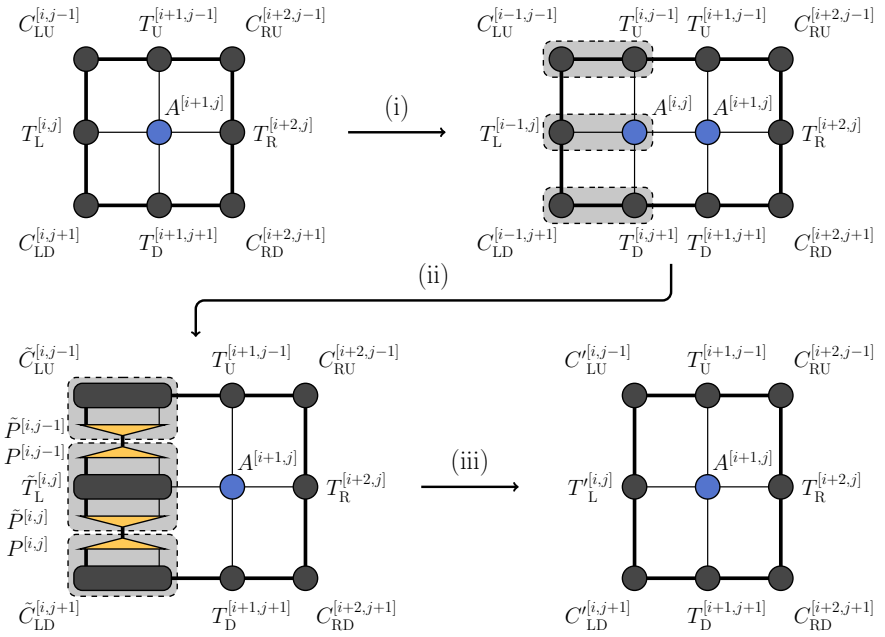

Figure 2.17: A left move in the directional CTM. In step (i), a column is inserted on the left. This column is contracted into the boundary tensors on the left in step (ii) to form enlarged corner- and edge tensors. Finally, in step (iii), we introduce projectors to truncate the environment bond dimension down from $D^2\chi \to \chi$. This gives the updated corner and edge tensors.

vergence is obtained.

A critical component of the algorithm is the method used to choose the projectors. No unique way exists to determine them, and several schemes have been proposed [32, 95–97]. We will employ the commonly used method developed in Ref. [32]. A diagrammatic overview of the approach is given in Fig. 2.18 for the projectors used in the left move. The projectors are computed based on a 2×2 cell of tensors with their corresponding environment tensors as shown in Fig. 2.18(a). The diagram is split at the bond that needs to be truncated and on the opposite side of the diagram, and a QR decomposition is performed on both halves.[3] We then compute the SVD of $R\tilde{R}$

$$R\tilde{R} = UsV^\dagger \approx U's'V'^\dagger, \tag{2.29}$$

where we keep only the χ largest singular values, as can be seen in Fig. 2.18(b).

[3]Note that the QR decomposition that is used here is not necessarily required [98].

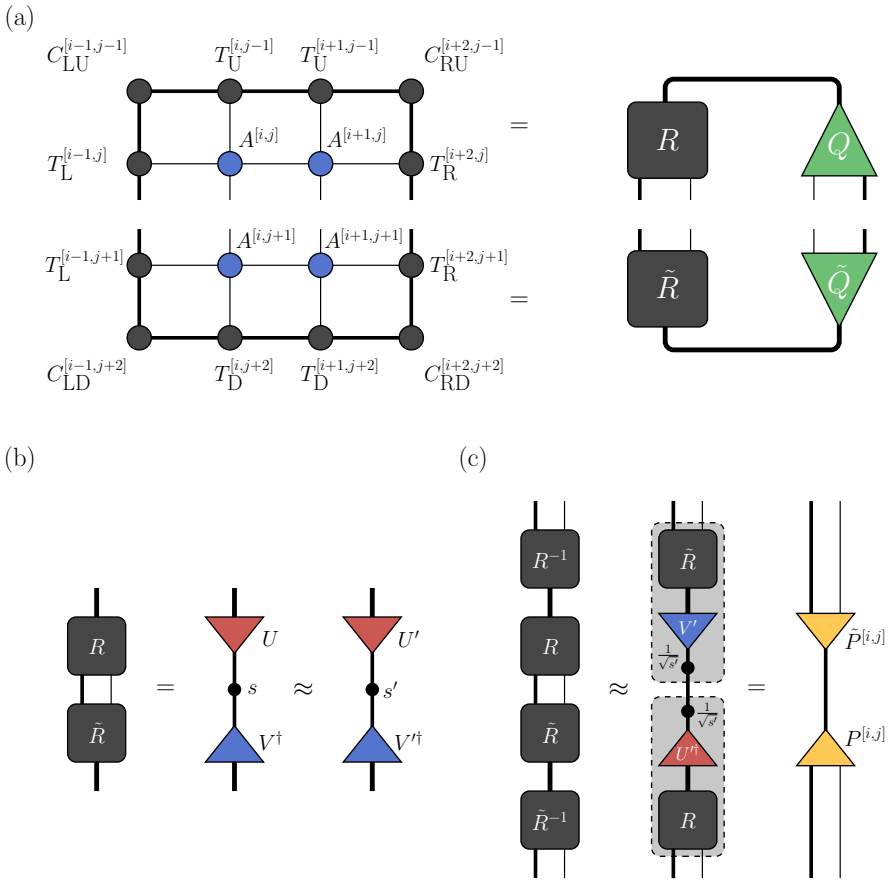

Figure 2.18: Computation of the projectors for a left move in the directional CTM method, as discussed in the main text. (a) A 2×2 cell with its environment is split into an upper and lower half. On each half, a QR decomposition is performed. (b) An SVD of $R\tilde{R}$ is done, and only the χ largest singular values are kept. (c) An approximate identity is inserted into the bond that is being truncated. The projectors $\tilde{P}$ and P are used to renormalize the enlarged bond.

Using the SVD tensors, the projectors are obtained by inserting an approximate identity on the bond that needs to be truncated

$$R^{-1}R\tilde{R}\tilde{R}^{-1} \approx \tilde{R}V'\frac{1}{s'}U'^{\dagger}R = \tilde{P}P, \tag{2.30}$$

with $\tilde{P} = \tilde{R}V'\frac{1}{\sqrt{s'}}$ and $P = \frac{1}{\sqrt{s'}}U'^{\dagger}R$, see Fig. 2.18(c). For a fast-decaying singular value spectrum s or for high χ, some of the singular values may reach values around machine precision which are problematic in the inversion. Instabilities can be avoided by setting singular values below a certain cutoff to zero.

A numerically cheaper variant of the projector scheme is obtained by basing the projector computation only on the lower-left and upper-left corners of the network in Fig. 2.18(a), which is the version that has been used in this work. In addition, a significant reduction in the computational cost can be achieved by using an iterative SVD. This allows us to only compute the χ leading singular values instead of the full spectrum. This reduces the leading computational cost from $\mathcal{O}(\chi^3 D^6)$ to $\mathcal{O}(\chi^3 D^4)$.

2.4.2. Coarse-graining contraction

An alternative family of iPEPS contraction approaches is formed by coarse-graining methods [99–104]. The main idea of these methods is to contract a group of tensors in the network to a single tensor and to replace this tensor with an accurate lower bond dimension approximation. The truncation can be performed using a local scheme which is computationally cheap [99, 101], or it can be optimized by taking the effects of the environment into account [100,101] and by removing short-range correlations more accurately [102–104].

To illustrate this class of algorithms we discuss one instance, the higher-order tensor renormalization group (HOTRG) [101], in more detail. The HOTRG is a coarse-graining algorithm based on a local truncation scheme. At each step of a HOTRG contraction, a coarse-graining of two tensors is performed over one axis of the network, as is shown in Fig. 2.19 for a square lattice. The new tensor has an enlarged bond in the orthogonal direction, which is truncated to χ to avoid exponential growth of the bond dimension. The bond dimension χ controls the accuracy of the contraction. This truncation is performed by inserting projectors onto the enlarged bond, in the way shown in Fig. 2.20(a). The same procedure is followed for each axis of the network which together complete one iteration. These iterations are repeated until sufficient convergence is achieved. The computational cost of HOTRG scales as $\mathcal{O}(\chi^7)$ for square lattices. It is straightforward to generalize the method to cubic networks, for which the dominant scaling becomes $\mathcal{O}(\chi^{11})$.

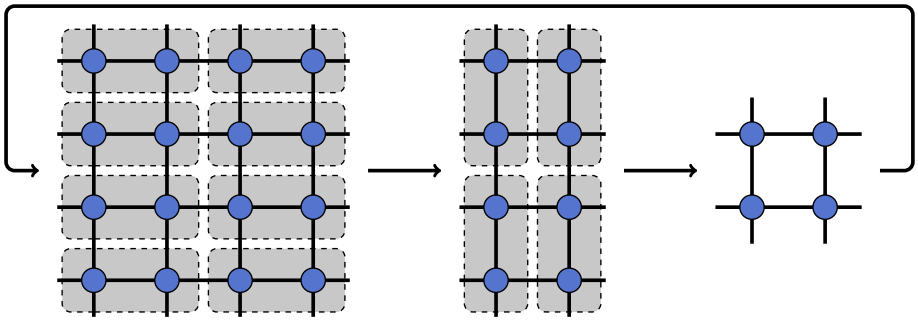

Figure 2.19: The HOTRG contraction for a square lattice network. A coarse-graining contraction is first done in the horizontal direction and after that in the vertical direction. These steps are iterated until convergence. Each full iteration reduces the total number of tensors in the network by a factor of four.

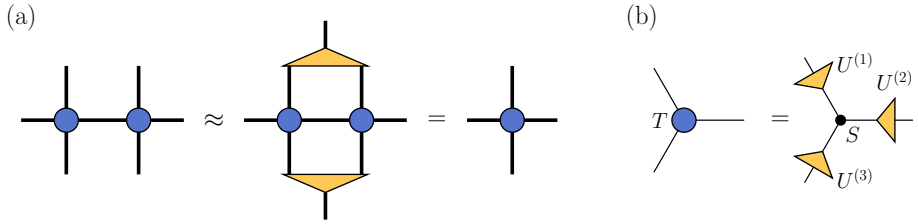

Figure 2.20: (a) One step of the HOTRG method in the horizontal direction. The projectors are obtained from a HOSVD decomposition. (b) A HOSVD decomposition of a rank-3 tensor T.

The projectors are obtained using a higher-order singular value decomposition (HOSVD), which is a generalization of the (matrix) SVD to higher-rank tensors [105]. To illustrate the HOSVD, let us consider a rank-3 tensor T. The HOSVD of this tensor is given by

$$T_{a_1 a_2 a_3} = \sum_{ijk} S_{ijk} U^{(1)}_{ia_1} U^{(2)}_{ja_2} U^{(3)}_{ka_3}, \tag{2.31}$$

with $U^{(i)}$ unitary matrices and S the so-called core tensor, as can be seen in Fig. 2.20(b). The core tensor obeys all-orthogonality, which means that

$$\sum_{jk} S_{\alpha jk} S_{\beta jk} = \sum_{ik} S_{i\alpha k} S_{i\beta k} = \sum_{ij} S_{ij\alpha} S_{ij\beta} = 0, \tag{2.32}$$

for $\alpha \neq \beta$. Furthermore, the following ordering condition is enforced

$$\sqrt{\sum_{jk} S^2_{\alpha jk}} \geq \sqrt{\sum_{jk} S^2_{\beta jk}}, \tag{2.33}$$

for $\alpha < \beta$. Similar to the SVD, a lower-rank approximation of T can be made by truncating the core tensor. Unlike the SVD case, however, this truncation is not guaranteed to be the optimal lower-rank truncation [106].

An improvement in accuracy over the HOTRG can be obtained in the closely related higher-order second renormalization group (HOSRG) [101]. In this method, we start from a HOTRG contraction, which we then attempt to improve by optimizing the projectors. This is achieved through back- and forwarded iterations which take the global tensor network environment around a truncated bond into account.

For larger supercells or for tensors that are not rotationally symmetric, the direct use of the HOSVD in the HOTRG contraction will not provide accurate projectors. In that case, we can use a different scheme that was proposed in Ref. [107]. Let us consider a HOTRG contraction in the x-direction, as shown in Fig. 2.21(a). To compute the projectors that truncate the bond, we can use an approach inspired by the projector computation in the directional CTM discussed in Sec. 2.4.1. First, we perform two QR decompositions in the way shown in Fig. 2.21(b). We then use R and $\tilde{R}$ to compute the projectors following the steps shown in Figs. 2.18(b) and 2.18(c). Note that the computational cost of the QR decomposition to obtain R can be reduced by contracting the tensors with their Hermitian conjugate and performing an eigendecomposition, as is shown in Fig. 2.21(c). A similar procedure can be followed for $\tilde{R}$.

2.4.3. MPS-MPO contraction

The final class of contraction algorithms that we want to discuss here are the MPS-MPO methods [29, 30, 54, 108], which are inspired by algorithms used in 1D.

Let us first consider a finite PEPS contraction, as is shown in Fig. 2.22. The first and last rows of the PEPS can be seen as MPSs $|\phi_1\rangle$ and $|\phi_N\rangle$, respectively,

$$|\phi_1\rangle = \sum_{d_1 \ldots d_N = 1}^{D^2} \mathrm{Tr}\Big(T^{[1,1]}_{d_1} \ldots T^{[1,N]}_{d_N}\Big) \, |d_1 \ldots d_N\rangle \,, \tag{2.34}$$

$$|\phi_N\rangle = \sum_{u_1 \ldots u_N = 1}^{D^2} \mathrm{Tr}\Big(T^{[N,1]}_{u_1} \ldots T^{[N,N]}_{u_N}\Big) \, |u_1 \ldots u_N\rangle \,, \tag{2.35}$$

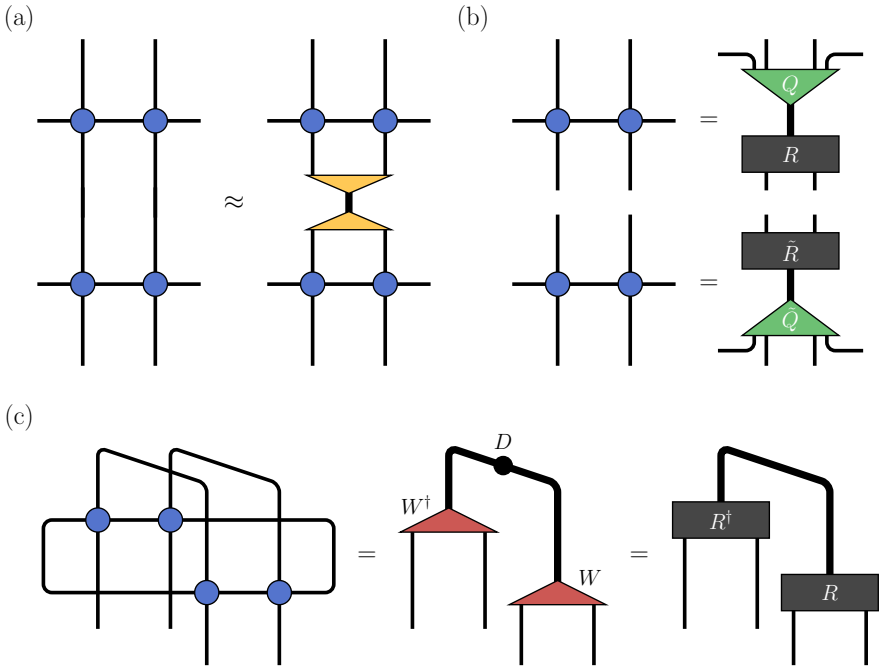

Figure 2.21: A generalization of the HOTRG contraction for larger supercells or in the absence of rotationally symmetric tensors, following Ref. [107]. (a) The projectors on one bond for a coarse-graining step in the x-direction. (b) To obtain the projectors, we first perform QR decompositions on the tensors on the top and the bottom. The projectors are computed using the R and $\tilde{R}$ tensors, based on the approach used in the directional CTM contraction shown in Figs. 2.18(b) and 2.18(c). (c) A more efficient way to obtain R. The tensors are contracted with their Hermitian conjugate, with the bottom legs left open. An eigendecomposition $WDW^\dagger$ is performed on this object, which is used to compute $R = W\sqrt{D}$.

with $T^{[i,j]}$ a tensor at lattice site (i, j) and d_i and u_i the vertical bonds of the first and last row of the PEPS, respectively. The other layers of the PEPS are seen as matrix product operators (MPO)

$$M_i = \sum_{\substack{u_1 \dots u_N = 1 \\ d_1 \dots d_N = 1}}^{D^2} \mathrm{Tr}\left(T^{[i,1]}_{u_1 d_1} \dots T^{[i,N]}_{u_N d_N} \right) |d_1 \dots d_N\rangle \langle u_1 \dots u_N| \,, \tag{2.36}$$

where M_i is the MPO at row i.

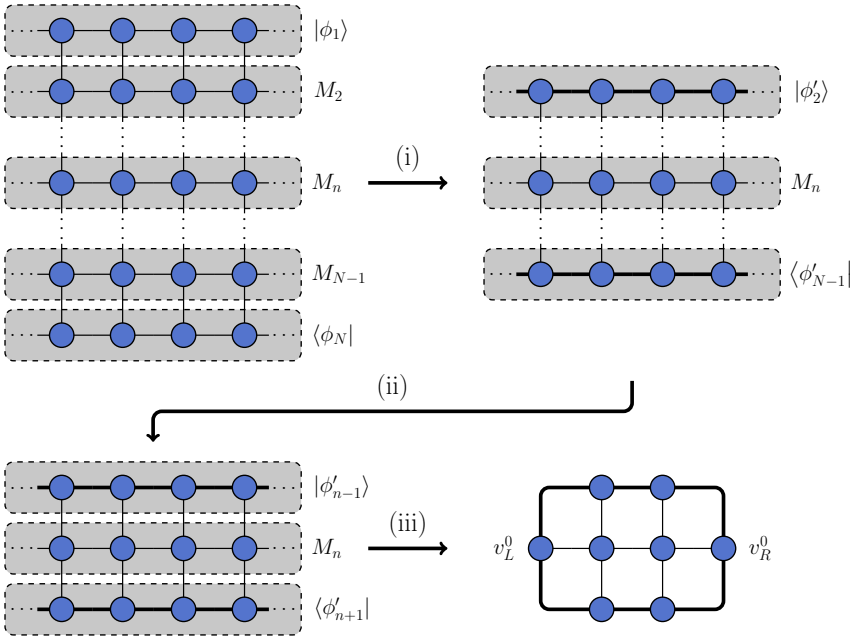

Figure 2.22: A diagrammatic overview of the MPS-MPO contraction method, as discussed in the main text. We start from the initial PEPS and identify the first and final rows as MPS $|\phi_1\rangle$ and $|\phi_N\rangle$, respectively. The other rows are seen as MPO layers M_n. In step (i), the rows M_2 and M_{N-1} are contracted with $|\phi_1\rangle$ and $|\phi_N\rangle$, respectively, and a truncation is done. These steps are iterated until we reach the desired row n, as shown in step (ii). Finally, in step (iii), the leading eigenvectors from the left v_L^0 and right v_R^0 are determined which results in a diagram that can be contracted directly.

The contraction now proceeds by iteratively applying the MPO to the boundary MPS. For the MPS at the top, the i-th MPO can be applied to the boundary MPS as

$$M_i \left|\phi'_{i-1}\right\rangle = \left|\tilde{\phi}_i\right\rangle \approx \left|\phi'_i\right\rangle, \tag{2.37}$$

with $\left|\tilde{\phi}_i\right\rangle$ and $|\phi'_i\rangle$ the new boundary MPS before and after truncation, respectively. A similar procedure can be followed for the MPS on the bottom. The accuracy of the contraction is controlled by the bond dimension of the boundary MPS χ. The truncation from $D^2\chi$ to χ can be done by various schemes, e.g., based on DMRG [29, 30] or TEBD [54]. Once all the rows are contracted into the boundary MPS we obtain a 1D object, which can be contracted exactly. This is done by computing the left- and right-leading eigenvectors v_L^0 and v_R^0,

respectively. This finally gives a diagram that can be contracted directly.

For an iPEPS, the contraction proceeds similarly, with the difference that we are interested in computing the leading eigenvector $|\phi\rangle$. When we assume that the iPEPS consists of identical MPO-rows M we have

$$M\,|\phi\rangle = \eta\,|\phi\rangle\,, \tag{2.38}$$

with η the leading eigenvalue. The leading eigenvector can, for example, be computed by a power method [54] or by a fixed-point method as is done in the VUMPS algorithm [108]. If the iPEPS is made up of a supercell that extends k rows, the leading eigenvector of the combined MPO $M_1 M_2 \dots M_k$ should be computed.

2.5. Ground state algorithms

In the previous sections, we defined the iPEPS ansatz and discussed how its expectation values can be evaluated. We did not yet address how an iPEPS wave function can be obtained that accurately represents the ground state though. For some models, the ground state can be written down exactly as an iPEPS. Well-known examples include the ground state of the AKLT Hamiltonian [109, 110] and of the toric code [91, 111], which can both be written down as an iPEPS with $D = 2$. These cases, however, form the exception. For the vast majority of models, it is necessary to make use of an optimization algorithm. The most commonly applied algorithms can be divided into two classes. The first class consists of algorithms that make use of an imaginary time evolution. The second class is made up of methods that directly minimize the energy of the ansatz based on the variational principle. Both classes are discussed in more detail in the following sections.

2.5.1. Imaginary time evolution

The idea of an imaginary time evolution is that an initial state $|\phi\rangle$ (e.g., an iMPS or iPEPS ansatz with random entries) is projected down to the ground state $|\psi_0\rangle$ of a given Hamiltonian H by applying the imaginary time evolution operator

$$\lim_{\beta\to\infty} e^{-\beta H}\,|\phi\rangle = |\psi_0\rangle\,, \tag{2.39}$$

with β the inverse temperature. To apply the imaginary time evolution operator to the tensor network ansatz we first decompose it into a series of local operators

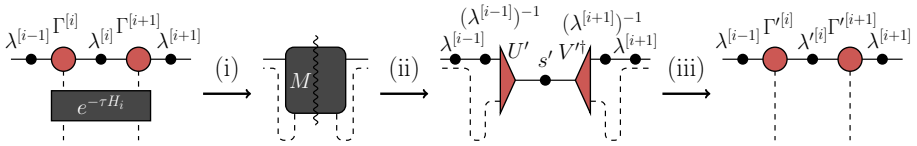

Figure 2.23: An update step of the iTEBD algorithm at bond i, as discussed in the main text. In step (i), the time evolution gate $e^{-\tau H_i}$ is applied to the tensors around bond i. This creates a tensor M, which is reshaped into a matrix. An SVD of M is performed in step (ii), where we only keep the D largest singular values. In step (iii), the unitary matrices are reshaped into rank-3 tensors, and the singular value matrices on the neighboring bonds are reintroduced by inserting identities onto those bonds and absorbing the inverse singular value matrices into the tensors.

using a Trotter-Suzuki decomposition. When we assume that the Hamiltonian can be written as a sum of local terms $H = \sum_i H_i$, the first-order Trotter-Suzuki decomposition can be written as follows

$$e^{-\beta H} = \left(e^{-\tau \sum_i H_i}\right)^M = \prod_{j=1}^{M} \prod_i e^{-\tau H_i} + \mathcal{O}(\tau), \tag{2.40}$$

with $\beta = \tau M$. The error can be further reduced to $\mathcal{O}(\tau^2)$ by reversing the order in which the Trotter gates $e^{-\tau H_i}$ are applied to the ansatz at every other time step. This is known as a second-order Trotter-Suzuki decomposition, and it will be used in the rest of this work. The application of the Trotter gate increases the size of the bond dimension, which needs to be truncated to avoid exponential growth. There are various schemes to do this truncation which is the main topic for the rest of this section.

Imaginary time evolution for iMPS

To introduce some basic ideas, we first discuss the 1D case. A popular method to do imaginary time evolution for iMPS is the infinite time-evolving block decimation (iTEBD) method [79, 80, 112]. We make use of an iMPS and adopt the convention where we keep singular value matrices $\lambda^{[i]}$ on the bonds. We, furthermore, assume that the iMPS is in canonical form. One step of the algorithm is shown in Fig. 2.23 for an update on bond i, where we assume nearest-neighbor interactions. The step proceeds as follows:

(i) Apply the imaginary time evolution gate $e^{-\tau H_i}$ to bond i and contract the resulting diagram as shown on the left-hand side of Fig. 2.23. We also

absorb the singular value matrices on the neighboring bonds, which are required by the canonical form. The resulting tensor is reshaped into a matrix M.

(ii) An SVD is performed on this matrix

$$M = UsV^\dagger \approx U's'V'^\dagger, \tag{2.41}$$

where a truncation is performed on the unitary matrices $U \to U'$ and $V \to V'$, and on the singular value matrix $s \to s'$ keeping only the D largest singular values. We obtain the updated $\lambda'^{[i]} = s'$.

(iii) Reshape U' and $V'^\dagger$ back to rank-3 tensors. On the open virtual bonds on the left and right, we reintroduce the singular value matrices of the neighboring bonds by inserting the identities $\lambda^{[i-1]}\left(\lambda^{[i-1]}\right)^{-1} = \mathbb{I}$ and $\left(\lambda^{[i+1]}\right)^{-1}\lambda^{[i+1]} = \mathbb{I}$, respectively. The matrices $\left(\lambda^{[i-1]}\right)^{-1}$ and $\left(\lambda^{[i+1]}\right)^{-1}$ are contracted into the rank-3 tensors giving the updated tensors $\Gamma'^{[i]}$ and $\Gamma'^{[i+1]}$, respectively.

Similar steps are repeated for all the bonds in the ansatz to complete one time step. These time steps, in their turn, are iterated until sufficient convergence is reached. To decrease the Trotter error, the Trotter step τ can be gradually reduced during the evolution.

Note that the imaginary time operator is non-unitary, and it does not keep the iMPS in canonical form. To keep the truncation accurate this, in principle, makes it necessary to transform the iMPS back to a canonical form after each update step. Conveniently, it turns out that when τ is small enough, the gates are close to identities, and the iMPS remains in a form that is close to canonical, making this transformation unnecessary [83].

Imaginary time evolution for iPEPS

Imaginary time evolution for iPEPS is significantly more involved than for iMPS. This is mainly due to the absence of a canonical form for iPEPS, which makes performing accurate truncations of the ansatz more difficult and computationally expensive. A common way to do imaginary time evolution for iPEPS is with the full update (FU) algorithm. After applying a Trotter gate to a bond, an optimal truncation requires minimizing the norm distance

$$\begin{aligned} d &= \left\| |\tilde{\psi}\rangle - |\psi'\rangle \right\|^2 \\ &= \langle\tilde{\psi}|\tilde{\psi}\rangle + \langle\psi'|\psi'\rangle - \langle\tilde{\psi}|\psi'\rangle - \langle\psi'|\tilde{\psi}\rangle, \end{aligned} \tag{2.42}$$

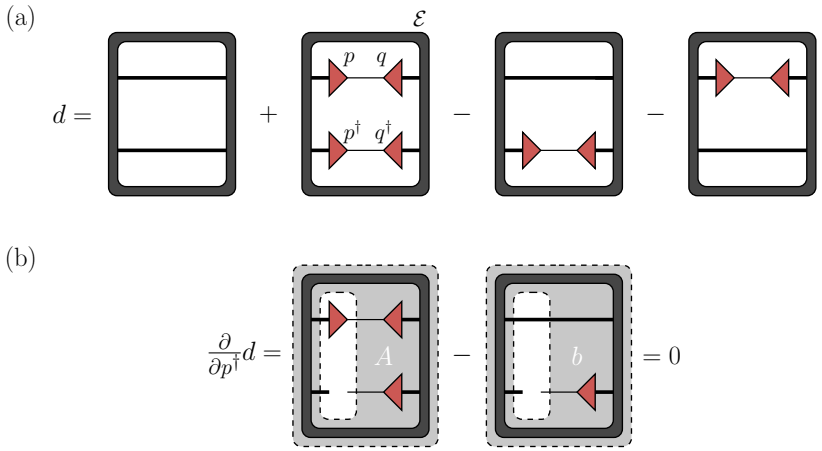

Figure 2.24: (a) A diagrammatic representation of the norm distance in Eq. 2.42. The gray boundary represents the CTM environment $\mathcal{E}$, while the bonds on the top and the bottom correspond to the updated bond on the bra- and ket-sides, respectively. The updated bond is renormalized by inserting projectors p and q. (b) The projector p is optimized by taking the derivative of Eq. 2.42 and solving the resulting linear equation. By iteratively optimizing p and q in this manner, the norm distance can be minimized.

with $|\tilde{\psi}\rangle$ the iPEPS with the Trotter gate applied to it and $|\psi'\rangle$ the truncated iPEPS, see Fig. 2.24(a). To compute these overlaps, we need to perform a full contraction of the iPEPS ansatz. Here, we will make use of the CTM which gives us the environment $\mathcal{E}$ in Fig. 2.25. To truncate the updated bond, we insert the projectors p and q and we optimize them iteratively such that they minimize the distance in Eq. 2.42. We start by doing an optimization step for p. When we fix q, an optimal p can be obtained by taking a derivative with respect to $p^\dagger$ in Eq. 2.42 and by solving the resulting linear equation

$$\frac{\partial}{\partial p^\dagger} d = Ap - b = 0, \tag{2.43}$$

where A and b are indicated in Fig. 2.24(b). We continue by fixing p and solving for q. This procedure can be iterated until Eq. 2.42 is minimized sufficiently. The tensors in the iPEPS ansatz are then updated and the next gate is applied.[4]

[4]Note that the projectors are not optimal globally. The reason is that they are obtained for an iPEPS where only one bond is updated, while these projectors are subsequently used to update all equivalent bonds in the iPEPS ansatz. In the FU method, this effect is assumed to be negligible.

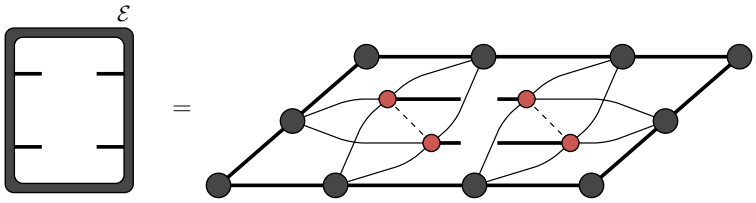

Figure 2.25: The environment $\mathcal{E}$ around a horizontal iPEPS bond computed using the CTM. The updated bonds are left open.

Due to the approximations in the iPEPS contraction as well as numerical error, the CTM environment $\mathcal{E}$ will not be exactly Hermitian or positive semidefinite. Numerical instabilities in the algorithm can be avoided by making the environment Hermitian explicitly $\tilde{\mathcal{E}} = \left(\mathcal{E} + \mathcal{E}^\dagger\right)/2$, and by making $\tilde{\mathcal{E}}$ positive semidefinite by taking an eigendecomposition of $\tilde{\mathcal{E}} = WDW^\dagger$ and setting negative eigenvalues to zero

$$D_+ = \begin{cases} D_i & D_i \geq 0 \\ 0 & D_i < 0 \end{cases}, \tag{2.44}$$

with D_i the i-th eigenvalue [113]. This results in the environment $\tilde{\mathcal{E}}_+ = WD_+W^\dagger$.

The computational cost of the FU procedure is dominated by the environment contraction which has to be redone every time a new gate is applied. A method to reduce this cost is the fast-full update (FFU) [114]. Since the change in the environment is small after each update step, it is sufficient in most cases to only perform one CTM step in the direction of the updated bond to approximate the environment. Although this does not affect the dominant computational scaling, the number of CTM update steps reduces significantly. To ensure that the environment remains accurate, a recomputation of the environment can be done after a certain number of update steps.

Although the FFU can significantly reduce the computational cost of an imaginary time evolution with iPEPS, the cost to compute the environment can still be prohibitively large in some cases. Therefore, less accurate, but computationally significantly cheaper methods have been developed as well. These methods make use of an approximate representation of the environment around the bond that is updated. To finish the discussion on imaginary time evolution methods, we will talk about two such approaches: the simple update (SU) and the cluster update (CU) algorithms.

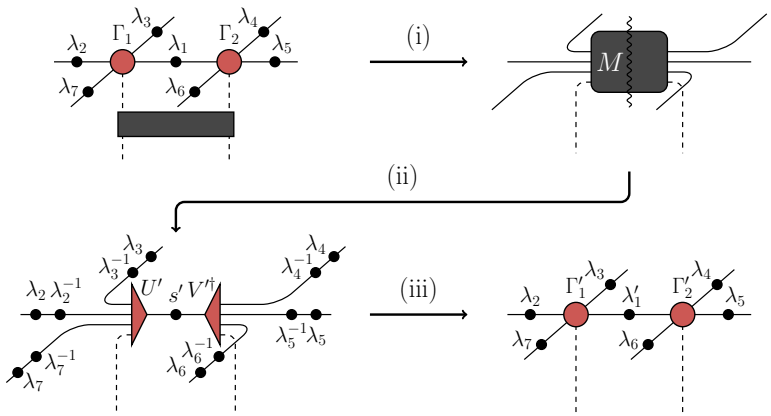

Figure 2.26: An update step in the SU algorithm, as discussed in the main text. In step (i), the gate is applied to the tensors and the resulting diagram is contracted. We also contract the singular value matrices on the neighboring bonds, which gives the tensor M. An SVD is then done in step (ii), where we perform a truncation and only keep the D largest magnitude singular values. In step (iii), the resulting unitaries U' and $V'^{\dagger}$ are reshaped back into tensors, and the singular value matrices on the neighboring bonds are reinserted by absorbing their inverses into the tensors.

Simple update

The simple update (SU) algorithm [115] can be understood as a direct application of the iTEBD algorithm to iPEPS. Similar to iTEBD, it is convenient to use the convention where the singular value matrices λ are kept on each bond. One step of the algorithm is shown in Fig. 2.26, and it proceeds as follows:

(i) Apply an imaginary time evolution gate to the iPEPS tensors and contract the resulting diagram. We also contract the singular value matrices of the neighboring bonds. This gives the tensor M.

(ii) Reshape the tensor M to a matrix and perform an SVD. We truncate the SVD tensors and only keep the largest D singular values.

(iii) Reshape the two unitary matrices U' and $V'^{\dagger}$ to tensors. We also insert identities of the form $\lambda_i \lambda_i^{-1}$ on the neighboring bonds and contract λ_i^{-1} with the tensors. This gives us the updated tensors.

A further reduction in the numerical cost of the SU can be achieved by splitting off the physical leg from the iPEPS tensors before applying the Trotter gate using a QR decomposition [116]. The algorithm can also be formulated in a

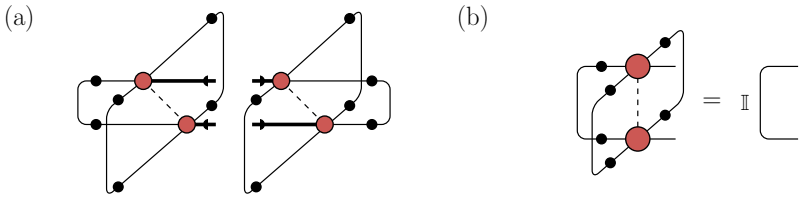

Figure 2.27: (a) The environment approximation that is used in the SU. (b) The left quasi-canonical form condition. For an iPEPS to be in the quasi-canonical form, this condition should be satisfied by all tensors and in all directions.

similar way to FU by minimizing Eq. 2.42 with the environment approximation shown in Fig. 2.27(a).

The SU method uses an environment approximation which is similar to the environment that would be used for an iMPS truncation. While an iTEBD evolution for iMPS with small τ brings the iMPS close to a canonical form, a SU evolution transforms an iPEPS to a quasi-canonical form [82, 117] (also known as a superorthogonal form [118]). In this form, the iPEPS satisfies the condition shown in Fig. 2.27(b) for all tensors and in all directions.

Despite the rough environment approximation, the SU is typically able to identify the correct phases and provides reasonably accurate results for models with short correlation lengths. For longer correlation lengths, more accurate optimization methods are often required.

Cluster update

The cluster update (CU) [119–121] can be considered to lie in between the SU and the FU both in terms of computational cost as well as its accuracy. In the CU, the truncation of the bond dimension is based on a local environment consisting of a finite cluster, for example, the 4×3 cluster, which is shown in Fig. 2.28. With this environment, a minimization of the distance in Eq. 2.42 can be made. In general, a trade-off exists between the size of the cluster (and thus the computational cost) and the accuracy of the optimization. The optimal cluster choice thus depends on the model under consideration.

Practical considerations

Before continuing, we would like to discuss some practical considerations in ground-state simulations. As in any optimization approach, imaginary time

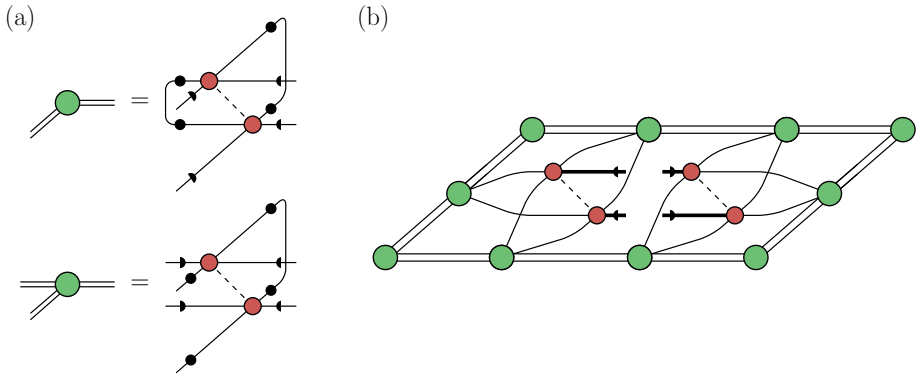

Figure 2.28: A 4×3 environment that can be used in the CU. (a) A more compact notation to represent the tensors at the corners and edges of this cluster. The full black circles represent singular value matrices λ, while the black half-circles represent their square root $\sqrt{\lambda}$. (b) The 4×3 cluster environment in the horizontal direction.

evolution methods can get trapped in local minima, e.g., in meta-stable phases. One reason for this is that the size of the variational subspace available in a truncation $dD \to D$ is constrained by the value of D. This subspace can sometimes be too small, which can cause a simulation to get stuck. Another factor is the size of the supercell, which must be large enough to support the ground state.

A good choice for the initial state can significantly reduce the chance of getting stuck in a local minimum and it can also decrease the simulation time considerably. A common strategy for CU or (F)FU simulations is to first perform SU optimizations from several random initial states. The state with the lowest energy can subsequently be selected as an initial state for a more accurate optimization. Another strategy is to use an up- or down-ramping, where an already optimized lower or higher bond dimension state, respectively, is used as the initial state.

How prone a simulation is to these problems varies depending on the model under consideration and it is often best to combine these strategies.

2.5.2. Energy minimization

An alternative strategy to find an (i)MPS or (i)PEPS approximating the ground state is the energy minimization. The idea is to optimize the entries in the

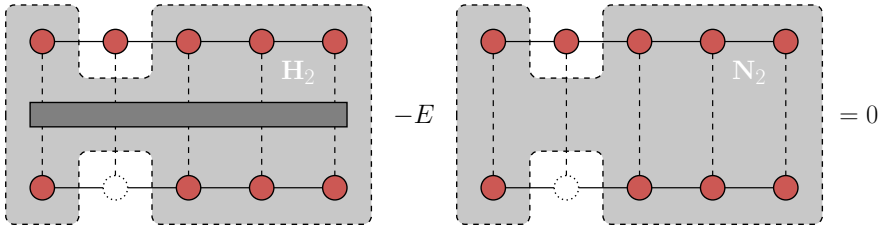

Figure 2.29: Example of the generalized eigenvalue problem from Eq. 2.47 obtained in a single-site energy minimization scheme at the second site of the MPS. The shaded regions on the left and right correspond to $\mathbf{H}_2$ and $\mathbf{N}_2$, respectively.

tensor network ansatz in such a way as to directly minimize the energy in correspondence with the variational principle. For a certain bond dimension D

$$|\psi_{0,D}\rangle = \arg\min_{|\phi_D\rangle} \frac{\langle\phi_D|H|\phi_D\rangle}{\langle\phi_D|\phi_D\rangle}, \tag{2.45}$$

where $|\phi_D\rangle$ is the tensor network ansatz with bond dimension D that is being optimized and $|\psi_{0,D}\rangle$ is the optimal wave function for fixed D.

As an example, let us consider a finite MPS consisting of five sites. A tensor T_i of this MPS can be optimized by solving

$$\frac{\partial}{\partial T_i^\dagger}\left(\frac{\langle\phi_D|H|\phi_D\rangle}{\langle\phi_D|\phi_D\rangle}\right) = 0, \tag{2.46}$$

which can be rewritten as

$$\mathbf{H}_i T_i - E\mathbf{N}_i T_i = 0, \tag{2.47}$$

with $\mathbf{H}_i$ and $\mathbf{N}_i$ defined as in Fig. 2.29. This process can be iterated over all the tensors until convergence is reached. This method corresponds to a reformulation of the single-site DMRG method in the MPS language [21, 22].

Energy minimization schemes were adopted early on for finite PEPS as well [29, 30]. For iPEPS ansätze, however, energy minimizations can be difficult to implement and early works, therefore, preferred the use of imaginary time evolution methods to find approximate ground state representations. One important difficulty is that the optimization is highly non-linear because each tensor in the iPEPS ansatz appears infinitely many times. Another difficulty is that the computation of $\mathbf{H}$ in Eq. 2.47 involves a summation over an infinite number of Hamiltonian terms which is challenging to compute. These problems were largely addressed in Refs. [122, 123], showing that energy minimization can produce results outperforming FU simulations. A more recent innovation has come

from the incorporation of the automatic differentiation technique from machine learning into energy minimization schemes, which greatly simplifies the implementation of the gradient computation [124].

2.6. Symmetries

Symmetries lie at the basis of many modern physical theories and can often be used to massively simplify problems. In numerical physics, symmetries can be used to reduce the degrees of freedom that need to be considered, and thus they can increase the efficiency of simulations. In exact diagonalization this, for example, allows you to reach larger system sizes, and also in tensor network algorithms symmetries can be used to simulate larger bond dimensions.

On a lattice, symmetries can be divided into two categories. The first one consists of spatial symmetries, such as translation, rotation, or mirror symmetries. We have, for example, already demonstrated how translation symmetry is exploited in the iMPS and iPEPS ansätze. The second category comprises internal symmetries, such as $SU(2)$ spin rotational invariance. Here, we are concerned with incorporating the latter. In our discussion, we will be following Refs. [125, 126].

For concreteness, we consider a $U(1)$ symmetry acting on a Hilbert space $\mathcal{H}$. The $U(1)$ symmetry group is often used for spin models or in the case of particle conservation.[5] We can define a linear representation of the $U(1)$ group $U(\phi) : \mathcal{H} \to \mathcal{H}$, where $U(\phi)$ satisfies

$$U(\phi_1) + U(\phi_2) = U(\phi_1 + \phi_2), \tag{2.48}$$

for $\phi_1, \phi_2 \in [0, 2\pi)$. This representation is unitary if it satisfies

$$U^\dagger(\phi)U(\phi) = U(\phi)U^\dagger(\phi) = \mathbb{I}, \tag{2.49}$$

for $\phi \in [0, 2\pi)$.

In the presence of the symmetry, the Hilbert space can be decomposed as a direct sum over irreducible representations of the group

$$\mathcal{H} = \bigoplus_k \mathcal{H}_k, \tag{2.50}$$

with $\mathcal{H}_k$ a (possibly degenerate) subspace of $\mathcal{H}$. Each $\mathcal{H}_k$ can be associated to a charge c_k.

[5] Because of practical considerations, in our simulations we will make use of a $\mathbb{Z}_q$ symmetry (which is a subgroup of $U(1)$) with a high q.

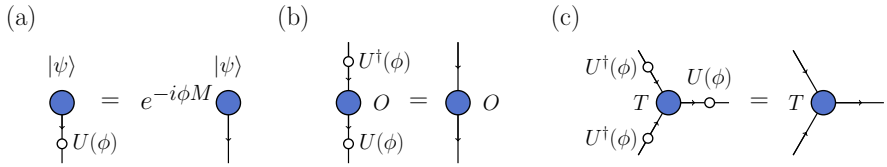

Figure 2.30: Symmetry conditions for various objects. (a) State $|\psi\rangle$. (b) Matrix O. (c) Rank-3 tensor T.

As an example, let us consider a spin model with a $U(1)$ symmetry of the z-component of the spin. The generator of the symmetry is the total magnetization

$$M = \sum_i S_i^z, \tag{2.51}$$

which has eigenstates $|ma_k\rangle$ with eigenvalue $M|ma_k\rangle = m|ma_k\rangle$. In this case, m is the charge (which can be interpreted as the magnetization) and a label a_k accounts for a potential degeneracy of $\mathcal{H}_k$. We can write $U(\phi)$ as

$$U(\phi) = \exp(-i\phi M). \tag{2.52}$$

Let us now consider a state $|\psi\rangle \in \mathcal{H}$. It is considered symmetric if it transforms as

$$U(\phi)|\psi\rangle = e^{-i\phi m}|\psi\rangle, \tag{2.53}$$

which is displayed diagrammatically in Fig. 2.30(a). This implies that $|\psi\rangle$ can be written in the basis of the corresponding subspace $\mathcal{H}_k$.

A matrix O, e.g., the Hamiltonian H, is symmetric if it transforms as

$$U^\dagger(\phi) O U(\phi) = O, \tag{2.54}$$

which is also shown in Fig. 2.30(b). Note that it follows from Schur's lemma that

$$O = \bigoplus_k O_k, \tag{2.55}$$

which implies that O conserves charge, i.e., a symmetric state $|\psi\rangle$ applied to O will remain in the same symmetry sector.

2.6.1. Symmetric tensor networks

Let us now look at a rank-n tensor T, with each index of the tensor acting on a certain Hilbert space $\mathcal{H}$. For this tensor, we also want to define a symmetry

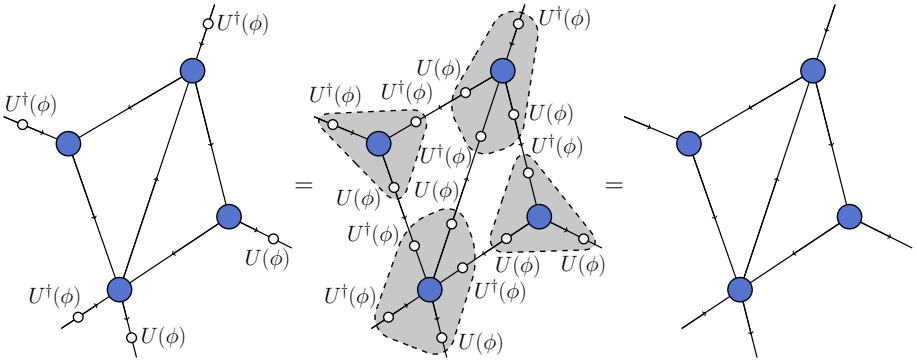

Figure 2.31: An example of a tensor network satisfying the symmetry condition. On each of the connected bonds, identities can be introduced $U(\phi)U^\dagger(\phi) = \mathbb{I}$. By using the symmetry condition from Eq. 2.57 for each individual tensor, we obtain the diagram on the right.

condition. This can be done by grouping the indices of the tensor into two arbitrary groups I_1 and I_2, i.e.,

$$\mathcal{H}_1 = \bigotimes_{i\in I_1} \mathcal{H}_i, \qquad \mathcal{H}_2 = \bigotimes_{i\in I_2} \mathcal{H}_i. \tag{2.56}$$

This allows us to write the tensor T as a matrix similar to Eq. 2.54. We will refer to I_1 and I_2 as incoming and outgoing indices, respectively. We can thus write the symmetry condition as

$$\left(U^{(1)}(\phi)\right)^\dagger T \left(U^{(2)}(\phi)\right) = T, \tag{2.57}$$

with $U^{(1)}(\phi) = \bigotimes_{i\in I_1} U^{(i)}(\phi)$ and $U^{(2)}(\phi) = \bigotimes_{i\in I_2} U^{(i)}(\phi)$, also see Fig. 2.30(c). Note that this implies that the tensor in this form also obeys Eq. 2.55 and that the incoming and outgoing indices preserve charge in a similar way. Tensor elements that do not conserve charge violate the symmetry condition and thus vanish. By writing T as a symmetric tensor, we thus require fewer parameters, which means that we found a much more efficient representation of the tensor.

A tensor network that is composed of symmetric tensors, in its turn, is also symmetric, as is shown for an example in Fig. 2.31.

2.6.2. Algorithms with symmetric tensors

We now consider some common operations used in tensor network algorithms and how they can be done with symmetric tensors. Two of the most important,

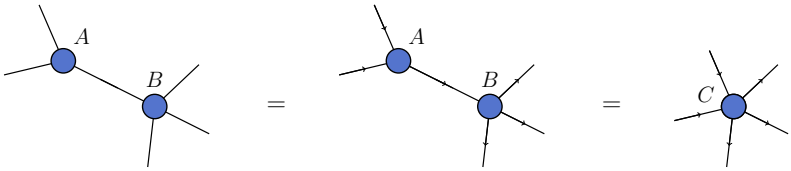

Figure 2.32: A contraction of two symmetric tensors A and B. First, the indices are labeled as incoming or outgoing depending on the index that is being contracted over. After that, the contraction proceeds by multiplying the different symmetry blocks and combining the results to construct tensor C.

and computationally demanding, operations are contractions and factorizations such as the SVD or eigendecompositions. We will first focus on the former.

Consider two tensors A and B that we want to contract over a certain index, see Fig. 2.32. First, we reshape the tensors to matrices in a similar way as done in Eq. 2.56, where the incoming and outgoing indices are chosen based on the index that is contracted. This brings the tensors to a block-diagonal form

$$A = \bigoplus_k A_k, \qquad B = \bigoplus_k B_k. \tag{2.58}$$

The contraction $C = A \cdot B$ now proceeds by multiplying the respective symmetry blocks, i.e., $C_k = A_k \cdot B_k$. After this is done for all sectors, we obtain $C = \bigoplus_k C_k$, and the indices of C are reshaped back.

For a factorization, such as the SVD, we can also make use of this block structure. For example, an SVD of A can be done by performing an SVD for each $A_k = U_k s_k V_k^\dagger$. We obtain the resulting matrices as $U = \bigoplus_k U_k$, $s = \bigoplus_k s_k$, and $V^\dagger = \bigoplus_k V_k^\dagger$.

A significant numerical cost saving is achieved through this block structure. When we assume A has q symmetry sectors with a degeneracy d, the cost of, for example, the SVD would be $q^3 d^3$ if we use non-symmetric tensors, while the symmetry construction reduces this to qd^3. Note that in practice, algorithms making use of symmetric tensors can suffer from numerical overheads for small bond dimensions which are associated with maintaining the symmetric form.

One complication arising for algorithms using symmetric tensors is determining the optimal charge sectors to keep on each index for the problem at hand. While the charge sectors for the physical index are determined by the local basis of the Hamiltonian, this is not the case for the virtual indices. The number of charge sectors kept on the virtual indices is restricted by the iPEPS bond dimension D. In practice, the most relevant charge sectors are determined dynamically during the algorithms.

2.7. Extrapolations

One of the main limitations of iPEPS simulations is that the bond dimensions that can be accurately reached are often limited and too small to reach sufficient convergence. Through the use of symmetries, the attainable bond dimensions can be increased, but they can still be too small to reach sufficient convergence and symmetries cannot be used in all cases. Therefore, extrapolations are commonly used to find estimates of observables.

A commonly used method in iPEPS simulations is the $1/D$ extrapolation. The idea of this approach is that the exact state can be approached for at most $D \to \infty$ or $1/D \to 0$. Observables like the energy typically converge faster than linear in $1/D$, however, which means that the extrapolation provides a lower bound. One way to obtain an estimate, therefore, is to take the mean between the extrapolated result and the value at the largest simulated D (which provides an upper bound). As an error on this estimate one can use the difference with the extrapolated or largest D result. The main appeal of the $1/D$ extrapolation is its simplicity. Its accuracy can be limited though, especially for closely competing phases.

Another approach is finite correlation length scaling which can be used in the presence of a diverging correlation length. These methods were originally developed for iMPS ansätze [127–130] but were later successfully extended to iPEPS [131, 132]. The main idea is that the finite D acts to constrain the correlation length that can be described by the iPEPS to a maximum value ξ_D, which can be tuned by varying D. An extrapolation in $1/\xi_D$ can then be performed in a similar fashion to finite-size scaling in, e.g., exact diagonalization or quantum Monte Carlo (QMC).

Other approaches have also been developed, such as extrapolations in the error of the truncation to D obtained in the optimization. When the ansatz represents the ground state exactly this error becomes zero. This type of extrapolation is commonly used in MPS studies and it can also provide more accurate results for iPEPS simulations [133].

CHAPTER 3

Contraction approaches for 3D iPEPS

Tensor network algorithms have proven to be very powerful tools for studying 1D and 2D quantum many-body systems. However, their application to 3D quantum systems has so far been limited, mostly because the efficient contraction of a 3D tensor network is very challenging. In this chapter, we develop and benchmark two contraction approaches for iPEPS in 3D. The first approach is based on a contraction of a finite cluster of tensors including an effective environment to approximate the full 3D network. The second approach performs a full contraction of the network by first iteratively contracting layers of the network with a boundary iPEPS, followed by a contraction of the resulting quasi-2D network using the CTM. Benchmark data for the Heisenberg and Bose-Hubbard models on the cubic lattice show that the algorithms provide competitive results compared to other approaches, making iPEPS a promising tool to study challenging open problems in 3D.

The contents of this chapter are based on Ref. [134].

3.1. Introduction

Thanks to significant progress in (i)PEPS algorithms over the past years, they have become a powerful approach for 2D strongly-correlated systems, especially for 2D fermionic and frustrated systems which are notoriously hard to simulate with QMC, see, e.g., Refs. [31–33,35,39,42–46,48–50,135]. Besides the computation of ground states, for which (i)PEPS was originally developed, significant progress has also been achieved in other applications, including the study of thermodynamic properties [118, 136–154], excited states [155, 156], real-time evolution [148,157–159], and open systems [148,160].

The successes of tensor networks for both 1D and 2D quantum systems raise the question of whether these methods can also be applied to 3D quantum systems. It is expected that ground states in 3D typically require a smaller bond dimension than their lower-dimensional counterparts because the entanglement of a site gets shared with more neighbors, such that 3D states typically lie closer to a product state. On the other hand, the presence of additional legs on the tensors implies a higher computational cost for the algorithms, forming one of the main obstacles in their development.

The main challenge of higher dimensional tensor networks is that they cannot be contracted exactly, but only approximately, in contrast to the MPS. Several generalizations of the 2D iPEPS contraction methods discussed in Sec. 2.4 to 3D have been proposed, including CTM in 3D [97, 161] and course-graining methods, such as the HOTRG [101] and other algorithms [162,163]. Generalizations of the MPS-MPO contraction have also been considered. These methods make use of a boundary (i)PEPS instead of a boundary (i)MPS and they have been introduced for 3D classical systems [164–169]. They are also commonly used in the context of imaginary time evolution algorithms of 2D quantum states at zero [54,114,115] and finite temperature [118,136–140,145,148], which effectively corresponds to a contraction of an anisotropic 3D network. Alternative algorithms outside these families have been proposed for 3D networks as well, including embedding a small bulk part in an entanglement bath [149,170], graph-based PEPS [171, 172], isometric tensor networks [173], and TTN [66].

In this chapter, we extend the algorithmic toolbox by proposing two contraction techniques for the study of 3D quantum models. The first method is based on the exact contraction of only a finite number of tensors while using an effective environment to approximate the rest of the network. This approach, which we call cluster contraction in the following, provides a simple, approximate contraction, with the accuracy being controlled by the cluster size. It forms an extension of the approximate two-site cluster contraction used in previous works [171, 172, 174, 175], and a related idea was also used in the CU and

evaluation procedures proposed in Refs. [113, 119, 120] in 2D.

In the second approach, a full contraction of the network is performed by defining a 2D boundary iPEPS and by iteratively absorbing layers of the 3D network (which can be seen as infinite projected entangled-pair operator (iPEPO) layers) into the boundary iPEPS. The contraction is based on the SU scheme [115] which is commonly used in imaginary time evolution algorithms. After convergence of the boundary iPEPS, the 3D tensor network can be effectively represented by a quasi-2D tensor network which is contracted using the CTM algorithm. The accuracy of this SU+CTM algorithm can be systematically controlled by the bond dimensions of the boundary iPEPS and CTM environment tensors.

The chapter is organized as follows: The cluster contractions and the SU+CTM method are introduced in Sec. 3.2 and Sec. 3.3, respectively. In Sec. 3.4 benchmark results for the Heisenberg and the Bose-Hubbard model on the cubic lattice are provided, with a comparison to previous studies based on QMC and other approaches. Finally, we present our conclusions and outlook in Sec. 3.5.

3.2. Cluster contraction

The first contraction method that we will discuss is the cluster contraction. We will make use of iPEPS tensors with the convention that the singular value matrices are kept on each bond, that was discussed in Sec. 2.2.1. In the cluster contraction, instead of performing a full contraction of the network, only a small cluster of the network is contracted exactly, while the rest of the network is taken into account only in an approximate way by absorbing the singular value matrices on the outer legs of the cluster, in a similar spirit as done in the SU imaginary time evolution algorithm. The smallest clusters are the $1 \times 1 \times 1$ and $2 \times 1 \times 1$ clusters depicted in Fig. 3.1 which can be used to evaluate one- and two-site operators respectively. These contractions have a relatively low computational cost of $\mathcal{O}\left(D^7\right)$ and they were used as an approximate contraction method before [171, 172, 174, 175]. We note that these contractions are exact on a Bethe lattice (containing no loops) and have been used frequently in this context [76, 176–179].

While these small clusters have the advantage of having a low computational cost, the involved contraction error may be quite substantial because of their small sizes and because they entirely neglect loops in the network. Furthermore, without a systematic way of increasing the contraction accuracy, it is hard to estimate the magnitude of the contraction error. For these reasons, we will extend

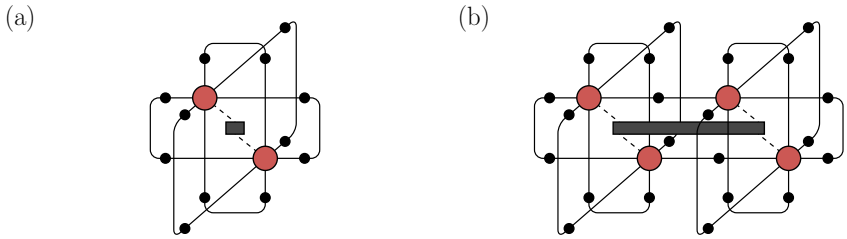

Figure 3.1: Diagrams of the smallest clusters used in the cluster contraction. In (a) the $1 \times 1 \times 1$ cluster is displayed which is used to evaluate one-site operators and in (b) the $2 \times 1 \times 1$ cluster is shown which is used for two-site operators. The black circles represent singular value matrices, which provide an effective environment, approximating the rest of the tensor network surrounding the cluster.

the cluster contractions to larger clusters in this work. Adding an additional layer of tensors around the site(s) on which the operator is measured results in the $3 \times 3 \times 3$ and $4 \times 3 \times 3$ clusters, which are depicted in Fig. 3.2(d)-(e). The computational cost of contracting these clusters has a high scaling of $\mathcal{O}\left(D^{29}\right)$, therefore in practice, it can typically only be used for $D = 2$ (without approximations). In addition, we consider the $2 \times 2 \times 2$ cluster shown in Fig. 3.2(c) with a contraction cost scaling as $\mathcal{O}\left(D^{12}\right)$, which we find offers a good trade-off between accuracy and computational cost.

Cluster contractions are expected to provide reasonable results for states with short-ranged correlations. Their main advantage is that they are simple to implement and, for the smaller clusters, computationally relatively cheap to perform. They can therefore be used for a quick first analysis of a model and to identify parameter regions that could be interesting to simulate using more sophisticated methods, such as the SU+CTM contraction method we introduce in the following.

3.3. SU+CTM contraction

In this section, we introduce a method to perform a full contraction of the infinite 3D network with an accuracy that can be systematically controlled. The approach is based on a boundary iPEPS onto which layers of the 3D network (which can be seen as iPEPO's) are absorbed, see Fig. 3.3, in a similar spirit as done in MPS-MPO based contractions of 2D tensor networks [29] which

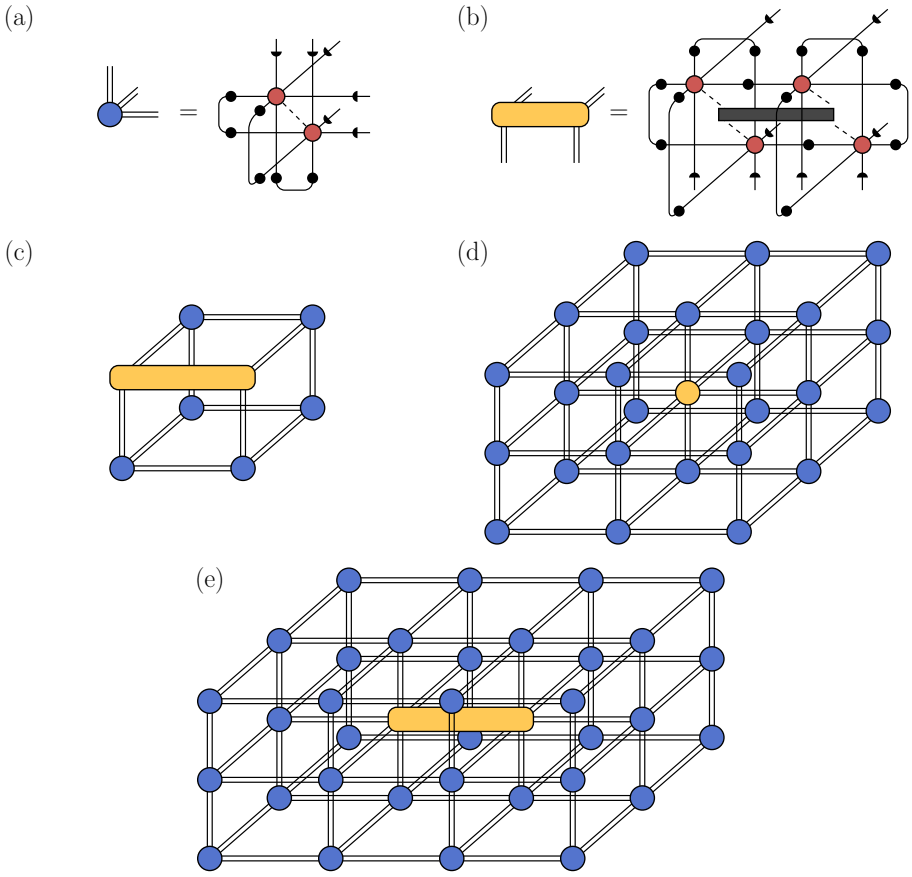

Figure 3.2: Cluster contractions for larger clusters. In (a) and (b) a more compact notation is introduced for graphical clarity. A full black circle represents λ_i, while a half circle represents $\sqrt{\lambda_i}$. Note that keeping the tensors separated typically gives a lower computational cost. In (c) the $2 \times 2 \times 2$ cluster is displayed. In practice, separate diagrams, with the operator inserted on the different bonds of this cluster, are computed and averaged over. Diagrams (d) and (e) show the $3 \times 3 \times 3$ and $4 \times 3 \times 3$ clusters, respectively.

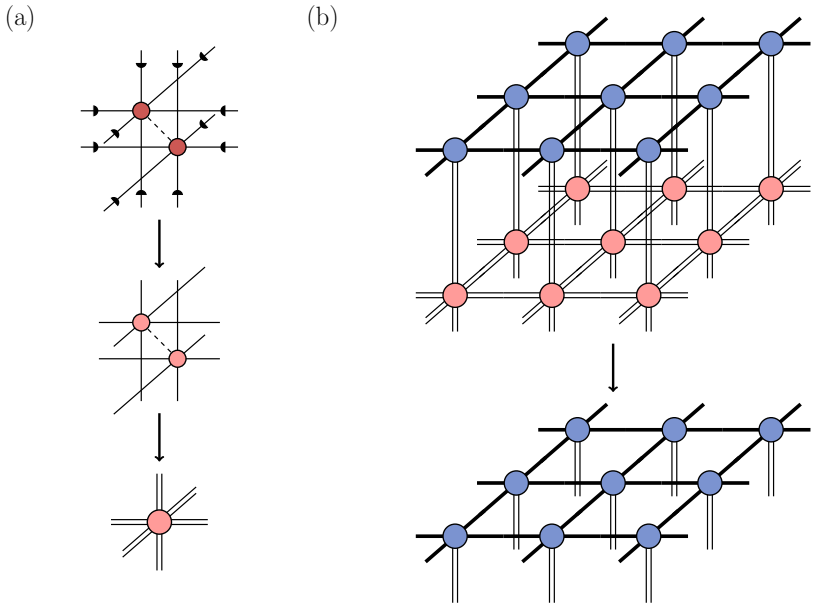

Figure 3.3: To contract the 3D tensor network a 2D boundary iPEPS is defined. For graphical clarity, the bulk 3D iPEPS tensors are represented in the way shown in (a). The half circles represent $\sqrt{\lambda_i}$ which are contracted into the bulk tensors. In (b) a contraction of an iPEPO layer with the boundary iPEPS is displayed.

were discussed in Sec. 2.4.3. Methods based on a boundary iPEPS have been previously developed in the context of 3D classical models [164–169]. While these approaches are typically based on a direct optimization of the boundary iPEPS, here we propose a computationally cheaper scheme that is applicable also for general 3D tensor networks without any mirror or rotational symmetries.

The method is based on iterative absorptions of iPEPO layers onto a boundary iPEPS until convergence is reached. A single iPEPO layer absorption is performed by splitting it into a product of two-body gates which are contracted with the boundary iPEPS, followed by a truncation similar to the one used in the SU imaginary time evolution algorithm. The method is applied twice in opposite directions to obtain an upper and a lower boundary iPEPS, representing the upper and lower half of the 3D network, respectively. The entire 3D network can then be effectively represented by a quasi-2D network made of the two boundary iPEPSs with a bulk iPEPO layer in between. The remaining three-layer network is then contracted using CTM. Each of these stages of this

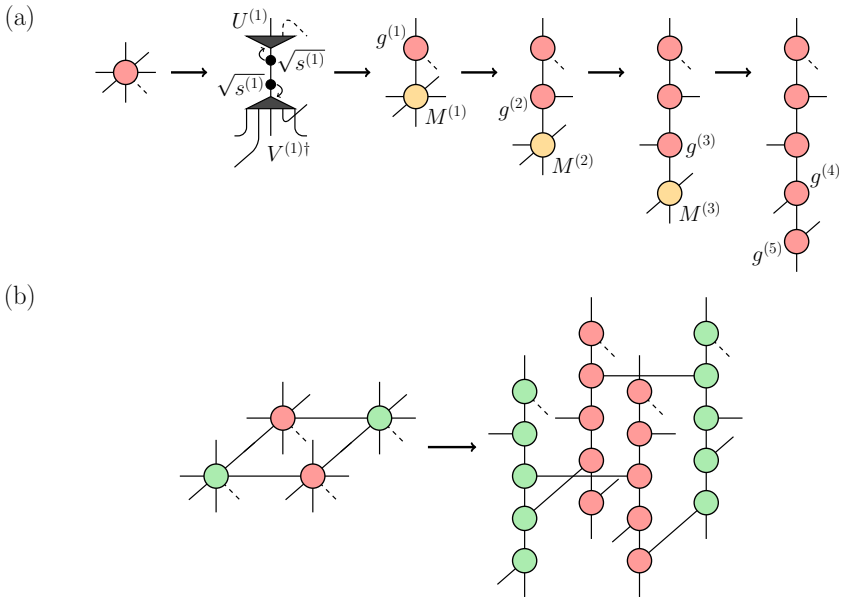

Figure 3.4: In (a) we show the decomposition of a bulk tensor in the 3D iPEPS to rank-3 tensors by sequentially splitting off legs using an SVD. After each SVD the square root of the singular value matrix is absorbed on each side (see main text for more details). In (b) the network of rank-3 tensors that is obtained after the decomposition is shown for a bipartite cubic lattice.

algorithm, which we call the SU+CTM contraction, will be discussed in detail in the following.

3.3.1. SU approach for the boundary iPEPS

We will start by explaining how an absorption of a single iPEPO layer onto the boundary iPEPS is performed. First, the bulk tensors are decomposed in such a way that the transformed network solely consists of rank-3 tensors. This is done by performing a sequence of SVDs in the following way (see also Fig. 3.4(a))

$$T_p^{lrbfud} = \mathbf{T}_{up,lrbfd} = \sum_{a_1} \mathbf{U}^{(1)}_{up,a_1} s^{(1)}_{a_1} \mathbf{V}^{(1)\dagger}_{lrbfd,a_1} =$$
$$= \sum_{a_1} g^{(1)}_{ua_1p} \mathbf{M}^{(1)}_{ra_1,lbfd} = \sum_{a_1 a_2} g^{(1)}_{ua_1p} \mathbf{U}^{(2)}_{ra_1,a_2} s^{(2)}_{a_2} \mathbf{V}^{(2)\dagger}_{lbfd,a_2} =$$

$$= \cdots = \sum_{a_1 a_2 a_3 a_4 a_5} g^{(1)}_{ua_1p} g^{(2)}_{ra_1a_2} g^{(3)}_{la_2a_3} g^{(4)}_{fa_3a_4} g^{(5)}_{ba_4d}, \tag{3.1}$$

where T_p^{lrbfud} is a tensor of the iPEPS network with the square root of the singular value matrices on the virtual bonds absorbed into it. At each decomposition step the square root of the singular value matrix obtained from the SVD is absorbed on each side, so we have $\mathbf{g}^{(j)} = \mathbf{U}^{(j)}\sqrt{s^{(j)}}$ and $\mathbf{M}^{(j)} = \sqrt{s^{(j)}}\mathbf{V}^{(j)\dagger}$. Note that the bond dimension in the middle of each string of rank-3 tensors can become large. In principle, a truncation can be done on the singular value spectrum to reduce the computational cost. In practice, however, it turns out that the CTM procedure, which is discussed in the next section, typically gives the dominant contribution, therefore we do not perform a truncation here.

Figure 3.4(b) shows an example of the network that is obtained from this decomposition for a bipartite lattice. The tensors on the two sublattices are split in different orders, such that the connecting horizontal legs between neighboring pairs of tensors are properly aligned. By thinking of the pairs of rank-3 tensors as two-body gates, we can absorb them onto the boundary iPEPS and perform a truncation in a similar way as in the SU imaginary time evolution algorithm. A single step of this procedure is shown in detail in Figs. 3.5(a)-(d). Both a gate from the bra- and the ket-layer are contracted at the same time. Figure 3.5(e) shows the absorption of the tensors carrying the physical bond, which does not involve a truncation. The maximum bond dimension that is used for the boundary iPEPS is denoted by χ_b. The iterative contraction of the iPEPO layers is continued until convergence is reached in the computed expectation values, which for the benchmark models that will be discussed later is achieved in less than ten iterations. Alternatively, the convergence of the boundary iPEPS singular value matrices can also be used as a convergence criterion. In general, there is no reflection symmetry in the iPEPS. Therefore, a contraction from the opposite direction (using another boundary iPEPS) is also required with the mirrored procedure. The upper and lower boundary iPEPS are initialized by a contraction of the bulk tensors as shown in Fig. 3.5(f). The dominant scaling of the boundary iPEPS contraction is $\mathcal{O}\left(\chi_b^5 D^8 + \chi_b^4 D^{10}\right)$.

3.3.2. Three-layer CTM

In the first part of the algorithm discussed in the previous section, we explained how to obtain the converged upper and lower boundary iPEPS which represent the upper and lower half of the 3D network, respectively. The entire 3D network can then be represented by the double-layer network made of the two boundary iPEPS. For the computation of observables, we additionally keep a single bulk iPEPO layer sandwiched between the two boundary iPEPS, result-

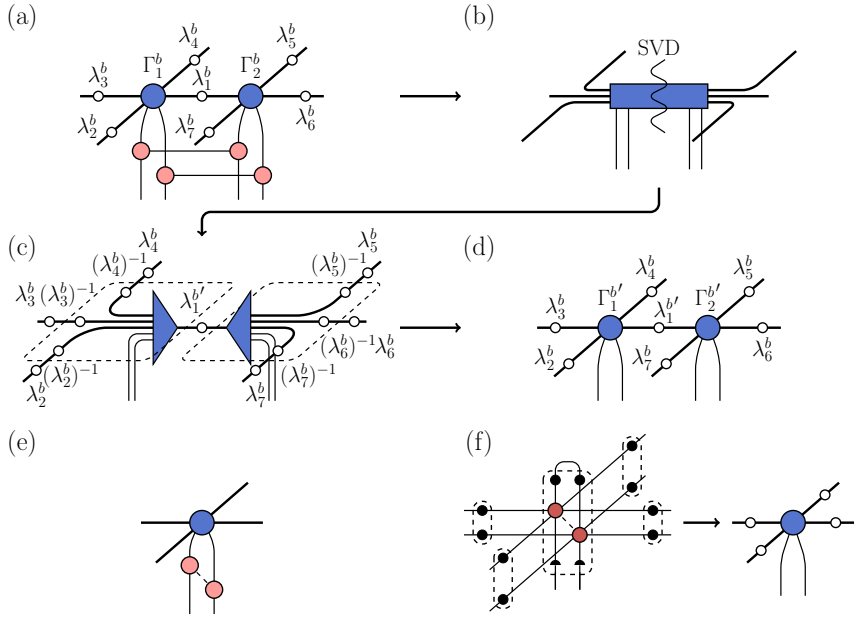

Figure 3.5: In (a)-(d) one step of the SU contraction is displayed. The open circles indicate the singular value matrices λ_i^b that are introduced on the boundary iPEPS. In (a), tensors from the bra- and ket-layer are applied onto the boundary iPEPS tensors as are the singular value matrices from the neighboring bonds. In (b), an (iterative) SVD is performed, after which the identities $\lambda_i^b \left(\lambda_i^b\right)^{-1}$ are inserted on each external bond in (c). In (d) the $\left(\lambda_i^b\right)^{-1}$ are contracted to obtain the new tensors. In (e), an absorption of the tensors carrying the physical bonds is shown which does not require a truncation. (f) shows the initialization of the upper boundary iPEPS tensors which are obtained from a contraction of the bulk iPEPS tensors. On the top, two singular value matrices of the bulk tensors, which are indicated by filled black circles, are used as an effective environment in a similar spirit as in the cluster contraction. The half circles indicate that a square root of the singular value matrix is taken. The initial singular value matrices of the boundary iPEPS are obtained by combining the bra- and ket-layer singular value matrices from the bulk tensors in the plane.

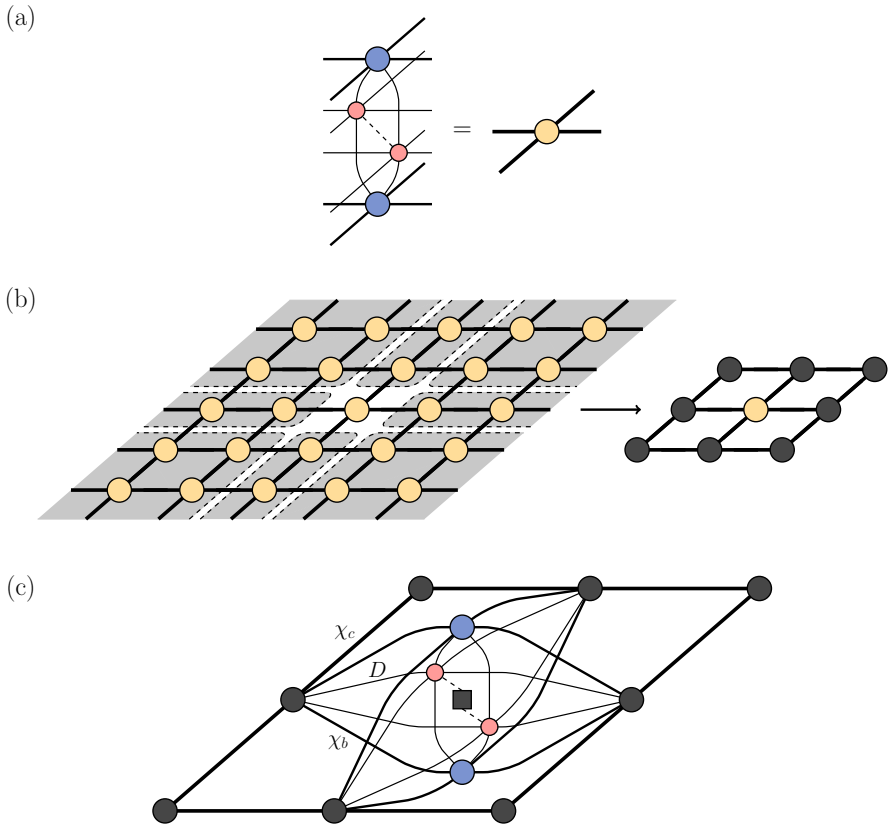

Figure 3.6: The 3D network is effectively represented by a three-layer network, made of the two converged boundary iPEPS with an iPEPO layer of bulk tensors sandwiched in between, shown in (a) for one site of the resulting quasi-2D network. This 2D network is contracted using the CTM yielding the corner and edge tensors surrounding the central site shown in (b), each representing part of the system as indicated by the shaded regions. In (c) the diagram corresponding to the expectation value of a one-site operator is displayed.

ing in the three-layer network shown in Figs. 3.6(a)-(b). In the second part of the algorithm, this quasi-2D network is contracted using the directional CTM method [95], with the renormalization procedure from Ref. [32].[1] We will denote the environment bond dimension by χ_c. The dominant scaling of this three-layer CTM scheme is $\mathcal{O}\left(\chi_c^3\chi_b^4D^4 + \chi_c^2\chi_b^6D^6 + \chi_c^2\chi_b^4D^9\right)$, which makes this the com-

[1] We note that the QR decomposition in Ref. [32] is not required for the computation of the projectors [98].

putationally most expensive part of the SU+CTM contraction algorithm.

Once the environment tensors are converged, expectation values can be evaluated in the standard way, as shown in Fig. 3.6(c) for the example of a one-site operator. For two-site operators, only operators lying within the additional iPEPO layer can be directly computed. To evaluate two-site operators along the direction orthogonal to the iPEPO layer, another SU+CTM contraction is performed using a rotated iPEPS network.

3.4. Results

3.4.1. Heisenberg model

To benchmark the contraction methods, we first present results for the spin-1/2 antiferromagnetic Heisenberg model on the cubic lattice. This model is given by the Hamiltonian

$$H = J \sum_{\langle ij \rangle} \mathbf{S}_i \mathbf{S}_j, \tag{3.2}$$

where $\mathbf{S}_i$ are spin-1/2 operators and $J > 0$. The iPEPS tensors are obtained using the SU imaginary time evolution algorithm. We make use of an ansatz with two independent tensors on the two sublattices. We perform simulations for $D = 2 - 4$ and, in order to reduce the computational cost, we use tensors with a $U(1)$ symmetry [125, 126].

We start by analyzing the convergence behavior of the SU+CTM contraction, first as a function of the CTM environment dimension χ_c, for fixed values of D and χ_b. Figure 3.7 presents results for the energy per site and the average local magnetic moment $m = \frac{1}{N} \sum_{i=1}^{N} |\langle \mathbf{S}_i \rangle|$, where i goes over all the non-equivalent sites in the ansatz (i.e., $N = 2$ in our ansatz with two independent tensors). For both observables, convergence is achieved at moderate values of χ_c, although higher values are required for larger D and χ_b, as is expected. In the following, the value of χ_c is fixed to a sufficiently large value, such that errors from the CTM contraction are negligible.

We next study the convergence of the SU+CTM as a function of the boundary iPEPS bond dimension, χ_b, first focusing on the energy shown in Fig. 3.8(a). The SU+CTM contractions show a rapid convergence as a function of χ_b. The χ_b required for convergence increases with D, still, even for the largest $D = 4$ already a modest $\chi_b \sim 7$ results in a very small contraction error. In the same figure, we also present data obtained from the cluster contractions. The energy

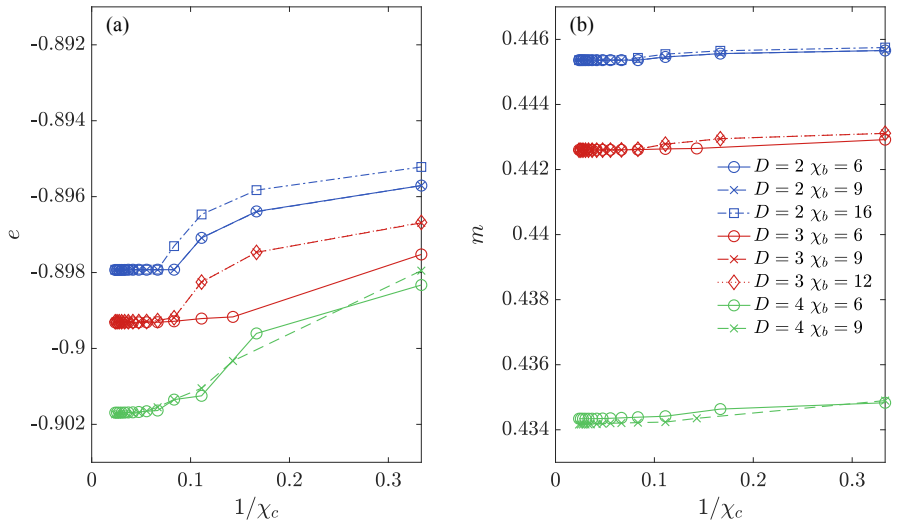

Figure 3.7: Convergence of (a) the energy and (b) the local magnetic moment m as a function of inverse CTM boundary dimension $1/\chi_c$, for various D and χ_b.

obtained with the smallest $2 \times 1 \times 1$ cluster shows a large deviation from the SU+CTM results already for $D = 2$, with only little improvement for higher D. The $2 \times 2 \times 2$ cluster gives a significant improvement over the $2 \times 1 \times 1$ cluster. The $4 \times 3 \times 3$ cluster improves this result further and shows a remarkable agreement with the SU+CTM result for $D = 2$. As mentioned in Sec. 3.2, it was not possible to use this last cluster for higher values of D due to the high computational cost.

For the local magnetic moment m, shown in Fig. 3.8(b), similar observations can be made. The most important difference is that the $2 \times 2 \times 2$ cluster contraction provides a less significant improvement over the smallest $1 \times 1 \times 1$ cluster.

To obtain an estimate of the energy and m in the exact infinite D limit, we attempt an extrapolation based on the effective correlation length ξ_D, an approach that has been used also for iPEPS in 2D [131, 132] and which was explained in Sec. 2.7. The correlation length can be computed from the two leading eigenvalues of the transfer matrix represented by the edge tensors in CTM [180], and ξ_D corresponds to the value for a given D in the $\chi_b, \chi_c \to \infty$ limit.[2] We make use of the finite-size scaling ansatz for the energy and m^2 derived in Ref. [181], where the leading finite-size corrections scale as $1/L^4$ and $1/L^2$, respectively.

[2]The extrapolated values are $\xi_{D=2} = 0.489(1)$, $\xi_{D=3} = 0.528(4)$, and $\xi_{D=4} = 0.81(1)$.

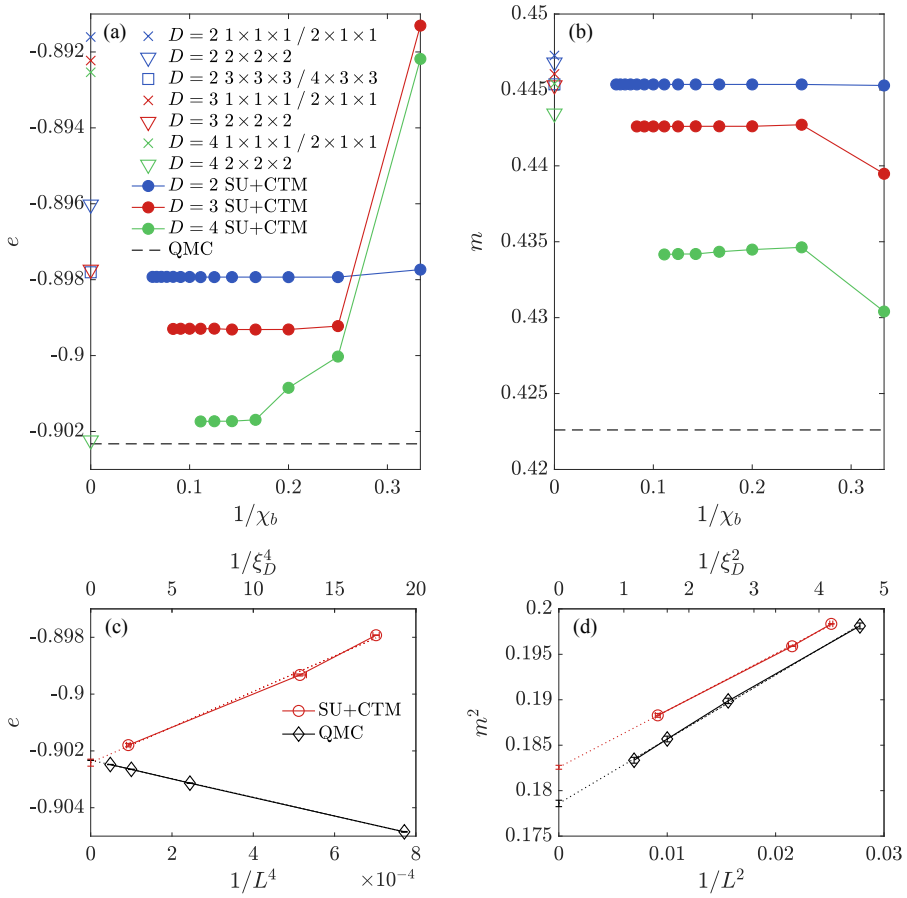

Figure 3.8: The results for (a) the energy and (b) the local magnetic moment m obtained with the SU+CTM method as a function of the inverse boundary iPEPS dimension $1/\chi_b$ and the cluster contractions which are plotted on the vertical axis. The QMC result extrapolated to the thermodynamic limit is shown by the dashed line. In (c) and (d) a linear extrapolation based on the effective correlation length ξ_D is presented for the energy as a function of $1/\xi_D^4$ and for m^2 as a function of $1/\xi_D^2$, respectively. For comparison, finite-size scaling results from QMC using system sizes $L = 6, 8, 10$ and 12 are shown.

In Figs. 3.8(c) and (d) we present the iPEPS results for the energy and m^2 in comparison with QMC data, obtained with the loop algorithm from the ALPS library [182, 183] for system sizes up to $L = 12$ and at sufficiently low temperatures ($T = 0.005J$) such that finite temperature effects are negligible

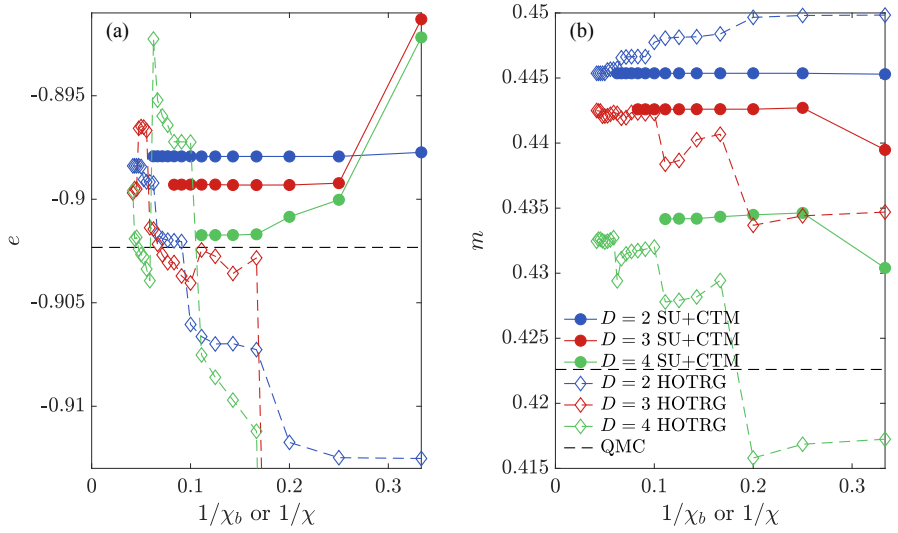

Figure 3.9: The HOTRG results for (a) the energy and (b) the local magnetic moment m as a function of the inverse bond dimension $1/\chi$ compared to the SU+CTM results as a function of $1/\chi_b$.

compared to the error bars. For the energy, we find a good agreement between the extrapolated iPEPS, $-0.9024(1)$, and QMC result, $-0.902325(11)$. The estimate for m^2 obtained with iPEPS, 0.1826(2), is slightly higher than the QMC value, 0.1786(4), which is most likely due to the local SU optimization scheme used here (which typically tends to overestimate the order parameter). Still, the relative error is only $\approx 2\%$, and we expect that the accuracy can be further improved by using more accurate optimization schemes.

Finally, in Fig. 3.9, we compare our SU+CTM results to a contraction of the converged iPEPS tensors using HOTRG [101]. Here we use a modified approach adapted to the anisotropic case where the projectors are computed in a similar way as in Ref. [107], which was discussed in Sec. 2.4.2. We observe that the convergence of the HOTRG results is strongly irregular and exhibits several plateaus, in contrast to the SU+CTM results which exhibit a fast and regular convergence. One possible reason for this behavior is that the distribution of the singular values obtained in HOTRG decays only very slowly, much slower than the spectrum in the SU+CTM approach. While there seems to be a tendency that HOTRG approaches the SU+CTM results, it was not possible to reach high enough χ to fully converge due to the high computational cost.

3.4.2. Bose-Hubbard model

As a second benchmark case, we consider the Bose-Hubbard model defined by the Hamiltonian

$$H = -t \sum_{\langle ij \rangle} b_i^\dagger b_j + \frac{U}{2} \sum_i n_i(n_i - 1) - \mu \sum_i n_i, \tag{3.3}$$

with t the hopping amplitude, U the on-site interaction, μ the chemical potential, $b_i^\dagger$ (b_i) the bosonic creation (annihilation) operator and $n_i = b_i^\dagger b_i$ the number operator. At zero temperature the model exhibits Mott insulating phases with integer particle filling for $t \ll U$ and a superfluid phase (SF) for $t \gg U$ [14].

We again make use of the SU imaginary time evolution to obtain the iPEPS tensors. To perform the iPEPS simulations with finite local Hilbert spaces we introduce a cutoff on the maximum occupation number on each site. The size of this cutoff is chosen such that the induced error is negligible. For the simulations of the $n = 1$ and $n = 2$ Mott lobes, a cutoff of $n_{\max} = 3$ and $n_{\max} = 4$ are used, respectively. To obtain the data in one of the phases, simulations are started deep in this phase and the converged iPEPS at one data point is used as the initial state of the SU optimization at the next data point. For a given value of D, the phase transition point can be determined by locating the intersection of the iPEPS energies of the two phases. In contrast to the Heisenberg case in the previous section, the $U(1)$ symmetry cannot be exploited here because it is broken in the superfluid phase. For this reason, the maximal bond dimension we consider here is $D = 3$. The SU+CTM contractions are performed using $\chi_b = 8$ and $\chi_c = 21$, which are sufficiently large to make the remaining finite χ_b and χ_c errors much smaller than the symbol sizes.

We first consider two selected cuts in the phase diagram at the tip of the first and second Mott lobes. Figure 3.10 shows a comparison between results obtained from the SU+CTM and cluster contractions for the energy, particle number, and the order parameter $\langle b^\dagger \rangle$ close to the tip of the $n = 1$ lobe for fixed $\mu/U = 0.4$ as a function of t/U. For the energy, the $2 \times 1 \times 1$ cluster shows a large deviation compared to the other results. The $2 \times 2 \times 2$ cluster gives a significant improvement and there is only a slight shift in the location of the phase transition compared to the SU+CTM contraction (which is mostly due to the small angle at which the energies of the two phases intersect). For the particle number and the order parameter a much smaller improvement is seen when going from the $1 \times 1 \times 1$ cluster to the $2 \times 2 \times 2$ cluster when compared to the SU+CTM result, as previously observed for m in the Heisenberg model. Still, the absolute error on the scale shown in Figs. 3.10(b)-(c) is small. Figure 3.11 shows results close to the tip of the second Mott lobe at fixed $\mu/U = 1.45$, for which similar observations can be made.

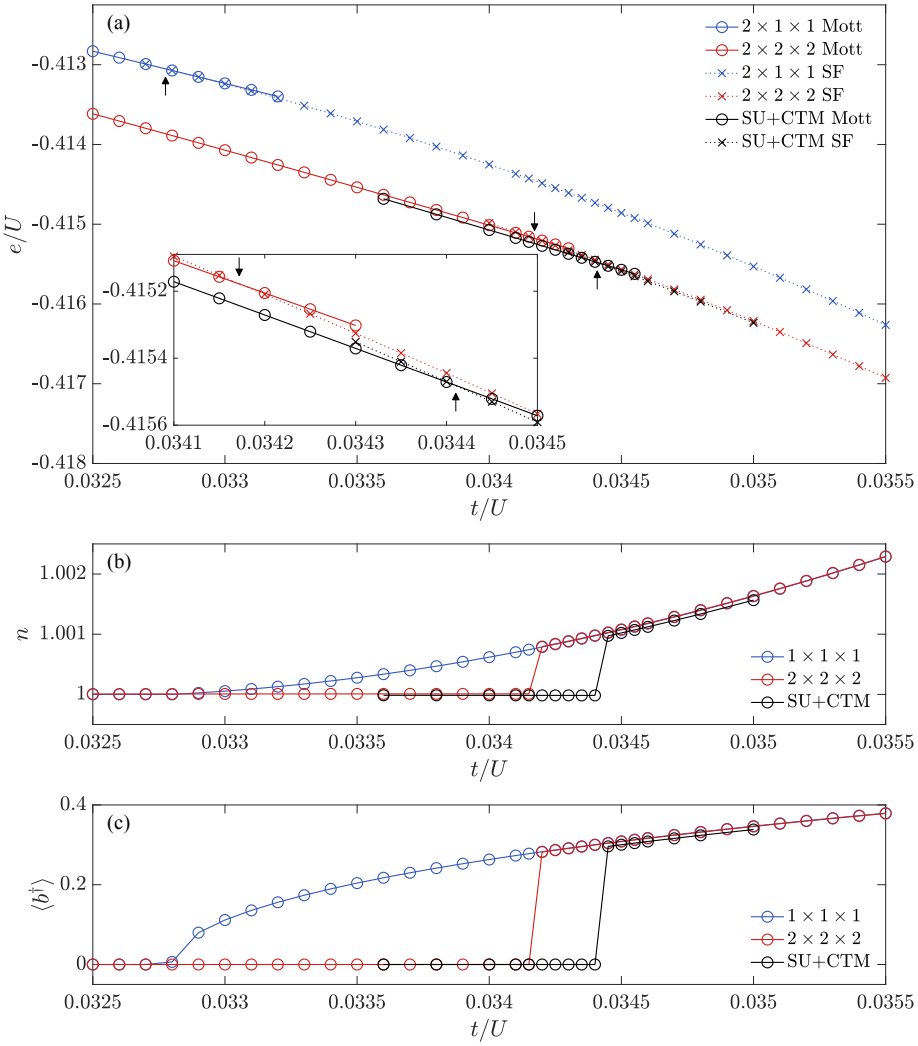

Figure 3.10: A cut through the phase diagram at the tip of the first Mott lobe for fixed $\mu/U = 0.4$ as a function of t/U obtained with $D = 3$. In (a) the energy of both phases is shown obtained using the cluster and SU+CTM contraction. The inset displays a zoom of the same results close to where the contractions indicate the phase transition to take place, marked by arrows. In (b) and (c) the particle number and order parameter $\langle b^\dagger \rangle$ of the lowest energy state are shown, respectively.

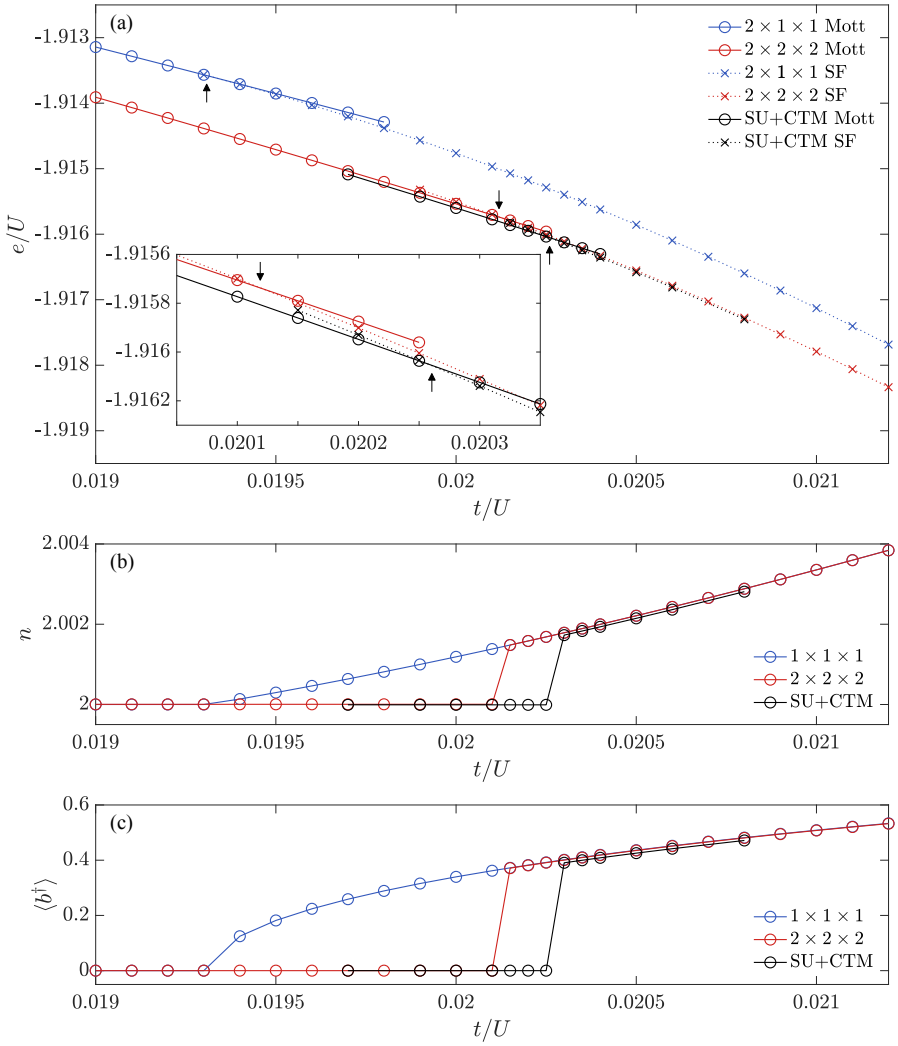

Figure 3.11: Same as in Fig. 3.10 for a cut through the phase diagram at the tip of the second Mott lobe with fixed $\mu/U = 1.45$.

We note that the jump in the order parameter $\langle b^\dagger \rangle$ at the phase transition in the $2 \times 2 \times 2$ cluster and the SU+CTM results seem to indicate that the transition is of first order, whereas the transition is known to be of second order. This is most likely an artifact of the SU optimization scheme used here which, since it is a local update, does not accurately reproduce the diverging correlation length

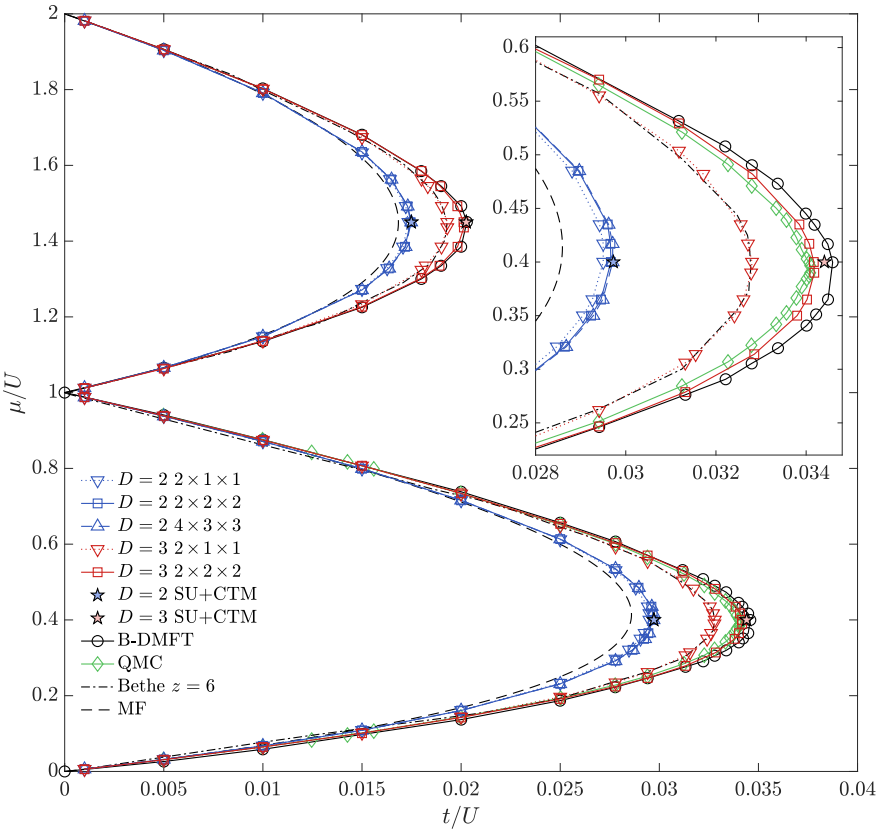

Figure 3.12: Ground state phase diagram of the first two Mott lobes of the Bose-Hubbard model obtained with the cluster and SU+CTM contraction. For comparison, results from B-DMFT [184], QMC [185], an exact solution for a Bethe lattice with coordination number $z = 6$ [186], and static MF theory are shown.

across a second-order transition. The accuracy of the order parameter around the transition could be improved using more accurate optimization schemes [54, 114, 119, 124]. Still, we can nevertheless obtain an accurate estimate of the critical point based on the intersection of the energies when compared to QMC as we show in the following.

By performing simulations along additional cuts, we can construct the ground state phase diagram for the first two Mott lobes shown in Fig. 3.12. We have restricted these additional simulations to the cluster contractions, which are

computationally substantially cheaper than the SU+CTM method, and, as we have found previously, the $2 \times 2 \times 2$ cluster already provides an estimate which is close to the SU+CTM result. For comparison, we added previous results from bosonic dynamical mean-field theory (B-DMFT) [184], QMC [185], an exact solution on the Bethe lattice for coordination number $z = 6$ [186], and the mean-field result (MF). While the $D = 2$ phase boundary only provides a slight improvement over the MF result, the data obtained for $D = 3$ with the $2 \times 2 \times 2$ cluster and the SU+CTM contraction show a close agreement with the QMC results. This demonstrates that already a relatively small bond dimension is sufficient to obtain the phase diagram with a remarkable accuracy that is competitive or even better than B-DMFT. Another observation we can make is the agreement between the $D = 3$ results obtained by the $2\times1\times1$ cluster and the $z = 6$ Bethe lattice results. This is because the simulation based on the SU imaginary time evolution approach brings the iPEPS to a quasi-canonical form, see Sec. 2.5.1. Combined with the $2 \times 1 \times 1$ contraction this is equivalent to an iPEPS simulation on the Bethe lattice.

3.5. Summary and discussion

In this chapter, we have presented two iPEPS contraction approaches to study 3D quantum many-body systems. The cluster contraction provides an approximation to the 3D contraction by only contracting a small cluster of tensors exactly while the rest of the network is taken into account approximately via the singular values on the boundary bonds of the cluster. The contraction error for the smallest $1\times1\times1$ and $2\times1\times1$ clusters, which have been used in previous studies [171, 172, 174, 175], can be quite large. A considerable improvement (at least for the energy) is obtained when using the larger $2 \times 2 \times 2$ cluster which is computationally still affordable. The SU+CTM method enables a full contraction of the 3D tensor network by iteratively absorbing iPEPO layers with a lower and upper boundary iPEPS, and by contracting the resulting quasi-2D tensor network using CTM. The accuracy can be systematically controlled by χ_b and χ_c, the bond dimension of the boundary iPEPS and the CTM environment tensors, respectively. A fast convergence as a function of χ_b and χ_c is observed, significantly outperforming a HOTRG contraction for the Heisenberg model. For the Bose-Hubbard model, we found that already a relatively small $D = 3$ yields a phase diagram that is in close agreement with QMC. We have shown that the combination of the two contraction approaches provides a practical way to compute a phase diagram at a reasonable computational cost.

There are various ways in which the accuracy of the methods can be further

improved. For the optimization of the iPEPS tensors, a higher accuracy can be obtained by using FU [54], or FFU [114], which, for each truncation step in the imaginary time evolution, takes the entire wave function into account, in contrast to the local SU update. However, the computational cost of these approaches is also substantially higher than the SU scheme. Alternatively, a CU [113,119,120], which only takes a cluster of tensors into account to perform a truncation, may provide an optimal trade-off between accuracy and computational cost. Schemes based on a direct energy minimization, e.g., based on automatic differentiation [124], may be another interesting option. The SU+CTM contraction itself could in principle also be further improved by replacing the SU with a full (or cluster) update scheme, albeit also here at the expense of a higher computational cost.

We expect these methods to provide a promising path towards simulating challenging 3D quantum systems, such as, e.g., the pyrochlore Heisenberg model, layered systems, and ultra-cold atoms in optical lattices, especially for cases that are out of reach by QMC due to the negative sign problem. Finally, we note that these approaches can also be extended to the finite temperature case or to other types of lattices in a rather straightforward way, as was done in 2D.

CHAPTER 4

Contraction approaches for layered systems

Strongly-correlated layered 2D systems are of central importance in condensed matter physics, but their numerical study is very challenging. Motivated by the enormous successes of tensor networks for 1D and 2D systems, we develop an efficient tensor network approach based on iPEPS for layered 2D systems. Starting from an anisotropic 3D iPEPS ansatz, we propose a contraction scheme in which the weakly interacting layers are effectively decoupled away from the center of the layers, such that they can be efficiently contracted using 2D contraction methods while keeping the center of the layers connected in order to capture the most relevant interlayer correlations. We present benchmark data for the anisotropic 3D Heisenberg model on a cubic lattice, which shows close agreement with QMC and full 3D contraction results. Finally, we study the dimer to Néel phase transition in the SSM with interlayer coupling, a frustrated spin model that is out of reach of QMC due to the negative sign problem.

The contents of this chapter are based on Ref. [187].

4.1. Introduction

A special and highly relevant class of 3D quantum systems is formed by layered 2D systems, in which the effective intralayer couplings are much stronger than the interlayer ones. Important realizations include the cuprate high-T_c superconductors [58] as well as various quasi-2D frustrated magnets such as Kagomé [60], triangular [61, 188–191], SSM [59, 192, 193], and honeycomb lattice compounds [62, 194–196]. While pure 2D models often already capture the relevant physics of these systems, the interlayer couplings can play an important role on the quantitative level. For example, they lead to a finite Néel transition temperature in layered square lattice Heisenberg models as opposed to the pure 2D case [197], or they may play a significant role in the competition of low-energy states in the 2D Hubbard model [35]. Thus, accurate tensor network approaches to study these systems would be highly desirable.

In this chapter, we introduce an efficient tensor network algorithm for layered 2D systems, called the layered corner transfer matrix (LCTM) method, which is substantially simpler and computationally cheaper than full 3D approaches. Motivated by the layered nature of these systems, we start from an anisotropic iPEPS ansatz, i.e., with a small interlayer bond dimension D_z compared to the intralayer bond dimension D_{xy}, which control the accuracy of the ansatz. The main idea of the algorithm is to contract the 3D tensor network by (1) performing an effective decoupling of the layers away from the center of each layer, (2) contracting the individual decoupled layers using the standard 2D CTM method [32, 94, 95], and (3) contracting the remaining tensor network, formed by the contracted layers connected with a finite bond dimension $D_z > 1$ in the center of each layer. A core ingredient of the approach is the effective decoupling procedure that we implement based on an iterative FU truncation scheme [54, 114].

The chapter is organized as follows. In Sec. 4.2 the algorithm will be discussed. We present benchmark results in Sec. 4.3 for the anisotropic Heisenberg model on a cubic lattice, which show close agreement with a full 3D contraction and with QMC data already for small D_z. As a more challenging example we consider a frustrated spin model, the SSM with interlayer coupling, for which QMC fails due to the negative sign problem. Finally, in Sec. 4.4 we draw our conclusions and highlight directions for future improvements and extensions of the LCTM approach.

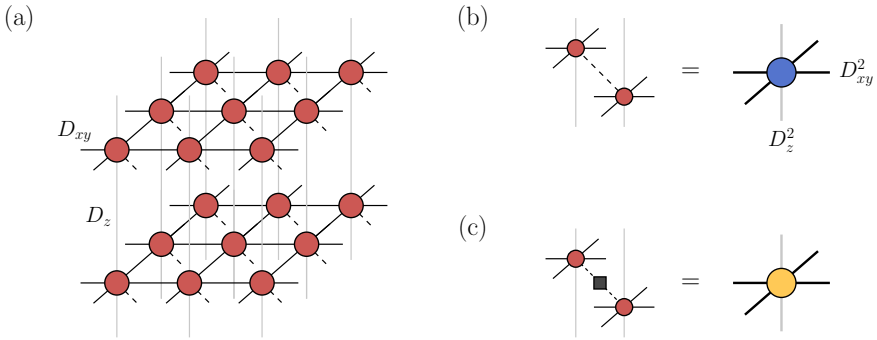

Figure 4.1: (a) Anisotropic 3D iPEPS ansatz with intralayer and interlayer bond dimensions D_{xy} and D_z, respectively. (b) The norm tensor represents the combined bra- and ket-tensors on each site where pairs of auxiliary indices are combined into new auxiliary indices with dimensions D^2_{xy} and D^2_z, respectively. (c) Same as in (b) but with a local operator between the bra- and ket-tensors for the evaluation of a local expectation value.

4.2. LCTM method

We consider a cubic iPEPS ansatz, shown in Fig. 4.1(a), in which each tensor has seven indices: one physical index carrying the local Hilbert space of a site, four indices with bond dimension D_{xy} connecting to the intraplane nearest-neighbor tensors, and two indices of dimension D_z connecting to the tensors in the neighboring planes. We choose $D_{xy} \geq D_z$ motivated by the anisotropic nature of layered 2D systems. In the limit of $D_z = 1$, the ansatz corresponds to a product state of 2D iPEPS layers, i.e., a state without entanglement between the layers (but with entanglement within the layers, controlled by D_{xy}).

The main challenge of a 3D tensor network algorithm is the efficient, approximate contraction of the 3D tensor network, which is needed to compute, e.g., a local expectation value. Let us consider computing the norm of the wave function. The corresponding tensor network is depicted in Fig. 4.2(a), where the norm tensors (blue) represent the combined bra- and ket-tensors on each site as shown in Fig. 4.1(b). To compute a local expectation value, we can simply put an operator between the local tensors as shown in Fig. 4.1(c) and replace the norm tensor with this new tensor at the desired location.

In the simplest case, for $D_z = 1$, this network consists of independent 2D square lattice networks that can be efficiently contracted using the CTM method [32, 94,95]. For the case $D_z > 1$, a full 3D contraction algorithm as in Chap. 3 could

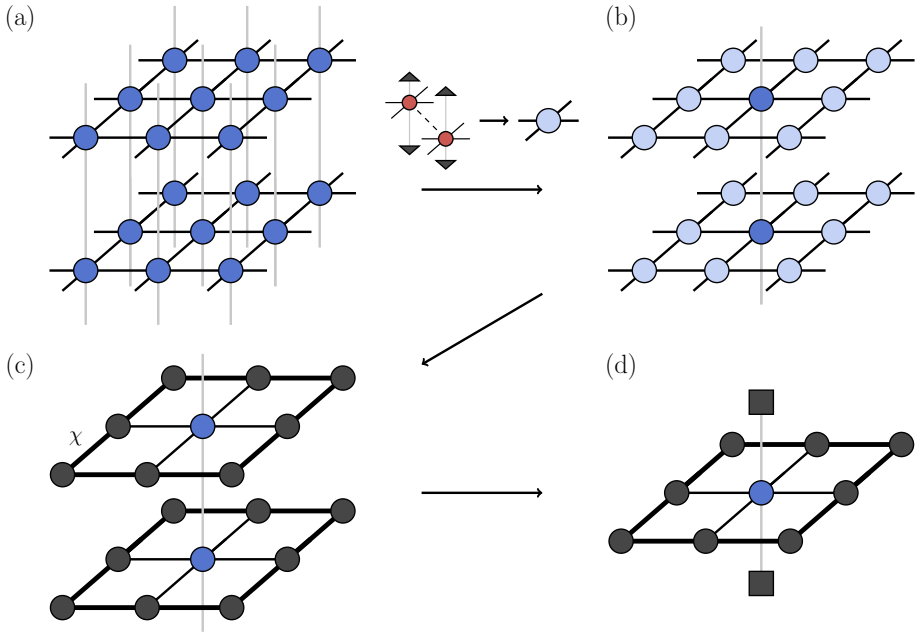

Figure 4.2: The main steps of the LCTM contraction method. (a) 3D tensor network representing the norm. (b) Tensor network with decoupled layers away from the center, obtained by a projection (black triangles) of the vertical indices of bra- and ket-tensors in (a) onto $D_z = 1$ (except in the center). (c) The decoupled 2D layers are contracted using the CTM method, which yields the environment tensors around the central tensor, i.e., four corner and four edge tensors (in black), with an accuracy controlled by the boundary bond dimension χ. (d) The infinite central chain with contracted layers can be evaluated by replacing the neighboring layers by the left- and right-dominant eigenvector (black squares) of the transfer matrix represented by a contracted layer. A local expectation value can be computed by replacing the central norm tensor by the yellow tensor shown in Fig. 4.1(c).

be used. This, however, is computationally expensive, and we thus follow a more efficient strategy here, exploiting the anisotropic nature of the ansatz. The main idea is to project the vertical indices of the bra- and ket-iPEPS tensors away from the center of each layer onto $D_z = 1$ (see details below), while keeping the full bond dimension $D_z > 1$ on the tensors in the center; see Fig. 4.2(b). This leads to an effective decoupling of the 2D layers away from the center, such that the standard 2D CTM approach can be used to contract them (Fig. 4.2(c)) while the most relevant interlayer correlations are still taken into account by

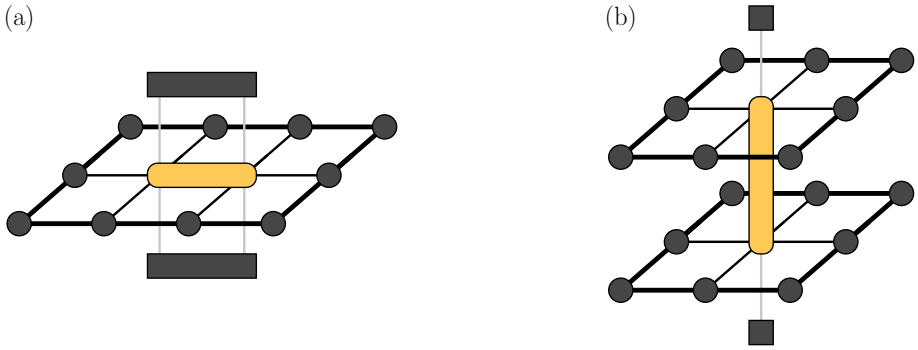

Figure 4.3: Relevant diagrams to compute (a) intra- and (b) interlayer nearest-neighbor observables, where the yellow tensor is obtained from contracting neighboring bra- and ket-tensors with a two-site operator in between.

the vertical connections of the tensors in the center. Since the bonds in the z-direction carry only little entanglement, the projection onto $D_z = 1$ away from the center is expected to induce only a small error on a local expectation value measured in the center. After contracting each layer, the resulting tensor network corresponds to an infinite 1D chain in the vertical direction with bond dimension D_z^2, which can be evaluated by sandwiching the central layer between the left- and right-dominant eigenvector of the corresponding transfer matrix (represented by a contracted layer), as shown in Fig. 4.2(d).

A core ingredient of the algorithm is the projection step from $D_z > 1$ to $D_z = 1$. We use a scheme based on a FU truncation [54, 114], a technique that is also applied in the context of imaginary time evolution algorithms to truncate a bond index in an iPEPS, see App. 4.A.1. The FU does require the environment tensors, which we initially do not have. We thus start from an initial approximate projection based on the SU approach [115], which only considers local tensors for the truncation, from which the environment for the FU projection is computed. To improve the accuracy of the truncation, one can repeat the computation of the environment iteratively. In practice, for the models considered here, we find that one FU iteration is sufficient to reach convergence.

The accuracy of the LCTM method is controlled by the boundary bond dimension χ and by the number of $D_z > 1$ connections kept in the center. Here, we focus on the simplest case, where we only keep the connections on the central tensor for the evaluation of one-site observables and interplane two-site observables (see Fig. 4.3(b)), which we find is sufficient in the limit of weak interlayer coupling, as we will show in our benchmark results. For intralayer two-site observables we keep two connections, as depicted in Fig. 4.3(a). The computational

cost of these contractions are $\chi^3 D_{xy}^4 + \chi^2 D_{xy}^6 D_z^2$ and $\min\left[\chi^3 D_{xy}^6, \chi^3 D_{xy}^4 D_z^4\right]$, respectively. In App. 4.A.4, we discuss other layer decoupling approaches and we also consider a scheme with more connections, which is more accurate, but also computationally more expensive.

The LCTM contraction method can not only be used for the computation of observables, but also in combination with accurate optimization schemes (to find the optimal variational parameters in the tensors for a given Hamiltonian), e.g., in an imaginary time evolution with FFU [114] or in energy minimization algorithms [122–124]. We further note that the LCTM method can be extended to arbitrary unit cell sizes in a similar way to the standard CTM in 2D [32,96].

4.3. Results

4.3.1. Anisotropic Heisenberg model

To benchmark the method, we consider the anisotropic 3D Heisenberg model on a cubic lattice given by the Hamiltonian

$$H = J_{xy} \sum_{\langle ij \rangle_{xy}} \mathbf{S}_i \mathbf{S}_j + J_z \sum_{\langle ij \rangle_z} \mathbf{S}_i \mathbf{S}_j, \tag{4.1}$$

with J_{xy} the intralayer and J_z the interlayer coupling strengths and $\mathbf{S}_i$ spin $S = 1/2$ operators. We use an iPEPS ansatz with two tensors, one for each sublattice, to capture the long-range antiferromagnetic order. The iPEPS is optimized with the FFU imaginary time evolution algorithm [114], starting from initial tensors obtained with SU optimization [115]. In the CTM approach, we keep a sufficiently large boundary bond dimension χ, such that finite-χ effects are negligible (see App. 4.A.4). To improve the computational efficiency, tensors with implemented $U(1)$ symmetry [125,126] are used.[1] We compare our results to the ones computed with the full 3D contraction approach (SU+CTM) from Sec. 3.3 and with QMC results based on the directed loop algorithm from the ALPS library [182, 183] (obtained at a sufficiently low temperature of $T = 0.005 J_{xy}$). To extrapolate the QMC data to the thermodynamic limit, a finite size scaling analysis is performed using the scaling relations for the isotropic 3D Heisenberg model on the cubic lattice from Ref. [181] for lattices of size $L \times L \times L/2$ with L up to 20 for $J_z/J_{xy} = 0.05$ and 0.1, and with $L \times L \times L$ lattices for a maximum L of 12 for $J_z/J_{xy} = 0.2 - 0.4$.

[1] We note that the SU(2) spin symmetry is broken in the ground state.

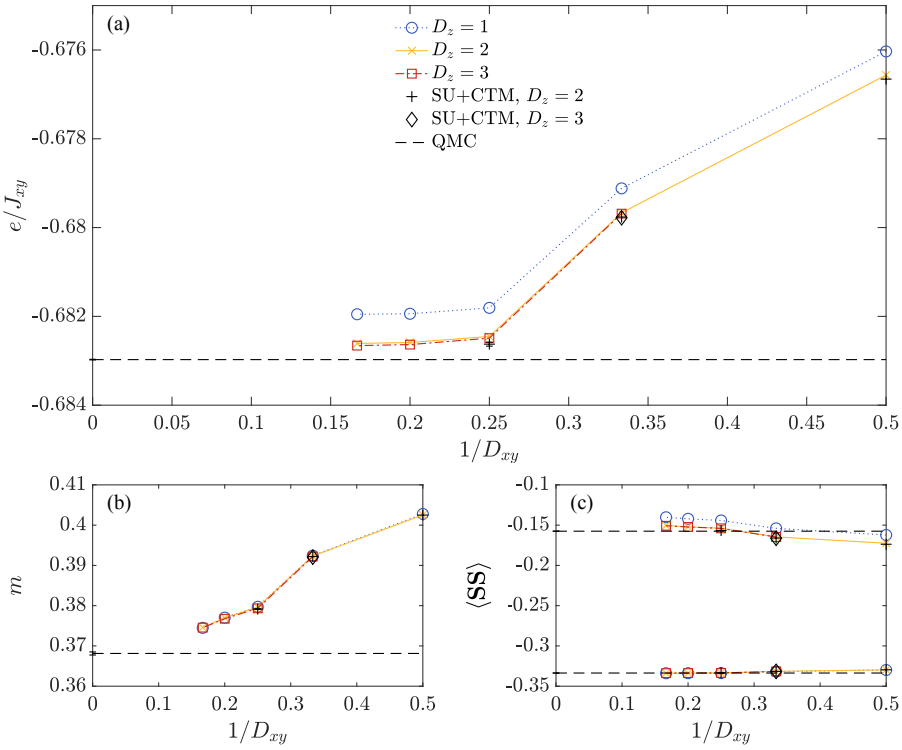

Figure 4.4: Results for the anisotropic 3D Heisenberg model with $J_z/J_{xy} = 0.1$ as a function of $1/D_{xy}$, obtained for $D_z = 1 - 3$. For comparison, the extrapolated QMC results are indicated by the horizontal dashed lines with the extrapolation error bar shown on the y-axis, which is of the order of the line width in (a) and (c). Data based on the full 3D contraction approach (SU+CTM) is shown by the black symbols. (a) Energy per site e in units of J_{xy}. (b) Local magnetic moment m. (c) Nearest-neighbor spin-spin correlator in the z-direction, $\langle \mathbf{SS} \rangle_z$ (top), and in the xy-direction, $\langle \mathbf{SS} \rangle_{xy}$ (bottom).

We first consider the results for the energy per site, e, for $J_z/J_{xy} = 0.1$ in Fig. 4.4(a), plotted as a function of inverse bond dimension D_{xy} for different values of D_z. Already a product of iPEPS layers ($D_z = 1$) yields a value that is remarkably close to the QMC result, with a relative error of only 0.15% for $D_{xy} = 6$. When D_z is increased to 2, a significant improvement is found and the relative error at $D_{xy} = 6$ is reduced to 0.05%, while a further increase to $D_z = 3$ only yields a small enhancement. Overall, the improvement of the variational energy is clearly larger when increasing D_{xy} (at least up to 4) compared to

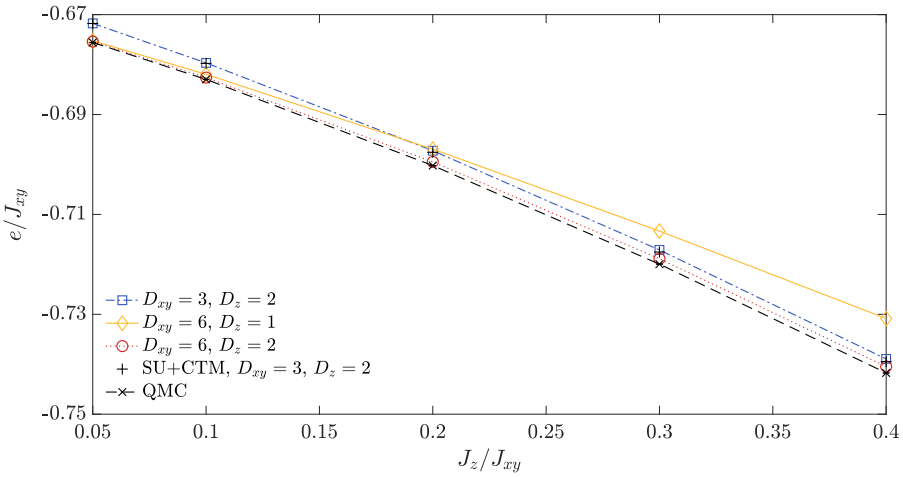

Figure 4.5: Energy per site as a function of J_z/J_{xy} for different sets of bond dimensions, in comparison with data from a full 3D contraction (SU+CTM) and extrapolated QMC results.

the improvement when increasing D_z, which further motivates the use of an anisotropic ansatz with $D_{xy} > D_z$. Comparing the LCTM scheme with the full 3D contraction (SU+CTM) only a small difference between the two methods is found.

Results for the local magnetic moment m are shown in Fig. 4.4(b). Whereas m systematically approaches the QMC result with increasing D_{xy}, the dependence on D_z is small, suggesting that the reduction of the magnetic moment is predominantly due to the intraplane quantum fluctuations. The relative error of m at $D_{xy} = 6$ and $D_z = 3$ is 1.7(1)%. In Fig. 4.4(c) we present results for the nearest-neighbor spin-spin correlators in the intraplane and z-direction. The former is more accurately reproduced, which is a natural consequence of the fact that the latter enters with a prefactor $J_z/J_{xy} = 0.1$ in the optimization of the tensors. Still, we find that the QMC result is approached with increasing D_z at large D_{xy} (note that increasing the two bond dimensions has an opposite effect on the change in the $\langle \mathbf{SS} \rangle_z$ correlator, see App. 4.A.4).

In Fig. 4.5 we present results for the energy per site as a function of J_z/J_{xy}, for selected values of D_{xy} and D_z. Starting with the data for $D_{xy} = 3$ and $D_z = 2$ we find that the deviation with respect to the SU+CTM result slightly increases with increasing J_z/J_{xy}, although the deviation remains small even at a relatively large value of $J_z/J_{xy} = 0.4$. For a small ratio $J_z/J_{xy} = 0.05$, a product of iPEPS layers ($D_z = 1$) for $D_{xy} = 6$ already provides an energy close

to the QMC result, with only a small improvement when increasing D_z to 2. In contrast, for $J_z/J_{xy} = 0.4$ the energy gain is large when increasing D_z, which is a natural consequence of the stronger entanglement between the layers for larger interlayer coupling.

4.3.2. Shastry-Sutherland model

We next consider a more challenging problem, the Shastry-Sutherland model [198] (SSM) - a frustrated spin model relevant for $SrCu_2(BO_3)_2$ [59] for which QMC suffers from the negative sign problem [199]. It is described by square lattice layers of coupled dimers with Hamiltonian

$$H = J \sum_{\langle ij \rangle} \mathbf{S}_i \mathbf{S}_j + J' \sum_{\langle ij \rangle'} \mathbf{S}_i \mathbf{S}_j + J'' \sum_{\langle ij \rangle''} \mathbf{S}_i \mathbf{S}_j, \tag{4.2}$$

with J and J' the intra- and interdimer couplings, $\mathbf{S}_i$ spin $S = 1/2$ operators, and with an additional interlayer coupling J'' to the model as in Ref. [70]. We make use of a cubic iPEPS ansatz, with one tensor per dimer as previously done for the 2D model [69]. To improve the efficiency we use tensors with $U(1)$ symmetry.

We consider the dimer to antiferromagnetic phase transition for fixed J'/J while varying J''/J and compare it to fourth-order series expansion (SE) results [70]. The location of the phase transition is determined from the intersection of the exact energy of the dimer state ($-0.375J$ per site) with the energy of the antiferromagnetic state. To obtain the energies of the antiferromagnetic states across the phase transition, we initialize the FFU optimizations from states obtained in the antiferromagnetic phase. Thanks to hysteresis effects across the first order phase transition, the state remains in this phase even beyond the critical coupling. For $J'/J = 0.61$, shown in Fig. 4.6(a), we find a close agreement with the SE result at large bond dimensions and also based on an extrapolation in inverse bond dimension.[2] For larger values (within the dimer phase) no estimate from SE exists due to convergence problems [70]. With iPEPS, in contrast, we can accurately determine the transition, as shown in Fig. 4.6(b) for $J'/J = 0.66$. We will study the model in more detail in Chap. 5.

[2]The extrapolation of the energy is done based on an approach similar to the inverse bond dimension extrapolation discussed in Sec. 2.7. Since we have two bond dimensions, we perform a linear extrapolation in $1/\kappa$, with $D_{xy} = \kappa$ and $D_z = (\kappa - 1)/2$, using the data for ($D_{xy} = 5$, $D_z = 2$), ($D_{xy} = 7$, $D_z = 3$) as well as the mean value of ($D_{xy} = 6$, $D_z = 2$) and ($D_{xy} = 6$, $D_z = 3$). Since the energy typically converges faster than linearly in $1/D$, we take the average of the extrapolated value and largest D value as the infinite D estimate and its difference to the largest D value as an estimate of the error bar.

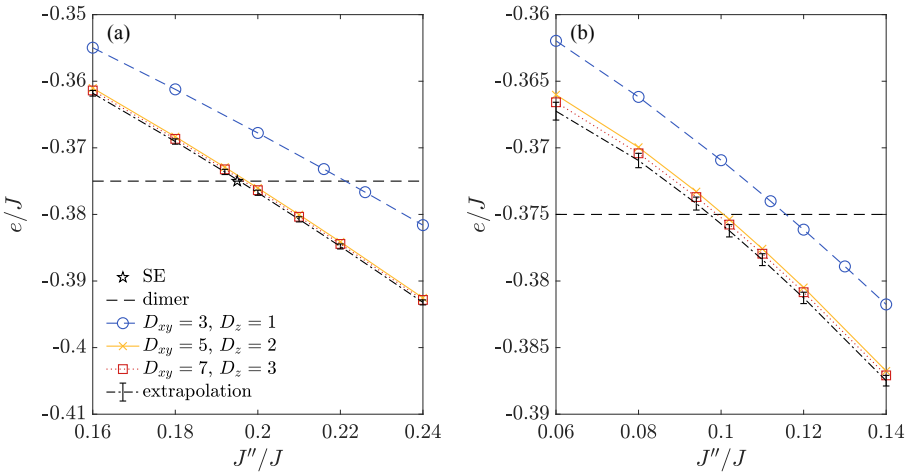

Figure 4.6: Energies per site as a function of J''/J of the SSM, showing the phase transition between the exact dimer state (horizontal dashed line) and the antiferromagnetic state for different bond dimensions, for (a) $J'/J = 0.61$ and (b) $J'/J = 0.66$. The dashed-dotted line shows the energy extrapolated in inverse bond dimension.

4.4. Conclusions

We have introduced the LCTM method, which is an efficient approach to study layered 2D systems with a weak interlayer coupling. The main idea is to perform a decoupling of the 3D network using the FU truncation onto $D_z = 1$ away from the center of each plane, while keeping the full bond dimension $D_z > 1$ in the center, such that the resulting network can be efficiently contracted with the standard CTM method in each layer. Our benchmark results for the anisotropic Heisenberg model demonstrate that the method yields values in close agreement with a full 3D contraction (SU+CTM), at a substantially lower computational cost. The results are close to QMC results even for a small interlayer bond dimension $D_z = 2$. Although the accuracy decreases when J_z/J_{xy} is increased, errors remain relatively small up to $J_z/J_{xy} = 0.4$. Our results for the SSM demonstrate that LCTM also enables the accurate study of problems that are out of reach of QMC due to the negative sign problem.

There are several promising ways to further improve the LCTM method. First, the accuracy of the FU projection onto $D_z = 1$ could be improved by making use of disentanglers between the layers [102, 200]. Second, the accuracy of the contraction can be increased by including more $D_z > 1$ bonds in the center (see

App. 4.A.4), although at a higher computational cost. Instead of keeping k open legs with total bond dimension $(D_z)^k$ in between the layers, the total dimension could be effectively reduced by introducing appropriate projectors between the layers. Third, instead of a complete decoupling away from the center, a small vertical bond dimension χ_z could be kept in the CTM environment tensors in order to capture the most relevant interlayer entanglement away from the center. And finally, the contraction scheme may also be combined with an energy minimization based on automatic differentiation [124], which is expected to provide more accurate tensors than the FFU optimization used here.

We believe our approach provides a powerful and practical tool for future studies of challenging layered 2D systems, especially models that are out of reach of QMC. Finally, we note that the LCTM method can be straightforwardly extended to fermionic systems and finite temperature calculations, e.g., by adapting ideas from Refs. [116, 201–203] and Refs. [147, 148], respectively.

4.A. Appendix

In this appendix, additional details and results on the LCTM method and the iPEPS optimization are presented. In Sec. 4.A.1, the truncation used in the $D_z > 1 \to D_z = 1$ projection step and in the FFU optimization is discussed as well as two computationally cheaper truncation approaches. Details on the FFU optimization and a comparison between FFU and other imaginary time evolution algorithms are presented in Sec. 4.A.2. Section 4.A.3 discusses the decay of the singular value spectra of the iPEPS, which further justifies the use of an anisotropic ansatz. Additional results on the accuracy and convergence of the LCTM are provided in Sec. 4.A.4, including the dependence on the boundary bond dimension χ, a comparison with the HOTRG method, the number of interlayer $D_z > 1$ connections, and a comparison of different layer decoupling procedures.

4.A.1. Truncation

In this section, we provide additional details on the truncation method, which is used to perform the projection from $D_z > 1$ to $D_z = 1$ of the vertical bonds. In the LCTM this is done with a FU truncation [54, 114] that involves the minimization of the norm distance

$$d = \left\| |\tilde{\psi}\rangle - |\psi'\rangle \right\|^2 \tag{4.3}$$

where $|\tilde{\psi}\rangle$ and $|\psi'\rangle$ are the untruncated and truncated iPEPS, respectively. The FU truncation was discussed in detail in Sec. 2.5.1 in the context of imaginary time evolution. The FU requires the computation of the environment around the bond that is being truncated, which is obtained using the LCTM approach. The relevant diagrams for a horizontal and a vertical bond are shown in Figs. 4.7(e) and Figs. 4.7(f), respectively.

Besides the FU truncation, which takes the full wave function into account to truncate a bond, other schemes exist where the environment is approximated through a local contraction. One such scheme is the SU [115] which makes use of an environment consisting of only two tensors together with their adjacent singular values as was discussed in Sec. 2.5.1. An improvement over the SU truncation (but still less accurate than the FU) is provided by the CU truncation [113, 119–121], which takes a larger environment consisting of a finite number of tensors around the bond into account. Figures 4.7(c) and 4.7(d) show examples of a 4×3 cluster environment for intraplane update steps and a 3×3 environment for the interplane bond, respectively.

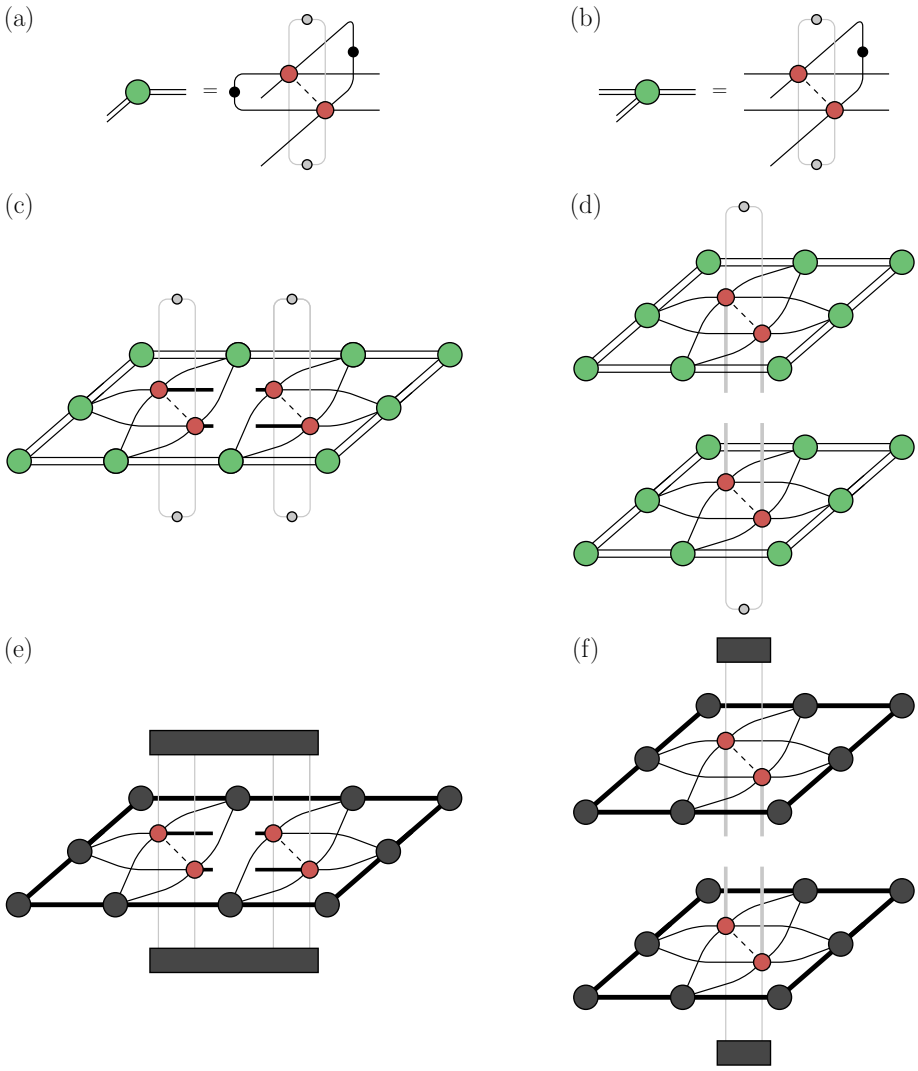

Figure 4.7: The environments used in our implementations of (a)-(d) the CU truncation and (e)-(f) the FFU truncation. (a)-(b) For graphical brevity, a compact notation is used. The small circles on the traced-out bonds represent the corresponding singular value matrices on the bonds. (c) A 4×3 cluster environment used for the intraplane update steps. (d) A 3×3 environment used in the interplane direction. (e) The FFU environment used for an intraplane bond. (f) The FFU environment for an interplane update step.

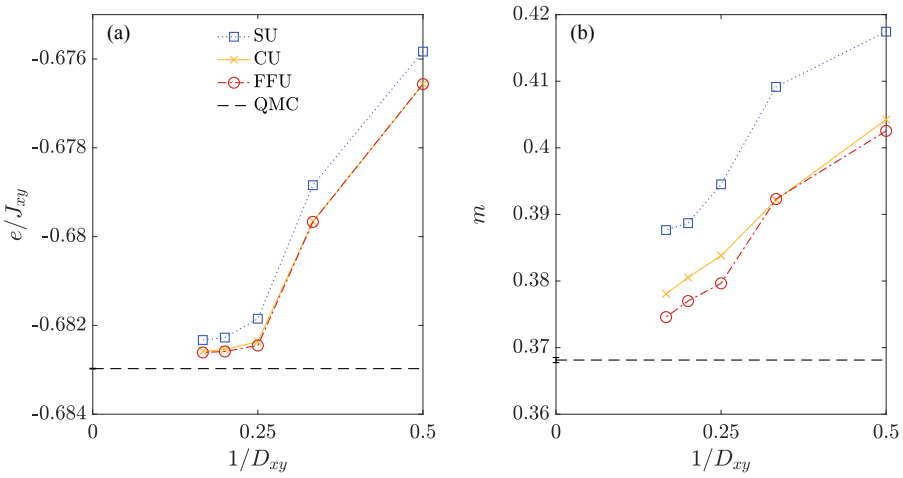

Figure 4.8: Comparison of results obtained with the SU, CU, and FFU imaginary time evolution methods for the anisotropic Heisenberg model with $J_z/J_{xy} = 0.1$ as a function of $1/D_{xy}$ and $D_z = 2$. For reference, extrapolated QMC results are provided. (a) Energy per site e in units of J_{xy}. (b) Local magnetic moment m.

4.A.2. Imaginary time evolution with LCTM

In the main text, results have been obtained based on the FFU approach. Alternatively, we have also tested imaginary time evolution schemes based on a SU and CU truncation, which are computationally cheaper but also less accurate. Here, we compare the results of these variants obtained for the anisotropic Heisenberg model with $J_z/J_{xy} = 0.1$ in Fig. 4.8. The SU leads to slightly higher energies than the FFU, as shown in Fig. 4.8(a), whereas the CU yields similar results to the FFU. For the local magnetic moment m, shown in Fig. 4.8(b), the deviation between the SU and FFU is more pronounced. Also here, the CU gives a significant improvement upon the SU result, with slightly larger values compared to the FFU result at large bond dimensions.

4.A.3. Decay of the singular value spectrum

To further motivate the anisotropic ansatz and contraction approach, we consider the singular value spectrum on the intra- and interplane bonds in Fig. 4.9 obtained for the 3D anisotropic Heisenberg model. The singular value matrices are extracted from our FFU-optimized tensors using the algorithm from

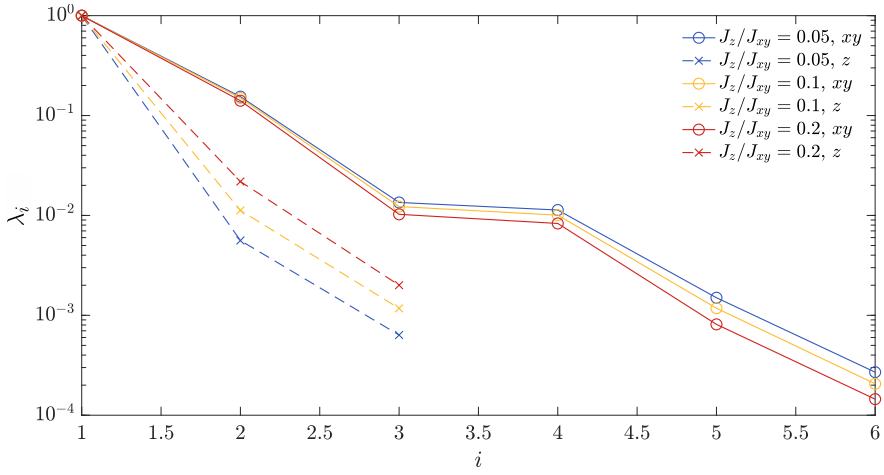

Figure 4.9: Spectrum of the singular values λ_i on the intra- and interplane bonds in the iPEPS ansatz obtained for the anisotropic Heisenberg model with $D_{xy} = 6$ and $D_z = 3$, exhibiting a fast decay (weaker entanglement) in the z-direction and a slow decay (stronger entanglement) in the xy-direction for small J_z/J_{xy}.

Ref. [82], which is similar to the procedure discussed in Sec. 2.2.1 to convert an iMPS to the canonical form but adapted to iPEPS to transform it into a quasi-canonical form.

A much faster decay of the singular values can be observed in the z-direction than in the intraplane direction, as expected, due to the weak entanglement between the planes. Increasing J_z/J_{xy} leads to a slower decay in the z-direction, suggesting that the value of D_z needs to be increased. Eventually, for sufficiently large J_z/J_{xy} the singular values in all directions will become of similar magnitude, such that an anisotropic ansatz in combination with the LCTM contraction is no longer justified.

4.A.4. Accuracy of the LCTM contraction

The accuracy of the LCTM contraction is controlled by both the boundary bond dimension χ of the CTM environment tensors as well as the number of untruncated interlayer connections that are kept in the center of the network. In this section, we analyze the dependence of the results on these parameters for the 3D anisotropic Heisenberg model. We also provide a comparison to the

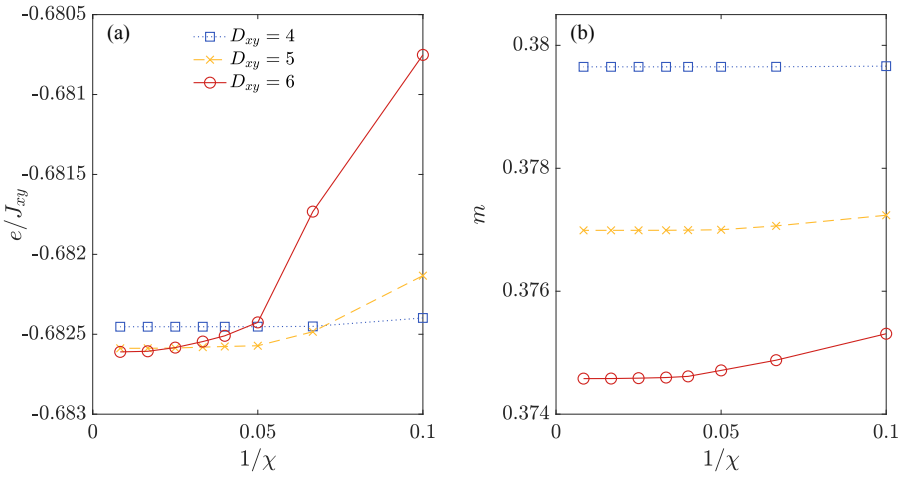

Figure 4.10: Convergence as a function of the inverse CTM boundary dimension $1/\chi$ for $D_{xy} = 4-6$ and $D_z = 2$. The results are for the anisotropic Heisenberg model with $J_z/J_{xy} = 0.1$. (a) The energy per site e in units of J_{xy}. (b) Local magnetic moment m.

HOTRG method [101, 107]. Finally, we examine alternative approaches for the $D_z > 1$ to $D_z = 1$ truncation performed away from the center.

Convergence in χ

In Fig. 4.10(a) we show the energy per site, e, for $J_z/J_{xy} = 0.1$ as a function of $1/\chi$ for different values of D_{xy} and $D_z = 2$. Convergence is reached at sufficiently large χ, where a higher χ is needed for larger D_{xy} for an accurate evaluation, as expected. Interestingly, we find that an increase in D_z does not require a larger χ to converge. Similar observations can be made for the local magnetic moment m in Fig. 4.10(b). For the results in the main text, χ is chosen sufficiently large such that finite-χ errors are negligible.

Comparison with HOTRG

In this section we present a comparison of the convergence behavior of the LCTM method as a function of χ with results obtained with the HOTRG approach [101,107], which was discussed in Sec. 2.4.2. Figure 4.10 shows the results for the energy and magnetization for different bond dimensions and $D_z = 2$, us-

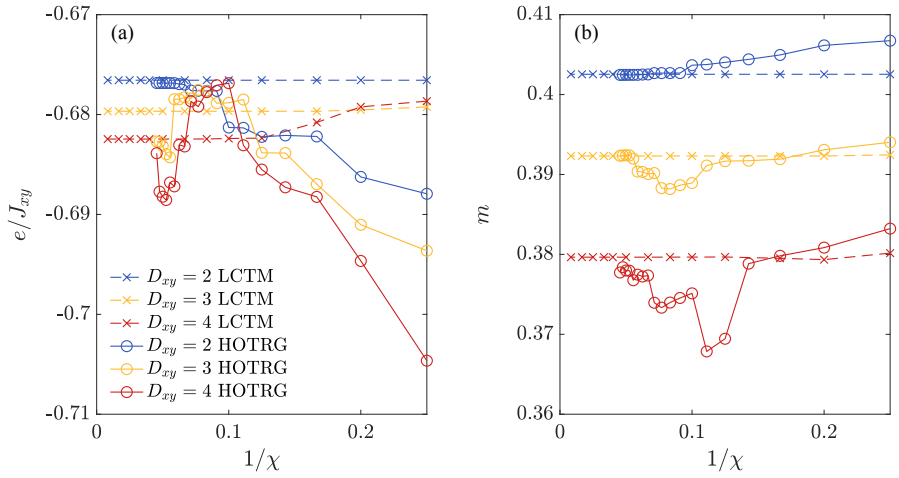

Figure 4.11: Comparison between LCTM and HOTRG for the convergence of the energy (a) and the magnetization (b) as a function of inverse bond dimension $1/\chi$.

ing tensors obtained from an FFU optimization (the same optimized tensors are used for the two contraction approaches). For small bond dimension $D_{xy} = 2$ the two approaches yield similar results at large χ. However, with increasing bond dimension it becomes more and more challenging to reach convergence with HOTRG, which overall displays an irregular convergence behavior as a function of χ and which is computationally substantially more expensive than LCTM. Similar observations have been made for the isotropic 3D Heisenberg model in Chap. 3, where it was found that SU+CTM shows a much more regular convergence behavior than HOTRG. For this reason, we have taken results from SU+CTM as reference values in the main text.

Interlayer connectivity

The number of untruncated $D_z > 1$ interlayer connections is another parameter controlling the accuracy of the LCTM method. The results in the main text have been obtained by just keeping a single connection in the center for one-site observables and interlayer two-site observables, and two connections for intralayer two-site observables. Here we present a comparison to a different scheme, in which we also keep the interlayer connections on the tensors neighboring the (two) central one(s). In practice, this can be implemented by absorbing tensors with $D_z > 1$ into the environment tensors at the final CTM

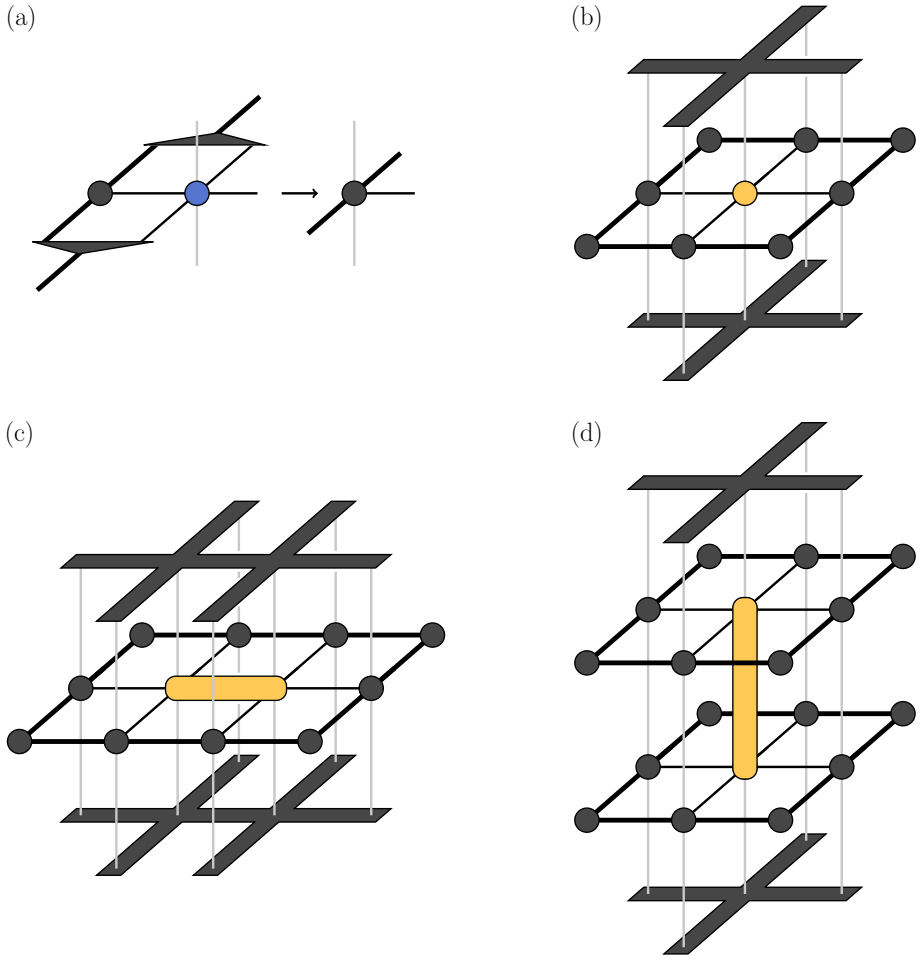

Figure 4.12: The star LCTM contraction, which differs from the standard LCTM because both the central and nearest-neighbor interlayer connections remain untruncated. The yellow tensors indicate the contraction of bra- and ket-tensors with an operator in between. (a) The star LCTM differs from the standard LCTM at the final CTM step where a tensor with untruncated interlayer connections is absorbed into the environment. (b) The final diagram for the computation of a one-site observable. The leading eigenvector is a larger object compared to the standard LCTM due to the additional untruncated bonds. (c) The diagram of an intraplane two-site observable. (d) The diagram of an interplane two-site observable.

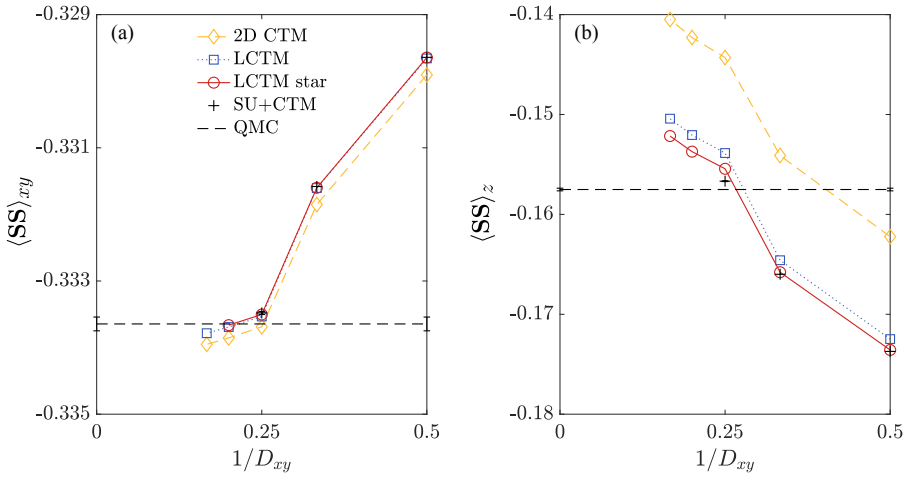

Figure 4.13: Contraction results for the nearest-neighbor spin-spin correlators obtained with a 2D CTM, standard LCTM, and star LCTM for the anisotropic Heisenberg model with $J_z/J_{xy} = 0.1$ as a function of $1/D_{xy}$ and with $D_z = 2$. For comparison, results obtained from a full 3D contraction (SU+CTM) and extrapolated QMC results are provided. (a) Nearest-neighbor spin-spin correlator in the intraplane direction $\langle \mathbf{SS} \rangle_{xy}$. (b) Nearest-neighbor spin-spin correlator in the interplane direction $\langle \mathbf{SS} \rangle_{z}$.

step, as depicted in Fig. 4.12(a). Figures 4.12(b)-(d) show the diagrams to evaluate a one-site observable, an intraplane two-site observable, and an interplane two-site observable, respectively. We call this scheme the star LCTM. It has the advantage that more of the interlayer correlations are taken into account, however, at the expense of a significantly higher contraction cost.

In Fig. 4.13(a) results for the nearest-neighbor spin-spin correlator in the intraplane direction are shown, using different contraction schemes to evaluate them. The tensors have been obtained for $J_z/J_{xy} = 0.1$ using the FFU imaginary time evolution based on the standard LCTM scheme. Besides the standard and star LCTM approach, we also include data from the 2D CTM in which no interlayer connections are kept (i.e., also the connection(s) on the central tensor(s) is (are) truncated to $D_z = 1$), and from the full 3D contraction (SU+CTM) which we take as reference values. We observe that without the interlayer connections (2D CTM) the deviation from the SU+CTM result is relatively large, whereas both the standard and star LCTM show a close agreement with the full 3D contraction.

Figure 4.13(b) shows results in the interlayer direction. The deviation from the

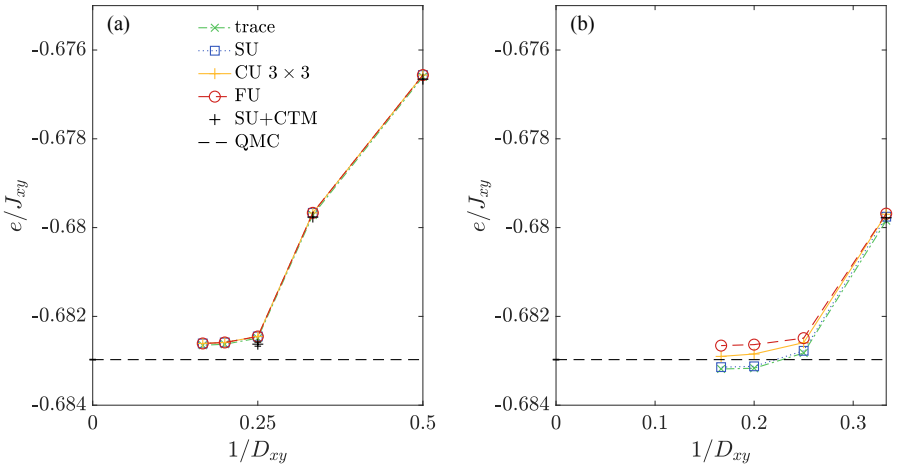

Figure 4.14: Results obtained with alternative layer decoupling approaches based on tracing out the z-bond, a SU truncation, and a CU truncation using a 3×3 cluster size compared to a FU truncation. The energy per site is shown as a function of $1/D_{xy}$ for the anisotropic Heisenberg model with $J_z/J_{xy} = 0.1$. For reference, a SU+CTM contraction and an extrapolated QMC result are provided as well. (a) $D_z = 2$. (b) $D_z = 3$.

SU+CTM result is larger here with the standard LCTM scheme, although it performs much better than the 2D CTM. A significant improvement is obtained by using the star LCTM, with a close agreement to SU+CTM for $D_{xy} = 2$ and 3. For larger D_{xy} we expect that the results can be further improved by keeping even more interlayer connections.

As already pointed out in the main text, increasing the two bond dimensions D_{xy} and D_z has an opposite effect on the change in the $\langle \mathbf{SS} \rangle_z$ correlator, which can be intuitively understood as follows. Firstly, an increase in D_z at fixed D_{xy} naturally leads to a decrease in $\langle \mathbf{SS} \rangle_z$, because the higher bond dimension lowers the variational energy on these bonds. The increase in $\langle \mathbf{SS} \rangle_z$ with increasing D_{xy} is less obvious, but can be best understood in the $D_z = 1$ limit. In this limit, the $\langle \mathbf{SS} \rangle_z$ correlator (or equivalently the energy on a z-bond) is minimized by the classical antiferromagnetic state which is realized for $D_{xy} = 1$, and amounts to $-m^2$, with $m = 1/2$ the magnitude of the local magnetic moment on each site. By increasing D_{xy}, m will become smaller due to intraplane quantum fluctuations (entanglement), and hence the $\langle \mathbf{SS} \rangle_z$ correlator between the layers with $D_z = 1$ will increase. We note that the opposite effect is observed for $\langle \mathbf{SS} \rangle_{xy}$, just that the dependence on D_z is very weak.

Alternative layer decoupling approaches

A key step in the LCTM method is the decoupling of the layers away from the center, which for the results in the main text is done by a FU truncation to $D_z = 1$. In this section, we compare several alternative local truncation approaches to the FU results.

The first alternative we consider is to trace out the bonds in the z-direction by connecting the respective bonds of the iPEPS tensors in the bra- and in the ket-layers. On these bonds, we include the corresponding singular value matrices in the same spirit as done in the SU and CU truncation. Another option we test is the SU truncation. Finally, we consider a CU truncation based on the 3×3 environment shown in Fig. 4.7(d).

Figure 4.14(a) shows results for the energy per site, e, as a function of $1/D_{xy}$ and $D_z = 2$ at $J_z/J_{xy} = 0.1$. Here we find that the alternative truncation approaches show a good agreement with the FU layer decoupling scheme. For the $D_z = 3$ case, presented in Fig. 4.14(b), however, the scheme based on tracing out the interlayer connections and the SU truncation both give a significant underestimation of the energy compared to FU. Although the CU 3×3 truncation performs better, it yields values that are too small as well. These results indicate that performing an accurate truncation is important, at least for $D_z > 2$, and they motivate the use of the computationally more expensive FU truncation in the main text.

CHAPTER 5

The Shastry-Sutherland model with weak interlayer coupling

The layered material $SrCu_2(BO_3)_2$ has long been studied because of its fascinating physics in a magnetic field and under pressure. Many of its properties are remarkably well described by the SSM. However, the extent of the intermediate plaquette phase discovered in $SrCu_2(BO_3)_2$ under pressure is significantly smaller than predicted in theory, which is likely due to the weak interlayer coupling that is present in the material but neglected in the model. Using state-of-the-art tensor network methods, we study the SSM with a weak interlayer coupling and show that the intermediate plaquette phase is destabilized already at a smaller value around $J''/J \sim 0.04 - 0.05$ than previously predicted from series expansion (SE). Based on our phase diagram we estimate the effective interlayer coupling in $SrCu_2(BO_3)_2$ to be around $J''/J \sim 0.027$ at ambient pressure.

The contents of this chapter are based on Ref. [204] (submitted to SciPost Physics)

5.1. Introduction

The competing interactions in frustrated materials give rise to a rich variety of fascinating phenomena. A paradigmatic example is the layered material $SrCu_2(BO_3)_2$ which has attracted significant attention in the past decades, in particular since the discovery of its intriguing sequence of magnetization plateaus at 1/8, 2/15, 1/6, 1/4, 1/3, and 1/2 (and possibly 2/5) [192, 205–214]. Substantial efforts have been invested in understanding the magnetic structures of the plateaus, with a growing consensus that they correspond to crystals of triplets at high magnetic field [59, 193, 215–219] and crystals of bound states of triplets at low field [31, 220]. Another exciting direction has been the study of the phase diagram under pressure [63, 153, 213, 221–227], which has revealed two phase transitions at zero field, including a critical point at finite temperature [153], and an even richer phase diagram at finite field [226].

Many properties of $SrCu_2(BO_3)_2$ are remarkably well described by the Shastry-Sutherland model (SSM) [192, 193, 198], a frustrated $S = 1/2$ spin model of orthogonal dimers on a square lattice, shown in Fig. 5.1(a). Its Hamiltonian is defined as

$$H_{2D} = J \sum_{\langle ij \rangle} \mathbf{S}_i \mathbf{S}_j + J' \sum_{\langle ij \rangle'} \mathbf{S}_i \mathbf{S}_j, \tag{5.1}$$

with J and J' the intra- and interdimer coupling, respectively. For small values of J'/J, the ground state is exactly given by a product of dimer singlets. In the other limit, the model reduces to the square lattice Heisenberg model with an antiferromagnetic (Néel) ground state. For intermediate J'/J consensus has been reached on the existence of an empty plaquette (EP) state [69, 228–230] in the range $0.675(2) < J'/J < 0.765(15)$ [69], in which strong bonds are formed around half the empty plaquettes which do not contain a dimer. While a weak first-order phase transition between the EP and Néel phase was found in Ref. [69], more recently there have also been predictions of a deconfined quantum critical point [231] (see also related Ref. [227]) or a narrow quantum spin liquid region between the two phases [232, 233].

At ambient pressure the effective coupling ratio in $SrCu_2(BO_3)_2$ is around $J'/J = 0.63$ [212], which lies in the dimer phase but close to the plaquette phase. Applying hydrostatic pressure causes the Cu-O-Cu angle to diminish, which results in a rapid decrease of J and a slower decrease in J' [234, 235], such that the ratio J'/J increases. Evidence of a phase transition into an intermediate gapped phase around 1.8 GPa has been found in various experiments, including NMR [221], X-ray scattering [222], inelastic neutron scattering (INS) [223], electron spin resonance (ESR) [224], magnetization measurements [213, 226], and specific heat measurements [63,153]. The nature of the intermediate phase is still

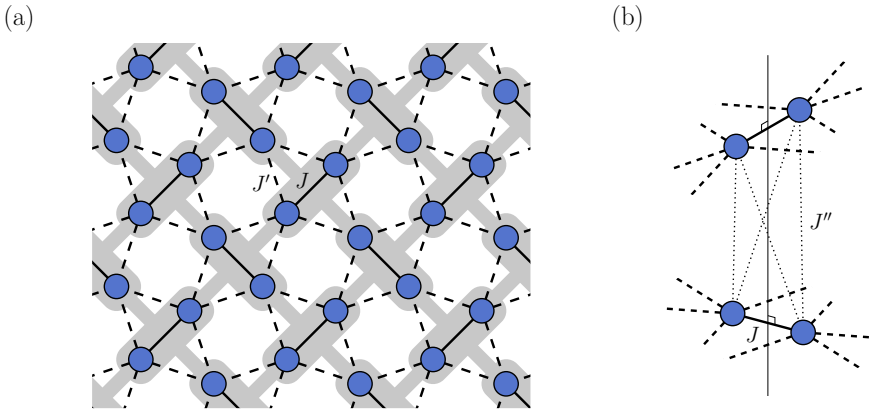

Figure 5.1: (a) The Shastry-Sutherland lattice with J the intradimer and J' the interdimer coupling. In gray, the underlying square lattice of orthogonal dimers is shown. (b) Two dimers in adjacent layers interact via the interlayer coupling J'' as indicated by the dotted lines. Each site of a dimer is coupled to both sites of the orthogonal dimer in the neighboring layer.

not fully settled. There exist indications from NMR [221,227] and INS [223] that the intermediate phase is not the EP phase but a closely related full plaquette (FP) phase, in which strong bonds are formed around the plaquettes containing a dimer. In the SSM this state is slightly higher in energy than the EP state, but it can be stabilized in a weakly distorted SSM [236] (however, the strength of the relevant couplings is not known). Antiferromagnetic order was observed with INS below 117 K and above 4 GPa [223], close to a tetragonal-monoclinic transition beyond which the SSM is no longer valid. Based on specific heat measurements [63], another Néel phase with a substantially lower transition temperature was discovered below 4 GPa, and the transition to the plaquette phase was found to occur around 2.5-3 GPa. Converted to J'/J [226] this corresponds to $J'/J \sim 0.7 - 0.71$, which is significantly lower than the theoretical prediction based on the SSM.

A natural cause of this discrepancy is the presence of small interlayer couplings in the compound [63, 70], which are neglected in the 2D model. The dominant interaction can be described by an additional Heisenberg term with strength J'' between the layers [59, 70, 237], such that the 3D model reads

$$H_{3\mathrm{D}} = H_{2\mathrm{D}} + J'' \sum_{\langle ij \rangle''} \mathbf{S}_i \mathbf{S}_j. \tag{5.2}$$

The $CuBO_3$ layers are stacked in such a way that the dimers have an alternating orientation in neighboring layers [59] and each site of a dimer interacts with

both sites of the neighboring dimer, see Fig. 5.1(b).[1] This model has already been studied in Ref. [70] using SE, where it was found, based on a fourth-order expansion, that the extent of the plaquette phase shrinks rapidly with increasing J'', and that it disappears beyond $J''/J \sim 0.08$. However, results at higher orders or from other numerical approaches have so far been lacking.

Regarding the strength of the interlayer coupling in $SrCu_2(BO_3)_2$, there is still no consensus. In Ref. [238] an estimate of $J''/J = 0.09$ was obtained from fits to the magnetic susceptibility. In Ref. [239], based on an analysis of the bound state energies of the two-triplet excitations, a much larger value $J''/J = 0.21$ was found. Calculations from density-functional theory (DFT) [234] predicted a much smaller ratio, $J''/J \leq 0.025$, but with values for J and J' which deviate considerably from other predictions.

In this chapter, we refine the phase diagram of the SSM with weak interlayer coupling using state-of-the-art tensor network methods for layered systems, the LCTM algorithm which was introduced in Chap. 4. We show that the EP phase becomes unstable at even smaller values of J''/J than predicted by SE. From our phase diagram, we extract an estimate of J''/J in $SrCu_2(BO_3)_2$, by determining the value which leads to an extent of the plaquette phase that is consistent with experiments. Besides this, we also analyze the effect of the interlayer coupling on the competition between the EP phase and the FP phase and show that the latter remains higher in energy also for finite J''/J.

The chapter is organized as follows. In Sec. 5.2 details on the simulation are discussed. In Sec. 5.3 we first provide an overview of the phase diagram, followed by a detailed study of the phase transitions along selected cuts. We then present additional results on the competition between EP and FP states and the phase diagram and we end the results section with a discussion on the estimate of the effective interlayer coupling in $SrCu_2(BO_3)$. Finally, in Sec. 5.4 we present our conclusions.

5.2. Simulation details

The simulations in the present study are performed using iPEPS. We consider a cubic lattice with one tensor per dimer [69], see Fig. 5.1(a). This results in a supercell consisting of two tensors which are repeated on the two sublattices. Motivated by the anisotropic nature of the model we take an ansatz

[1] We note that the model neglects the buckling of the $CuBO_3$ layers which causes a small difference in the distance between the Cu^{2+}-ions in adjacent layers [59], and hence slightly different J'' couplings. However, since the effect is expected to be small, we consider the same coupling on all bonds for simplicity, as previously done in Ref. [70].

with different bond dimensions in the intra- and interplane directions, D_{xy} and D_z, respectively, with $D_{xy} \geq D_z$. To contract the ansatz, we make use of the LCTM contraction algorithm introduced in Chap. 4. To obtain accurate interlayer projectors within the LCTM we iterate the environment computation up to three times. To improve the computational efficiency, we use tensors with implemented $U(1)$ symmetry [125, 126].

The ansatz is optimized using a combination of energy minimization and FFU. Initially, the tensors are optimized on the 2D lattice (i.e., with $J''/J = 0$) by energy minimization. The resulting tensors are then used as initial states in an FFU optimization with finite J''/J, which we found leads to better results than optimizations initialized from a SU [115] optimization at the values of J'/J and J''/J considered. Simulations in the Néel phase are initialized at $J'/J = 0.8$ and evolved using imaginary time steps $\tau = 0.1$ and $\tau = 0.05$, where the state with the lowest energy is selected. For the simulations of the EP phase, a 2D iPEPS at the corresponding J'/J is used as the initial state and the FFU is performed with $\tau = 0.05$. In some cases, an increase in the energy is observed after a certain imaginary time β. In these cases, the simulation is halted and the tensors giving the lowest energy are selected. We note that the EP states can be stacked in two different ways. While our main results have been obtained with plaquettes in alternating positions in adjacent layers, we have also tested the stacking with plaquettes on top of each other [231], which we found leads to similar results.

To identify the phases, we introduce the following order parameters. For the Néel phase, we consider the local magnetic moment

$$m = \sqrt{\langle \mathbf{S}_x \rangle^2 + \langle \mathbf{S}_y \rangle^2 + \langle \mathbf{S}_z \rangle^2}, \tag{5.3}$$

with $\mathbf{S}_i$ the spin operators. As an order parameter for the EP phase, we use

$$\Delta e_{\mathrm{EP}} = \bar{e}_{\mathrm{other}} - \bar{e}_{\mathrm{EP}}, \tag{5.4}$$

where $\bar{e}_{\mathrm{EP}}$ is the mean energy of the bonds belonging to the empty plaquette and $\bar{e}_{\mathrm{other}}$ is the mean energy of the remaining bonds.

5.3. Simulation results

The main results of this work are summarized in the phase diagram in Fig. 5.2. For the range of couplings considered, the 3D model exhibits the same three phases as the 2D model: a dimer phase made of exact singlets in the low J'/J region, an empty plaquette (EP) phase at intermediate values of J'/J,

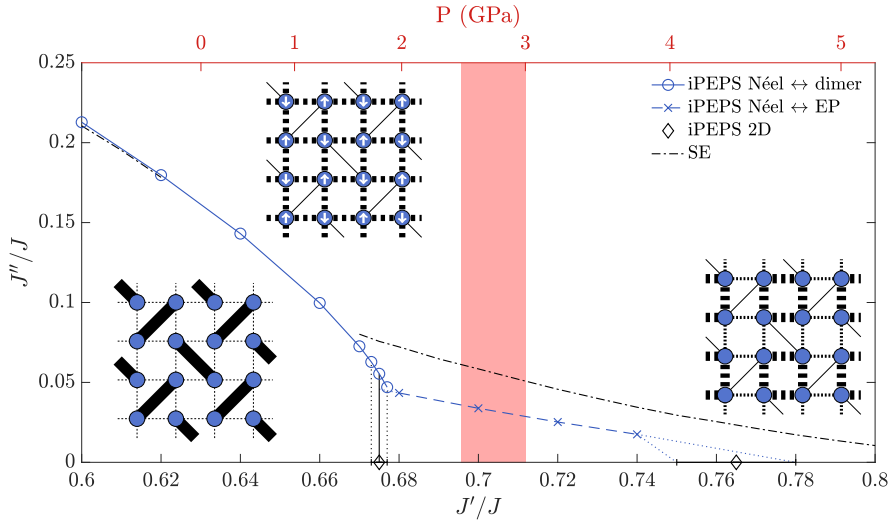

Figure 5.2: The phase diagram of the SSM with interlayer coupling ($D_{xy} = 6$, $D_z = 3$), which includes a dimer, a Néel, and an empty-plaquette (EP) phase. Previous iPEPS results for the 2D model [69] are shown by the black diamonds, and the dashed-dotted lines correspond to fourth-order SE data [70]. The upper horizontal axis shows the pressure corresponding to a particular coupling J'/J, based on the pressure model from Ref. [226]. The location of the plaquette to Néel phase transition found in experiments [63] is marked in light red.

and a Néel phase which dominates for sufficiently large J'/J and/or large J''/J. The EP phase destabilizes already at weak interlayer coupling of at most $J''/J \sim 0.04 - 0.05$ in favor of the Néel phase, while the dimer phase survives at stronger interlayer coupling. That the Néel state gets energetically favored for sufficiently large J''/J can be intuitively understood from the fact that the antiferromagnetic layers can be stacked on top of each other without frustrating the Néel order [70], and hence the additional interlayer coupling lowers the energy per site. This is in contrast to the interlayer energy of the 2D dimer, which is exactly zero, or close to zero in case of the EP state.

Our results are in good agreement with the SE results from Ref. [70] for the dimer singlet to Néel phase transition, however, the transition from the EP to Néel phase is located at weaker interlayer coupling than predicted by SE shown by the dashed-dotted line in Fig. 5.2.

In the following, we provide a detailed study of the phase transitions along specific cuts for fixed J'/J and varying J''/J.

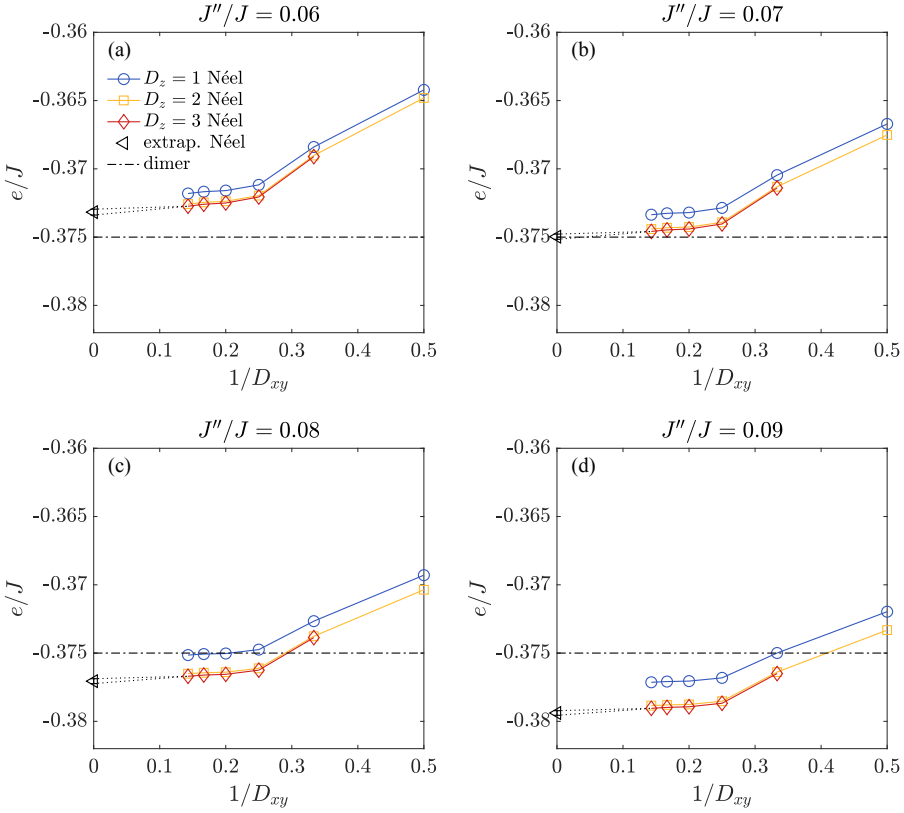

Figure 5.3: Energy per site e in units of J at $J'/J = 0.67$ for different values of J''/J around the phase transition between the dimer and Néel states. The latter is plotted as a function of $1/D_{xy}$ for $D_z = 1-3$ and it includes an extrapolation to the infinite bond dimension limit (see text for details). The exact energy of the dimer state is shown by the dashed-dotted line.

5.3.1. Phase transition between dimer and Néel phase

In this section we consider the phase transition between the dimer singlet and the Néel phase, focusing on a cut at $J'/J = 0.67$. This transition has been studied in Chap. 4 with the LCTM method for $J'/J = 0.61$ and $J'/J = 0.66$ as a benchmark example.

Figure 5.3 shows the energy per site e as a function of inverse bond dimension $1/D_{xy}$ and different values of D_z at $J''/J = 0.06$, 0.07, 0.08, and 0.09, respectively. The dimer state has an exact energy of $e = -3/8J$ per site, i.e., it is

independent of J'/J and J''/J, and it is already reproduced for $D_{xy} = D_z = 1$. The energy of the Néel state exhibits a stronger dependence on D_{xy} than on D_z, which is due to the weak interlayer coupling compared to the intraplane coupling. While the energy gets considerably lowered from $D_z = 1$ to $D_z = 2$, it hardly changes anymore when increasing it to $D_z = 3$. In contrast, substantially larger changes are obtained by varying D_{xy}, which motivates using an anisotropic ansatz with $D_{xy} > D_z$.

To obtain an estimate of the energy in the infinite bond dimension limit, we perform an extrapolation in $1/\kappa$, with $D_{xy} = \kappa$ and $D_z = \frac{\kappa-1}{2}$, i.e., using the energy of the states for ($D_{xy} = 5$, $D_z = 2$), ($D_{xy} = 7$, $D_z = 3$), and the mean of ($D_{xy} = 6$, $D_z = 2$) and ($D_{xy} = 6$, $D_z = 3$). Since the convergence in the bond dimension is typically faster than linear, we take the mean between the linearly extrapolated result and the lowest energy result at ($D_{xy} = 7$, $D_z = 3$) to be the estimate. As an error estimate, we take half the difference between the estimate and the lowest energy value at finite bond dimension.[2]

The location of the phase transition is obtained from the intersection of the energies of the two states as a function of J''/J, shown in Figure 5.4(a).[3] Since the energy of the dimer state is fixed, each finite bond dimension result for the critical coupling $(J''/J)_c$ corresponds to an upper bound. The largest bond dimension ($D_{xy} = 7$, $D_z = 3$) yields $(J''/J)_c = 0.072$, whereas a slightly lower value is obtained based on the extrapolated energy, $(J''/J)_c = 0.0702(10)$.

In Fig. 5.4(b) the local magnetic moment m of the lowest energy state at fixed D is shown, revealing a large jump at the phase transition. Increasing D_{xy} has only a small effect on m near the phase transition which indicates that the jump remains finite in the infinite D limit, corresponding to a first-order phase transition.

5.3.2. Phase transition between empty plaquette and Néel phase

We next consider the transition between the EP phase and the Néel phase, focusing on a cut at $J'/J = 0.7$. In Fig. 5.5 the energy of the states as a function of $1/D_{xy}$ is presented for $J''/J = 0.02$, 0.03, 0.04, and 0.05 respectively, includ-

[2] We note that a more accurate energy extrapolation in the gapless Néel phase could be obtained using finite correlation length scaling [131, 132]. However, this requires an accurate estimate of the correlation length which with the current version of the LCTM approach cannot be obtained in a controlled way (since the approach is tailored to the computation of local observables).

[3] We note that, due to hysteresis effects, a state initialized in the Néel phase remains a Néel state even slightly beyond the transition into the dimer phase.

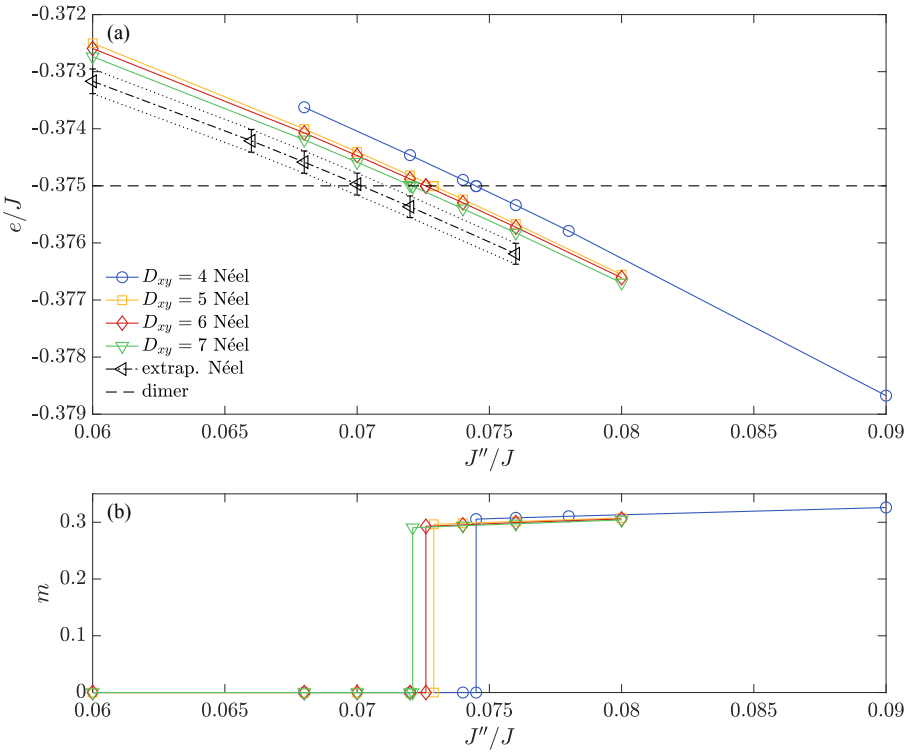

Figure 5.4: Results for the dimer to Néel phase transition for fixed $J'/J = 0.67$. (a) Energies of the dimer and Néel states as a function of J''/J ($D_z = 3$), where the phase transition is located at the intersection of the energies. (b) Local magnetic moment m across the phase transition, revealing that the transition is of first order.

ing an extrapolation performed in a similar way as described in the previous section.

The dependence of the Néel state energy on D_z is weaker than in the case of $J'/J = 0.67$ in the previous section, due to the smaller interlayer couplings that are considered here. An even weaker dependence on D_z is found for the EP state, which is expected due to the inherent 2D nature of the state. Since the local magnetic moment in the EP state vanishes, the interlayer energy is exactly zero at lowest order for $D_z = 1$, corresponding to a product state of 2D iPEPS. Going beyond $D_z = 1$ introduces correlations between the planes, which however remain very weak compared to the strong intraplane plaquette correlations, and hence the interlayer energy remains close to zero.

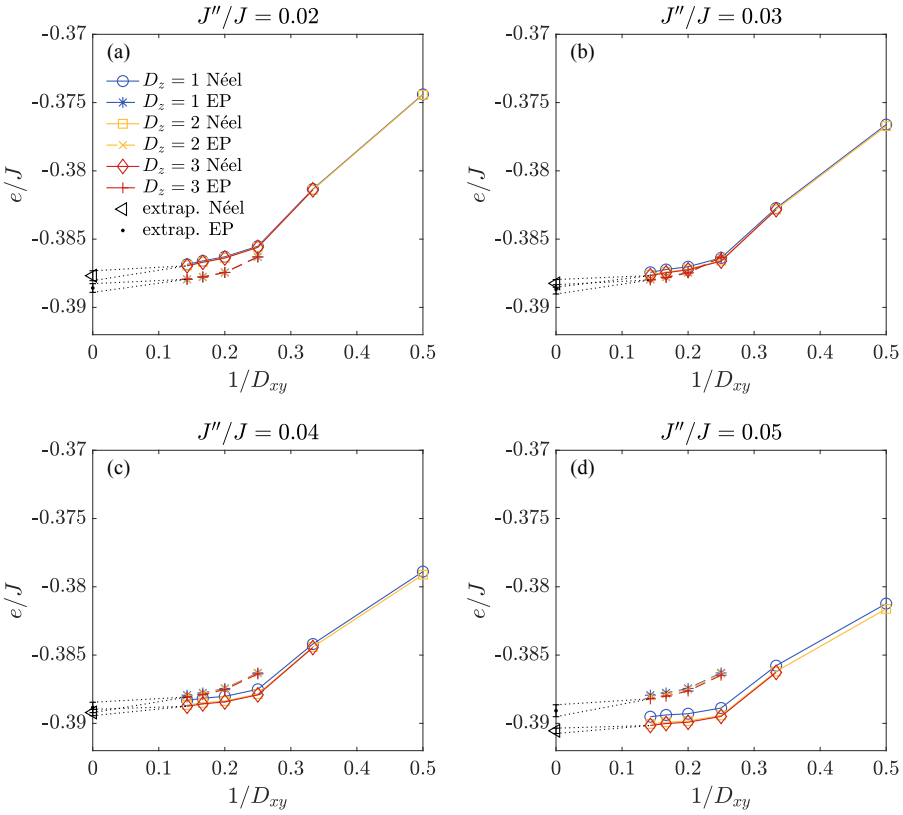

Figure 5.5: Energy per site as a function of $1/D_{xy}$ for $D_z = 1-3$ at $J'/J = 0.7$ for different values of J''/J around the phase transition between the EP and Néel states, including extrapolated energies.

Figure 5.6(a) shows the energy of the states as a function of J''/J in the vicinity of the phase transition. When D_{xy} is increased from 4 to 6 the EP state decreases slightly faster in energy than the Néel state, causing the location of the phase transition to shift to slightly higher J''/J. When increasing D_{xy} further only a tiny shift to a smaller coupling $(J''/J)_c = 0.034$ is found, suggesting that the location of the critical point does not change significantly anymore. Based on the extrapolated energies we get a critical coupling of $(J''/J)_c = 0.036$. By intersecting the upper and lower bounds of the error bars of the extrapolated energies we obtain an error range on the transition between $0.026 - 0.042$, which should provide a rather conservative error estimate. A less conservative error range is obtained by intersecting half the error bar widths, yielding

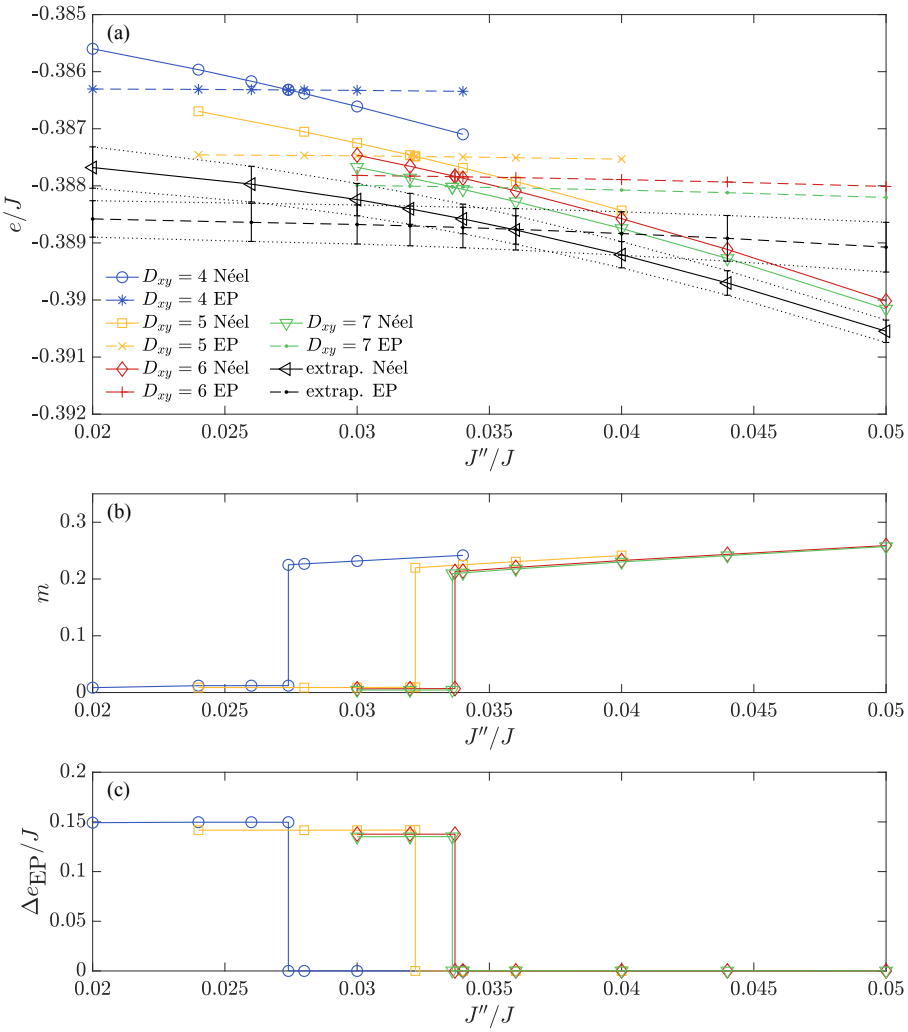

Figure 5.6: Results for the EP to Néel phase transition for fixed $J'/J = 0.7$. (a) Energies of the EP and Néel states as a function of J''/J ($D_z = 3$), where the critical coupling is located at the intersection of the energies. Both the local magnetic moment (b) and the EP order parameter (c) exhibit a jump at the phase transition, indicating that it is of first order.

$0.032 - 0.039$. Our value for the critical coupling is significantly lower than the SE result $(J''/J)_c = 0.058$ from Ref. [70].

In Figs. 5.6(b) and (c) the values of the local magnetic moment and EP order parameter across the phase transition are presented. Also in this case a discontinuous jump in the order parameters is found, indicating that the transition is of first order.

5.3.3. Competition between the empty and full plaquette states

As mentioned in the introduction, the precise nature of the intermediate phase in $SrCu_2(BO_3)_2$ is still not fully confirmed. NMR [221, 227] and INS [223] experiments suggest that the intermediate phase in $SrCu_2(BO_3)_2$ is not the EP but a full plaquette (FP) phase, in which strong bonds are formed around the plaquettes containing a dimer, as opposed to the EP state. In the SSM it was shown that the FP state is higher in energy than the EP state [236], but it can be stabilized by a relatively small deformation of the model using two types of intra- and interdimer couplings [236, 240]. In the following, we study the effect of the interlayer coupling on the competition between the EP and FP states at $J'/J = 0.7$, in order to test whether the FP state gets potentially stabilized in the 3D model.

In Figs. 5.7(a) and (b) we present the energies of the EP and FP states as a function of J''/J, respectively. The simulations for the FP state have been initialized in the 2D FP phase [236] by using two distinct dimer couplings on the two orthogonal dimers, $J_2/J_1 = 0.85$, and $J'/J_1 = 0.7$.[4] The dependence of the energy on J''/J is found to be very weak for both states such that the FP state remains higher in energy than the EP state as in the $J''/J = 0$ case. For comparison, we have also added the energy of the purely 2D states by the dashed lines which lie close to the energy obtained from the FFU optimization with finite J'', showing that the gain in interlayer energy is small in both cases. Thus, from these results, we conclude that the interlayer coupling does not stabilize the FP state.

For completeness, we also present the corresponding local magnetic moment and EP and FP order parameters in Figs. 5.7(c)-(f), where the latter is defined in a similar way as the EP order parameter (i.e., $\Delta e_{\mathrm{FP}} = \bar{e}_{\mathrm{other}} - \bar{e}_{\mathrm{FP}}$). In both states, the magnetization remains vanishingly small, and the strength of the corresponding plaquette orders does not change significantly with increasing J'/J.

[4] Due to stability issues for $D_{xy} = 6$ with $\tau = 0.05$ we have used a smaller value of $\tau = 0.01$ for $D_{xy} = 6$ which, however, does not have a significant effect on the energy.

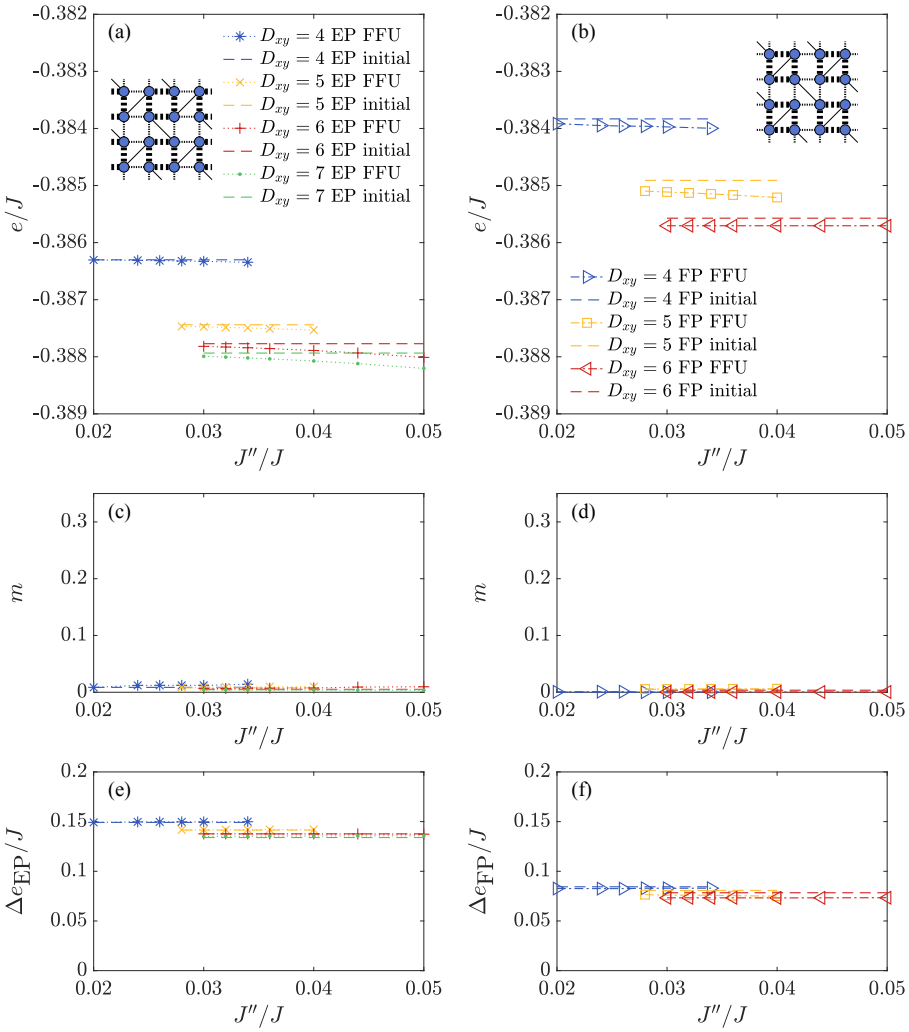

Figure 5.7: Comparison of results obtained for the EP (left column) and FP (right column) states for $J'/J = 0.7$ as a function of J''/J. (a)-(b) Energy per site of the two states for different values of D_{xy} with $D_z = 3$. The dashed lines indicate the energies of the initial 2D states for $J''/J = 0$. (c)-(d) show the corresponding local magnetic moments, and (e)-(f) the EP and FP order parameters, respectively.

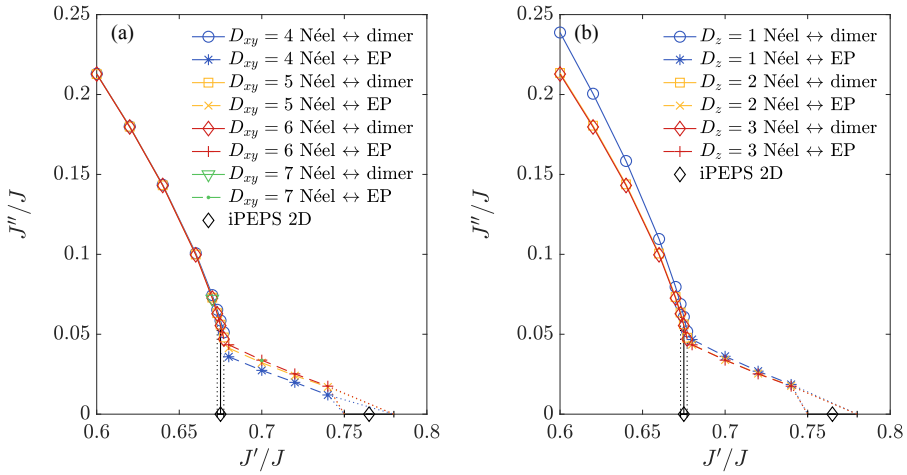

Figure 5.8: The phase diagram for (a) $D_{xy} = 4 - 7$ and fixed $D_z = 3$, and (b) fixed $D_{xy} = 6$ and $D_z = 1 - 3$. The phase transitions for the 2D model from Ref. [69] are shown by the black diamonds.

5.3.4. Phase diagram for different bond dimensions

To get more insights into the finite bond dimension effects on the phase diagram, we present results for different D_{xy} and D_z in Figs. 5.8(a)-(b), respectively. Overall, on the scale of the phase diagram, the changes on the phase transition lines are hardly visible at large bond dimensions. As discussed in Sec. 5.3.1, the transition line between the dimer and Néel phase shifts to slightly lower values with increasing D_{xy} and D_z since the energy of the exact dimer state is fixed, whereas the Néel state energy gets lowered with increasing bond dimension. The EP to Néel transition line is initially shifted to larger values of J''/J with increasing D_{xy}, but for $D_{xy} = 7$ essentially the same (slightly lower) value is found as for $D_{xy} = 6$. Increasing D_z has the opposite effect, because the gain in energy for the Néel state is considerably higher than for the EP state, as we have seen in Sec. 5.3.2, but the change from $D_z = 2$ to $D_z = 3$ is very small. We note that since the EP state energy is only very weakly dependent on J''/J and the dimer energy is constant, we have approximated the dimer to EP phase transition by a vertical line with the corresponding error bar from the 2D result [69].

5.3.5. The effective interlayer coupling in $SrCu_2(BO_3)_2$

Based on our phase diagram we can now discuss how large the effective value of J''/J in $SrCu_2(BO_3)_2$ should be, such that the extent of the plaquette phase is compatible with experiments. It is clear that it cannot be beyond $J''/J \sim 0.05$, because at these values the plaquette phase vanishes entirely. To relate the pressure to the coupling ratio J'/J we use the pressure model from Ref. [226], with the pressure dependence of the coupling parameters given by $J(p) = -5.13\,[\mathrm{K/GPa}]\,p + 81.5\,[\mathrm{K}]$ and $J'(p) = -1.43\,[\mathrm{K/GPa}]\,p + 51.35\,[\mathrm{K}]$. Based on specific heat measurements in Ref. [63] the phase transition between the plaquette and the Néel phase was found to occur around 2.5-3 GPa, corresponding to $J'/J = 0.704(8)$ and indicated by the light-red area in Fig. 5.2. At this coupling ratio the critical interlayer coupling in our phase diagram for ($D_{xy} = 6$, $D_z = 3$) is $J''/J = 0.032(4)$. Assuming that the pressure dependence of J'' is negligible compared to the pressure dependence of J, we find the effective interlayer coupling at ambient pressure to be around $J'' = 2.2(3)\,\mathrm{K}$ or $J''/J = 0.027(4)$.

This value is compatible with DFT calculations [234] predicting $J''/J \lesssim 0.025$. However, it is substantially smaller than the estimates from fits to the magnetic susceptibility ($J''/J = 0.09$) [238] based on exact diagonalization of a 16-site system, which may be due to finite size effects, limitations of the mean-field ansatz which was used to include the interlayer effects, or the chosen temperature range which excluded the data below 100 K. We note that the LCTM approach can also be extended to finite temperature, offering the possibility to perform accurate fits to the magnetic susceptibility as done for the 2D model in Ref. [150], which is an interesting direction for future research. An even larger value was obtained in Ref. [239], $J''/J = 0.21$, based on an analysis of the bound state energies of the two-triplet excitations, however, the relevant coupling ratio was predicted to be $J'/J = 0.603$ and the phase transition was found at $J'/J = 0.63$ which is too low compared to more recent estimates. Finally, one may wonder how this estimate would change in a slightly deformed Shastry-Sutherland model in which the FP state is slightly lower in energy than the EP state [236]. Since the change in energy of the AF state between $J''/J = 0$ and $J''/J = 0.1$ is roughly an order of magnitude larger than the typical energy difference between the EP and FP states, we can expect that the energies of the AF state and FP state intersect at a critical value $(J''/J)_c$ which is only slightly shifted compared to the standard SSM, yielding an estimate for the interlayer coupling that is not substantially different from the one we obtain for the standard SSM. A quantitative analysis would require simulations of the deformed model; however, the values of the effective couplings are not known.

5.4. Conclusion

In this chapter, we have performed a systematic study of the phase diagram of the SSM with weak interlayer coupling using 3D iPEPS with the LCTM approach. Our results are in qualitative agreement with fourth-order SE results, however, on the quantitative level we found that the transition between the EP and the Néel phase occurs at a lower J''/J than predicted by SE, with critical couplings of at most $J''/J \sim 0.04 - 0.05$. Based on our phase diagram and the extent of the plaquette phase found in experiments, we estimated the effective interlayer coupling in $SrCu_2(BO_3)_2$ to be around $J''/J \sim 0.027$ at ambient pressure. We also investigated the effect of the interlayer coupling on the competition between EP and FP phases and found that the dependence on J'' is very weak for both states, such that the EP state remains lower in energy than the FP state.

From the perspective of tensor network methods, applications to 3D quantum systems have been very limited so far and they form an exciting and challenging frontier. This study constitutes the first application of the LCTM approach beyond benchmark calculations, demonstrating the potential of iPEPS to explore challenging problems in the field of weakly-coupled layered systems.

CHAPTER 6

Conclusion

In this thesis we developed several iPEPS algorithms that can be used for the study of strongly-correlated quantum systems in 3D. In Chap. 3, we focused on general 3D quantum systems for which we developed two iPEPS contraction algorithms. In the cluster contraction, we evaluate a finite cluster of tensors exactly, while the rest of the network is considered approximately. This approach performs a reasonably accurate contraction at a moderate computational cost. With the SU+CTM contraction, on the other hand, a full contraction of the network can be done, which gives a better accuracy, although at a significantly higher numerical cost. In this method, the 3D tensor network is first approximated by a 2D boundary iPEPS, after which we evaluate the resulting quasi-2D network using the CTM. We provided benchmark results for the 3D Heisenberg model and found a good agreement with QMC data. We also studied the 3D Bose-Hubbard model and found a close agreement between the $D = 3$ iPEPS simulations and results from B-DMFT [184] and QMC [185].

Both the cluster and SU+CTM contractions are promising tools to study challenging 3D models, and it will be exciting to let them shed light on these models in future studies. Nevertheless, there is still room for improvement on the algorithmic side. The most pressing problem to tackle, which at the same time is the most challenging one, is to find methods that further reduce the computational cost of the SU+CTM contraction approach without significantly affecting its accuracy. This is critical to make the study of iPEPS with higher D possible, and it would allow us to explore the application of more accurate iPEPS opti-

mization approaches, such as (F)FU [54, 114] or energy minimization schemes based on automatic differentiation [124]. Since the dominant contribution to the computational cost comes from the CTM contraction, it is important to find efficiency gains there, e.g., by exploring one- or two-layer contraction schemes to replace the three-layer approach we use here. It can also be fruitful to study the CU imaginary time evolution scheme to improve over the accuracy of the SU optimization at a more moderate numerical effort than would be the case in the (F)FU or energy minimization.

In Chap. 4, we considered a contraction approach, the LCTM, for layered 2D systems with weak interlayer coupling. The idea of this approach is to decouple the layers of the network away from the center, such that we can contract them using the CTM method. In the center, the layers remain connected to capture the most relevant interlayer correlations. We evaluated its accuracy through simulations of the anisotropic Heisenberg model and showed that the results agree well with QMC, even for relatively strong interlayer couplings. We also simulated the dimer singlet to Néel state transition in the SSM, where we found a close agreement with SE results [70].

In future research, the accuracy of the LCTM can be increased by taking the interlayer correlations into account to higher accuracy. One option is to extend the CTM scheme by introducing a small vertical bond dimension that captures interlayer correlations further away from the center. Such extensions most likely also involve an increase in the numerical cost. It would furthermore be interesting to use the LCTM contraction in an energy minimization approach based on automatic differentiation. Another remaining question is what the best procedure is to accurately extrapolate the results of the LCTM scheme. In our work, we used an extrapolation in the inverse bond dimension, which is known to have limited accuracy. It will be interesting to find ways to improve the quality of the extrapolations, for example, based on finite correlation length scaling that is commonly used for 2D iPEPS [131, 132].

We used the LCTM to evaluate the phase diagram of the SSM around a regime relevant to experimental studies of $SrCu_2(BO_3)_2$ in Chap. 5. An important motivation behind this study was a discrepancy in the extent of the plaquette phase, which is predicted to be larger in theoretical studies of the 2D SSM [69] than what was observed in specific heat measurements [63]. We found that the J'/J-range where the ground state corresponds to the plaquette state quickly decreases when the strength of the interlayer coupling J''/J is increased. The plaquette state vanishes completely around $J''/J \sim 0.04 - 0.05$, which is weaker than an earlier prediction from a SE study [70]. Furthermore, based on the extent of the plaquette phase in Ref. [63] we approximate the interlayer coupling in $SrCu_2(BO_3)_2$ to be around $J''/J \sim 0.027$.

This study demonstrates that it is possible to study challenging and relevant layered 2D systems that are out of reach of QMC with LCTM, and we pave the way for future studies of other layered systems. There are still some open questions regarding the SSM as well. In our study, we find that the intermediate state is formed by the EP state. Experimental evidence exists which suggests that the actual ground state is an FP state. We therefore performed simulations of the FP state as well, and we found that it is higher in energy than the EP state, similar to what has been found in studies of the 2D SSM. In Ref. [236] it was shown that the FP phase can be stabilized through an anisotropy in the coupling strength. It can be interesting to extend this study by looking at the effect of an interlayer coupling in this analysis and whether it affects our estimate of the interlayer coupling obtained for the isotropic case.

With this thesis, we hope to have provided a valuable contribution to the field of strongly-correlated systems, and in particular to tensor network algorithms. Although many 3D systems are difficult to study, we have nonetheless shown that tensor networks can play an important role in their further understanding. There is still plenty of room for the algorithms to be improved, but already in their current form, it will be exciting to apply them to other challenging 3D strongly-correlated systems, such as quantum magnets [55,59–62] and ultra-cold atomic systems [56, 57], especially those that are inaccessible by QMC. It will also be interesting to extend the current methods to study fermionic models based on ideas from Refs. [116,201,203]. Further comparisons of our 3D iPEPS algorithms to other methods for 3D systems will also be desirable, in particular other generalizations of tensor networks to 3D, such as 3D TTN [66] and 3D DMRG [241].

Bibliography

[1] A. Einstein, "Über die von der molekularkinetischen Theorie der Wärme geforderte Bewegung von in ruhenden Flüssigkeiten suspendierten Teilchen," *Ann. Phys. (Berl.)*, vol. 322, no. 8, p. 549, 1905.

[2] J. Perrin, "Mouvement Brownien et réalité moléculaire," *Ann. Chim. Phys.*, vol. 18, p. 1, 1909.

[3] E. Rutherford, "The scattering of α and β particles by matter and the structure of the atom," *Philos. Mag.*, vol. 21, p. 669, 1911.

[4] N. Bohr, "On the constitution of atoms and molecules," *Philos. Mag.*, vol. 26, p. 1, 1913.

[5] C. L. Cowan, F. Reines, F. B. Harrison, H. W. Kruse, and A. D. McGuire, "Detection of the free neutrino: a confirmation," *Science*, vol. 124, no. 3212, p. 103, 1956.

[6] G. Danby, J.-M. Gaillard, K. Goulianos, L. M. Lederman, N. Mistry, M. Schwartz, and J. Steinberger, "Observation of high-energy neutrino reactions and the existence of two kinds of neutrinos," *Phys. Rev. Lett.*, vol. 9, p. 36, 1962.

[7] K. Kodama, N. Ushida, C. Andreopoulos, N. Saoulidou, G. Tzanakos, P. Yager, B. Baller, D. Boehnlein, W. Freeman, B. Lundberg, J. Morfin, R. Rameika, J. Yun, J. Song, C. Yoon, S. Chung, P. Berghaus, M. Kubantsev, N. Reay, R. Sidwell, N. Stanton, S. Yoshida, S. Aoki, T. Hara, J. Rhee, D. Ciampa, C. Erickson, M. Graham, K. Heller, R. Rusack, R. Schwienhorst, J. Sielaff, J. Trammell, J. Wilcox, K. Hoshino, H. Jiko, M. Miyanishi, M. Komatsu, M. Nakamura, T. Nakano, K. Niwa, N. Nonaka, K. Okada, O. Sato, T. Akdogan, V. Paolone, C. Rosenfeld, A. Kulik, T. Kafka, W. Oliver, T. Patzak, and J. Schneps, "Observation of tau neutrino interactions," *Phys. Lett. B*, vol. 504, no. 3, p. 218, 2001.

[8] J. Barrow-Green, "The three-body problem," in *The Princeton companion to mathematics* (T. Gowers, J. Barrow-Green, and I. Leader, eds.), pp. 726–728, Princeton University Press, 2008.

[9] P. W. Anderson, "More is different," *Science*, vol. 177, no. 4047, p. 393, 1972.

[10] J. Hubbard, "Electron correlations in narrow energy bands," *Proc. R. Soc. Lond. A*, vol. 276, p. 238, 1963.

[11] A. Altland and B. Simons, *Condensed matter field theory*, ch. 2, pp. 59–66. Cambridge University Press, 2 ed., 2010.

[12] D. P. Arovas, E. Berg, S. A. Kivelson, and S. Raghu, "The Hubbard model," *Annu. Rev. Condens. Matter Phys.*, vol. 13, no. 1, p. 239, 2022.

[13] M. Qin, T. Schäfer, S. Andergassen, P. Corboz, and E. Gull, "The Hubbard model: A computational perspective," *Annu. Rev. Condens. Matter Phys.*, vol. 13, no. 1, p. 275, 2022.

[14] M. P. A. Fisher, P. B. Weichman, G. Grinstein, and D. S. Fisher, "Boson localization and the superfluid-insulator transition," *Phys. Rev. B*, vol. 40, no. 1, p. 546, 1989.

[15] E. Ising, "Beitrag zur Theorie des Ferromagnetismus," *Z. Phys.*, vol. 31, p. 253, 1925.

[16] L. Onsager, "Crystal statistics. I. A two-dimensional model with an order-disorder transition," *Phys. Rev.*, vol. 65, p. 117, 1944.

[17] H. A. Bethe, "Zur Theorie der Metalle," *Z. Phys.*, vol. 71, p. 205, 1931.

[18] L. Hulthén, "Über das Austauschproblem eines Kristalles," *Ark. Mat. Astron. Fys.*, vol. 26A, 1938.

[19] E. H. Lieb and F. Y. Wu, "Absence of Mott transition in an exact solution of the short-range, one-band model in one dimension," *Phys. Rev. Lett.*, vol. 20, p. 1445, 1968.

[20] M. Troyer and U.-J. Wiese, "Computational complexity and fundamental limitations to fermionic quantum Monte Carlo simulations," *Phys. Rev. Lett.*, vol. 94, p. 170201, 2005.

[21] S. R. White, "Density matrix formulation for quantum renormalization groups," *Phys. Rev. Lett.*, vol. 69, p. 2863, 1992.

[22] U. Schollwöck, "The density-matrix renormalization group in the age of matrix product states," *Ann. Phys. (N. Y.)*, vol. 326, no. 1, p. 96, 2011.

[23] M. Fannes, B. Nachtergaele, and R. F. Werner, "Finitely correlated states on quantum spin chains," *Commun. Math. Phys.*, vol. 144, no. 3, p. 443, 1992.

[24] S. Östlund and S. Rommer, "Thermodynamic limit of density matrix renormalization," *Phys. Rev. Lett.*, vol. 75, p. 3537, 1995.

[25] J. Eisert, M. Cramer, and M. B. Plenio, "Colloquium: Area laws for the entanglement entropy," *Rev. Mod. Phys.*, vol. 82, p. 277, 2010.

[26] Y. Hieida, K. Okunishi, and Y. Akutsu, "Numerical renormalization approach to two-dimensional quantum antiferromagnets with valence-bond-solid type ground state," *New J. Phys.*, vol. 1, p. 7, 1999.

[27] N. Maeshima, Y. Hieida, Y. Akutsu, T. Nishino, and K. Okunishi, "Vertical density matrix algorithm: A higher-dimensional numerical renormalization scheme based on the tensor product state ansatz," *Phys. Rev. E*, vol. 64, p. 016705, 2001.

[28] Y. Nishio, N. Maeshima, A. Gendiar, and T. Nishino, "Tensor product variational formulation for quantum systems." arXiv:cond-mat/0401115, 2004.

[29] F. Verstraete and J. I. Cirac, "Renormalization algorithms for quantum-many body systems in two and higher dimensions." arXiv:cond-mat/0407066, 2004.

[30] V. Murg, F. Verstraete, and J. I. Cirac, "Variational study of hard-core bosons in a two-dimensional optical lattice using projected entangled pair states," *Phys. Rev. A*, vol. 75, p. 033605, 2007.

[31] P. Corboz and F. Mila, "Crystals of bound states in the magnetization plateaus of the Shastry-Sutherland model," *Phys. Rev. Lett.*, vol. 112, p. 147203, 2014.

[32] P. Corboz, T. M. Rice, and M. Troyer, "Competing states in the t-J model: Uniform d-wave state versus stripe state," *Phys. Rev. Lett.*, vol. 113, p. 046402, 2014.

[33] H. J. Liao, Z. Y. Xie, J. Chen, Z. Y. Liu, H. D. Xie, R. Z. Huang, B. Normand, and T. Xiang, "Gapless spin-liquid ground state in the $S = 1/2$ kagome antiferromagnet," *Phys. Rev. Lett.*, vol. 118, p. 137202, 2017.

[34] I. Niesen and P. Corboz, "Emergent Haldane phase in the $S = 1$ bilinear-biquadratic Heisenberg model on the square lattice," *Phys. Rev. B*, vol. 95, p. 180404(R), 2017.

[35] B.-X. Zheng, C.-M. Chung, P. Corboz, G. Ehlers, M.-P. Qin, R. M. Noack, H. Shi, S. R. White, S. Zhang, and G. K.-L. Chan, "Stripe order in the underdoped region of the two-dimensional Hubbard model," *Science*, vol. 358, no. 6367, p. 1155, 2017.

[36] S. S. Jahromi and R. Orús, "Spin-$\frac{1}{2}$ Heisenberg antiferromagnet on the star lattice: Competing valence-bond-solid phases studied by means of tensor networks," *Phys. Rev. B*, vol. 98, p. 155108, 2018.

[37] H.-Y. Lee and N. Kawashima, "Spin-one bilinear-biquadratic model on a star lattice," *Phys. Rev. B*, vol. 97, no. 20, p. 205123, 2018.

[38] H. Yamaguchi, Y. Sasaki, T. Okubo, M. Yoshida, T. Kida, M. Hagiwara, Y. Kono, S. Kittaka, T. Sakakibara, M. Takigawa, Y. Iwasaki, and Y. Hosokoshi, "Field-enhanced quantum fluctuation in an $S = \frac{1}{2}$ frustrated square lattice," *Phys. Rev. B*, vol. 98, p. 094402, 2018.

[39] R. Haghshenas and D. N. Sheng, "$U(1)$-symmetric infinite projected entangled-pair states study of the spin-1/2 square J_1-J_2 Heisenberg model," *Phys. Rev. B*, vol. 97, p. 174408, 2018.

[40] J.-Y. Chen, L. Vanderstraeten, S. Capponi, and D. Poilblanc, "Non-Abelian chiral spin liquid in a quantum antiferromagnet revealed by an iPEPS study," *Phys. Rev. B*, vol. 98, no. 18, p. 184409, 2018.

[41] R. Haghshenas, S.-S. Gong, and D. N. Sheng, "Single-layer tensor network study of the Heisenberg model with chiral interactions on a kagome lattice," *Phys. Rev. B*, vol. 99, no. 17, p. 174423, 2019.

[42] B. Ponsioen, S. S. Chung, and P. Corboz, "Period 4 stripe in the extended two-dimensional Hubbard model," *Phys. Rev. B*, vol. 100, p. 195141, 2019.

[43] S. S. Chung and P. Corboz, "SU(3) fermions on the honeycomb lattice at $\frac{1}{3}$ filling," *Phys. Rev. B*, vol. 100, p. 035134, 2019.

[44] A. Kshetrimayum, C. Balz, B. Lake, and J. Eisert, "Tensor network investigation of the double layer kagome compound $Ca_{10}Cr_7O_{28}$," *Ann. Phys. (N. Y.)*, vol. 421, p. 168292, 2020.

[45] Z. Shi, W. Steinhardt, D. Graf, P. Corboz, F. Weickert, N. Harrison, M. Jaime, C. Marjerrison, H. A. Dabkowska, F. Mila, and S. Haravifard, "Emergent bound states and impurity pairs in chemically doped Shastry-Sutherland system," *Nat. Commun.*, vol. 10, no. 1, p. 2439, 2019.

[46] H.-Y. Lee, R. Kaneko, L. E. Chern, T. Okubo, Y. Yamaji, N. Kawashima, and Y. B. Kim, "Magnetic field induced quantum phases in a tensor network study of Kitaev magnets," *Nat. Commun.*, vol. 11, no. 1, p. 1639, 2020.

[47] O. Gauthé, S. Capponi, M. Mambrini, and D. Poilblanc, "Quantum spin liquid phases in the bilinear-biquadratic two-SU(4)-fermion Hamiltonian on the square lattice," *Phys. Rev. B*, vol. 101, no. 20, p. 205144, 2020.

[48] J.-Y. Chen, S. Capponi, A. Wietek, M. Mambrini, N. Schuch, and D. Poilblanc, "$SU(3)_1$ chiral spin liquid on the square lattice: A view from symmetric projected entangled pair states," *Phys. Rev. Lett.*, vol. 125, p. 017201, 2020.

[49] W.-Y. Liu, S.-S. Gong, Y.-B. Li, D. Poilblanc, W.-Q. Chen, and Z.-C. Gu, "Gapless quantum spin liquid and global phase diagram of the spin-1/2 $J_1 - J_2$ square antiferromagnetic Heisenberg model," *Sci. Bull.*, vol. 67, no. 10, p. 1034, 2022.

[50] J. Hasik, D. Poilblanc, and F. Becca, "Investigation of the Néel phase of the frustrated Heisenberg antiferromagnet by differentiable symmetric tensor networks," *SciPost Phys.*, vol. 10, p. 012, 2021.

[51] W.-Y. Liu, J. Hasik, S.-S. Gong, D. Poilblanc, W.-Q. Chen, and Z.-C. Gu, "Emergence of gapless quantum spin liquid from deconfined quantum critical point," *Phys. Rev. X*, vol. 12, p. 031039, 2022.

[52] M. Peschke, B. Ponsioen, and P. Corboz, "Competing states in the two-dimensional frustrated kondo-necklace model," *Phys. Rev. B*, vol. 106, p. 205140, Nov 2022.

[53] S. Niu, J. Hasik, J.-Y. Chen, and D. Poilblanc, "Chiral spin liquids on the kagome lattice with projected entangled simplex states," *Phys. Rev. B*, vol. 106, p. 245119, 2022.

[54] J. Jordan, R. Orús, G. Vidal, F. Verstraete, and J. I. Cirac, "Classical simulation of infinite-size quantum lattice systems in two spatial dimensions," *Phys. Rev. Lett.*, vol. 101, p. 250602, 2008.

[55] R. Schäfer, I. Hagymási, R. Moessner, and D. J. Luitz, "Pyrochlore $S = \frac{1}{2}$ Heisenberg antiferromagnet at finite temperature," *Phys. Rev. B*, vol. 102, p. 054408, 2020.

[56] M. A. Cazalilla and A. M. Rey, "Ultracold fermi gases with emergent SU(N) symmetry," *Rep. Prog. Phys.*, vol. 77, no. 12, p. 124401, 2014.

[57] C. Gross and I. Bloch, "Quantum simulations with ultracold atoms in optical lattices," *Science*, vol. 357, no. 6355, p. 995, 2017.

[58] J. G. Bednorz and K. A. Müller, "Possible high T_c superconductivity in the Ba-La-Cu-O system," *Z. Phys. B*, vol. 64, no. 2, p. 189, 1986.

[59] S. Miyahara and K. Ueda, "Theory of the orthogonal dimer Heisenberg spin model for $SrCu_2(BO_3)_2$," *J. Phys. Condens. Matter*, vol. 15, no. 9, p. R327, 2003.

[60] M. P. Shores, E. A. Nytko, B. M. Bartlett, and D. G. Nocera, "A structurally perfect $S = 1/2$ kagomé antiferromagnet," *J. Am. Chem. Soc.*, vol. 127, no. 39, p. 13462, 2005.

[61] Y. Shirata, H. Tanaka, A. Matsuo, and K. Kindo, "Experimental realization of a spin-1/2 triangular-lattice Heisenberg antiferromagnet," *Phys. Rev. Lett.*, vol. 108, p. 057205, 2012.

[62] H. Takagi, T. Takayama, G. Jackeli, G. Khaliullin, and S. E. Nagler, "Concept and realization of Kitaev quantum spin liquids," *Nat. Rev. Phys.*, vol. 1, no. 4, p. 264, 2019.

[63] J. Guo, G. Sun, B. Zhao, L. Wang, W. Hong, V. A. Sidorov, N. Ma, Q. Wu, S. Li, Z. Y. Meng, A. W. Sandvik, and L. Sun, "Quantum phases of $SrCu_2(BO_3)_2$ from high-pressure thermodynamics," *Phys. Rev. Lett.*, vol. 124, p. 206602, May 2020.

[64] T. M. R. Byrnes, P. Sriganesh, R. J. Bursill, and C. J. Hamer, "Density matrix renormalization group approach to the massive Schwinger model," *Phys. Rev. D*, vol. 66, p. 013002, 2002.

[65] L. Tagliacozzo and G. Vidal, "Entanglement renormalization and gauge symmetry," *Phys. Rev. B*, vol. 83, no. 11, p. 115127, 2011.

[66] G. Magnifico, T. Felser, P. Silvi, and S. Montangero, "Lattice quantum electrodynamics in (3+1)-dimensions at finite density with tensor networks," *Nat. Commun.*, vol. 12, p. 3600, 2021.

[67] V. Coffman, J. Kundu, and W. K. Wootters, "Distributed entanglement," *Phys. Rev. A*, vol. 61, p. 052306, 2000.

[68] T. J. Osborne and F. Verstraete, "General monogamy inequality for bipartite qubit entanglement," *Phys. Rev. Lett.*, vol. 96, p. 220503, 2006.

[69] P. Corboz and F. Mila, "Tensor network study of the Shastry-Sutherland model in zero magnetic field," *Phys. Rev. B*, vol. 87, p. 115144, 2013.

[70] A. Koga, "Ground-state phase diagram for the three-dimensional orthogonal-dimer system," *J. Phys. Soc. Jpn.*, vol. 69, no. 11, p. 3509, 2000.

[71] M. B. Hastings, "An area law for one-dimensional quantum systems," *J. Stat. Mech.: Theory Exp.*, vol. 2007, no. 08, p. P08024, 2007.

[72] G. Vidal, J. I. Latorre, E. Rico, and A. Kitaev, "Entanglement in quantum critical phenomena," *Phys. Rev. Lett.*, vol. 90, p. 227902, 2003.

[73] P. Calabrese and J. Cardy, "Entanglement entropy and quantum field theory," *J. Stat. Mech.: Theory Exp.*, vol. 2004, no. 06, p. P06002, 2004.

[74] G. Vidal, "Class of quantum many-body states that can be efficiently simulated," *Phys. Rev. Lett.*, vol. 101, p. 110501, 2008.

[75] G. Evenbly and G. Vidal, "Class of highly entangled many-body states that can be efficiently simulated," *Phys. Rev. Lett.*, vol. 112, p. 240502, 2014.

[76] Y.-Y. Shi, L.-M. Duan, and G. Vidal, "Classical simulation of quantum many-body systems with a tree tensor network," *Phys. Rev. A*, vol. 74, p. 022320, 2006.

[77] R. N. C. Pfeifer, G. Evenbly, S. Singh, and G. Vidal, "NCON: A tensor network contractor for MATLAB." arXiv:1402.0939 [physics.comp-ph], 2014.

[78] R. N. C. Pfeifer, J. Haegeman, and F. Verstraete, "Faster identification of optimal contraction sequences for tensor networks," *Phys. Rev. E*, vol. 90, p. 033315, 2014.

[79] G. Vidal, "Efficient classical simulation of slightly entangled quantum computations," *Phys. Rev. Lett.*, vol. 91, p. 147902, 2003.

[80] G. Vidal, "Efficient simulation of one-dimensional quantum many-body systems," *Phys. Rev. Lett.*, vol. 93, p. 040502, 2004.

[81] V. Zauner-Stauber, L. Vanderstraeten, M. T. Fishman, F. Verstraete, and J. Haegeman, "Variational optimization algorithms for uniform matrix product states," *Phys. Rev. B*, vol. 97, p. 045145, 2018.

[82] H. N. Phien, I. P. McCulloch, and G. Vidal, "Fast convergence of imaginary time evolution tensor network algorithms by recycling the environment," *Phys. Rev. B*, vol. 91, p. 115137, 2015.

[83] R. Orús and G. Vidal, "Infinite time-evolving block decimation algorithm beyond unitary evolution," *Phys. Rev. B*, vol. 78, p. 155117, 2008.

[84] S. Liang and H. Pang, "Approximate diagonalization using the density matrix renormalization-group method: A two-dimensional-systems perspective," *Phys. Rev. B*, vol. 49, p. 9214, 1994.

[85] S. R. White, "Spin gaps in a frustrated Heisenberg model for CaV_4O_9," *Phys. Rev. Lett.*, vol. 77, p. 3633, 1996.

[86] E. Stoudenmire and S. R. White, "Studying two-dimensional systems with the density matrix renormalization group," *Annu. Rev. Condens. Matter Phys.*, vol. 3, no. 1, p. 111, 2012.

[87] S. Depenbrock, I. P. McCulloch, and U. Schollwöck, "Nature of the spin-liquid ground state of the $S = 1/2$ Heisenberg model on the kagome lattice," *Phys. Rev. Lett.*, vol. 109, p. 067201, 2012.

[88] D. Varjas, M. P. Zaletel, and J. E. Moore, "Chiral Luttinger liquids and a generalized Luttinger theorem in fractional quantum Hall edges via finite-entanglement scaling," *Phys. Rev. B*, vol. 88, p. 155314, 2013.

[89] J. P. F. LeBlanc, A. E. Antipov, F. Becca, I. W. Bulik, G. K.-L. Chan, C.-M. Chung, Y. Deng, M. Ferrero, T. M. Henderson, C. A. Jiménez-Hoyos, E. Kozik, X.-W. Liu, A. J. Millis, N. V. Prokof'ev, M. Qin, G. E. Scuseria, H. Shi, B. V. Svistunov, L. F. Tocchio, I. S. Tupitsyn, S. R. White, S. Zhang, B.-X. Zheng, Z. Zhu, and E. Gull, "Solutions of the two-dimensional Hubbard model: Benchmarks and results from a wide range of numerical algorithms," *Phys. Rev. X*, vol. 5, p. 041041, 2015.

[90] A. Wietek, Y.-Y. He, S. R. White, A. Georges, and E. M. Stoudenmire, "Stripes, antiferromagnetism, and the pseudogap in the doped Hubbard model at finite temperature," *Phys. Rev. X*, vol. 11, p. 031007, 2021.

[91] F. Verstraete, M. M. Wolf, D. Perez-Garcia, and J. I. Cirac, "Criticality, the area law, and the computational power of projected entangled pair states," *Phys. Rev. Lett.*, vol. 96, p. 220601, 2006.

[92] N. Schuch, M. M. Wolf, F. Verstraete, and J. I. Cirac, "Computational complexity of projected entangled pair states," *Phys. Rev. Lett.*, vol. 98, p. 140506, 2007.

[93] R. J. Baxter, *Exactly Solved Models in Statistical Mechanics*. Academic Press, 1982.

[94] T. Nishino and K. Okunishi, "Corner transfer matrix renormalization group method," *J. Phys. Soc. Jpn.*, vol. 65, no. 4, p. 891, 1996.

[95] R. Orús and G. Vidal, "Simulation of two-dimensional quantum systems on an infinite lattice revisited: Corner transfer matrix for tensor contraction," *Phys. Rev. B*, vol. 80, p. 094403, 2009.

[96] P. Corboz, S. R. White, G. Vidal, and M. Troyer, "Stripes in the two-dimensional $t - J$ model with infinite projected entangled-pair states," *Phys. Rev. B*, vol. 84, no. 4, p. 041108(R), 2011.

[97] R. Orús, "Exploring corner transfer matrices and corner tensors for the classical simulation of quantum lattice systems," *Phys. Rev. B*, vol. 85, p. 205117, 2012.

[98] T. Okubo. personal communication.

[99] M. Levin and C. P. Nave, "Tensor renormalization group approach to two-dimensional classical lattice models," *Phys. Rev. Lett.*, vol. 99, p. 120601, 2007.

[100] Z. Y. Xie, H. C. Jiang, Q. N. Chen, Z. Y. Weng, and T. Xiang, "Second renormalization of tensor-network states," *Phys. Rev. Lett.*, vol. 103, p. 160601, 2009.

[101] Z. Y. Xie, J. Chen, M. P. Qin, J. W. Zhu, L. P. Yang, and T. Xiang, "Coarse-graining renormalization by higher-order singular value decomposition," *Phys. Rev. B*, vol. 86, p. 045139, 2012.

[102] G. Evenbly and G. Vidal, "Tensor network renormalization," *Phys. Rev. Lett.*, vol. 115, p. 180405, 2015.

[103] S. Yang, Z.-C. Gu, and X.-G. Wen, "Loop optimization for tensor network renormalization," *Phys. Rev. Lett.*, vol. 118, p. 110504, 2017.

[104] M. Hauru, C. Delcamp, and S. Mizera, "Renormalization of tensor networks using graph-independent local truncations," *Phys. Rev. B*, vol. 97, p. 045111, 2018.

[105] L. De Lathauwer, B. De Moor, and J. Vandewalle, "A multilinear singular value decomposition," *SIAM J. Matrix Anal. Appl.*, vol. 21, no. 4, p. 1253, 2000.

[106] L. De Lathauwer, B. De Moor, and J. Vandewalle, "On the best rank-1 and rank-(R_1 ,R_2 ,. . .,R_N) approximation of higher-order tensors," *SIAM J. Matrix Anal. Appl.*, vol. 21, no. 4, p. 1324, 2000.

[107] S. Iino, S. Morita, and N. Kawashima, "Boundary tensor renormalization group," *Phys. Rev. B*, vol. 100, p. 035449, 2019.

[108] M. T. Fishman, L. Vanderstraeten, V. Zauner-Stauber, J. Haegeman, and F. Verstraete, "Faster methods for contracting infinite two-dimensional tensor networks," *Phys. Rev. B*, vol. 98, p. 235148, 2018.

[109] I. Affleck, T. Kennedy, E. H. Lieb, and H. Tasaki, "Rigorous results on valence-bond ground states in antiferromagnets," *Phys. Rev. Lett.*, vol. 59, p. 799, 1987.

[110] I. Affleck, T. Kennedy, E. H. Lieb, and H. Tasaki, "Valence bond ground states in isotropic quantum antiferromagnets," *Commun. Math. Phys.*, vol. 115, no. 3, p. 477, 1988.

[111] A. Kitaev, "Fault-tolerant quantum computation by anyons," *Annals of Physics*, vol. 303, no. 1, pp. 2–30, 2003.

[112] G. Vidal, "Classical simulation of infinite-size quantum lattice systems in one spatial dimension," *Phys. Rev. Lett.*, vol. 98, p. 070201, 2007.

[113] M. Lubasch, J. I. Cirac, and M.-C. Bañuls, "Algorithms for finite projected entangled pair states," *Phys. Rev. B*, vol. 90, p. 064425, 2014.

[114] H. N. Phien, J. A. Bengua, H. D. Tuan, P. Corboz, and R. Orús, "Infinite projected entangled pair states algorithm improved: Fast full update and gauge fixing," *Phys. Rev. B*, vol. 92, p. 035142, 2015.

[115] H. C. Jiang, Z. Y. Weng, and T. Xiang, "Accurate determination of tensor network state of quantum lattice models in two dimensions," *Phys. Rev. Lett.*, vol. 101, p. 090603, 2008.

[116] P. Corboz, R. Orús, B. Bauer, and G. Vidal, "Simulation of strongly correlated fermions in two spatial dimensions with fermionic projected entangled-pair states," *Phys. Rev. B*, vol. 81, p. 165104, 2010.

[117] H. Kalis, D. Klagges, R. Orús, and K. P. Schmidt, "Fate of the cluster state on the square lattice in a magnetic field," *Phys. Rev. A*, vol. 86, p. 022317, 2012.

[118] S.-J. Ran, W. Li, B. Xi, Z. Zhang, and G. Su, "Optimized decimation of tensor networks with super-orthogonalization for two-dimensional quantum lattice models," *Phys. Rev. B*, vol. 86, p. 134429, 2012.

[119] L. Wang and F. Verstraete, "Cluster update for tensor network states." arXiv:1110.4362 [cond-mat.str-el], 2011.

[120] M. Lubasch, J. I. Cirac, and M.-C. Bañuls, "Unifying projected entangled pair state contractions," *New J. Phys.*, vol. 16, no. 3, p. 033014, 2014.

[121] J. Dziarmaga, "Time evolution of an infinite projected entangled pair state: Neighborhood tensor update," *Phys. Rev. B*, vol. 104, p. 094411, 2021.

[122] P. Corboz, "Variational optimization with infinite projected entangled-pair states," *Phys. Rev. B*, vol. 94, p. 035133, 2016.

[123] L. Vanderstraeten, J. Haegeman, P. Corboz, and F. Verstraete, "Gradient methods for variational optimization of projected entangled-pair states," *Phys. Rev. B*, vol. 94, p. 155123, 2016.

[124] H.-J. Liao, J.-G. Liu, L. Wang, and T. Xiang, "Differentiable programming tensor networks," *Phys. Rev. X*, vol. 9, p. 031041, 2019.

[125] S. Singh, R. N. C. Pfeifer, and G. Vidal, "Tensor network states and algorithms in the presence of a global U(1) symmetry," *Phys. Rev. B*, vol. 83, p. 115125, 2011.

[126] B. Bauer, P. Corboz, R. Orús, and M. Troyer, "Implementing global abelian symmetries in projected entangled-pair state algorithms," *Phys. Rev. B*, vol. 83, p. 125106, 2011.

[127] L. Tagliacozzo, T. R. de Oliveira, S. Iblisdir, and J. I. Latorre, "Scaling of entanglement support for matrix product states," *Phys. Rev. B*, vol. 78, p. 024410, 2008.

[128] F. Pollmann, S. Mukerjee, A. M. Turner, and J. E. Moore, "Theory of finite-entanglement scaling at one-dimensional quantum critical points," *Phys. Rev. Lett.*, vol. 102, p. 255701, 2009.

[129] B. Pirvu, G. Vidal, F. Verstraete, and L. Tagliacozzo, "Matrix product states for critical spin chains: Finite-size versus finite-entanglement scaling," *Phys. Rev. B*, vol. 86, p. 075117, 2012.

[130] V. Stojevic, J. Haegeman, I. P. McCulloch, L. Tagliacozzo, and F. Verstraete, "Conformal data from finite entanglement scaling," *Phys. Rev. B*, vol. 91, p. 035120, 2015.

[131] M. Rader and A. M. Läuchli, "Finite correlation length scaling in Lorentz-invariant gapless iPEPS wave functions," *Phys. Rev. X*, vol. 8, p. 031030, 2018.

[132] P. Corboz, P. Czarnik, G. Kapteijns, and L. Tagliacozzo, "Finite correlation length scaling with infinite projected entangled-pair states," *Phys. Rev. X*, vol. 8, p. 031031, 2018.

[133] P. Corboz, "Improved energy extrapolation with infinite projected entangled-pair states applied to the two-dimensional Hubbard model," *Phys. Rev. B*, vol. 93, p. 045116, 2016.

[134] P. C. G. Vlaar and P. Corboz, "Simulation of three-dimensional quantum systems with projected entangled-pair states," *Phys. Rev. B*, vol. 103, p. 205137, 2021.

[135] I. Niesen and P. Corboz, "A tensor network study of the complete ground state phase diagram of the spin-1 bilinear-biquadratic Heisenberg model on the square lattice," *SciPost Phys.*, vol. 3, p. 030, 2017.

[136] W. Li, S.-J. Ran, S.-S. Gong, Y. Zhao, B. Xi, F. Ye, and G. Su, "Linearized tensor renormalization group algorithm for the calculation of thermodynamic properties of quantum lattice models," *Phys. Rev. Lett.*, vol. 106, p. 127202, 2011.

[137] P. Czarnik, L. Cincio, and J. Dziarmaga, "Projected entangled pair states at finite temperature: Imaginary time evolution with ancillas," *Phys. Rev. B*, vol. 86, p. 245101, 2012.

[138] S.-J. Ran, B. Xi, T. Liu, and G. Su, "Theory of network contractor dynamics for exploring thermodynamic properties of two-dimensional quantum lattice models," *Phys. Rev. B*, vol. 88, p. 064407, 2013.

[139] P. Czarnik and J. Dziarmaga, "Projected entangled pair states at finite temperature: Iterative self-consistent bond renormalization for exact imaginary time evolution," *Phys. Rev. B*, vol. 92, p. 035120, 2015.

[140] P. Czarnik and J. Dziarmaga, "Variational approach to projected entangled pair states at finite temperature," *Phys. Rev. B*, vol. 92, p. 035152, 2015.

[141] C. Peng, S.-J. Ran, T. Liu, X. Chen, and G. Su, "Fermionic algebraic quantum spin liquid in an octa-kagome frustrated antiferromagnet," *Phys. Rev. B*, vol. 95, p. 075140, 2017.

[142] Y.-W. Dai, Q.-Q. Shi, S. Y. Cho, M. T. Batchelor, and H.-Q. Zhou, "Finite-temperature fidelity and von Neumann entropy in the honeycomb spin lattice with quantum Ising interaction," *Phys. Rev. B*, vol. 95, p. 214409, 2017.

[143] P. Czarnik, J. Dziarmaga, and A. M. Oleś, "Overcoming the sign problem at finite temperature: Quantum tensor network for the orbital e_g model on an infinite square lattice," *Phys. Rev. B*, vol. 96, p. 014420, 2017.

[144] S.-J. Ran, W. Li, S.-S. Gong, A. Weichselbaum, J. von Delft, and G. Su, "Emergent spin-1 trimerized valence bond crystal in the spin-$\frac{1}{2}$ Heisenberg model on the star lattice," *Phys. Rev. B*, vol. 97, p. 075146, 2018.

[145] P. Czarnik and J. Dziarmaga, "Time evolution of an infinite projected entangled pair state: An algorithm from first principles," *Phys. Rev. B*, vol. 98, p. 045110, 2018.

[146] X. Chen, S.-J. Ran, T. Liu, C. Peng, Y.-Z. Huang, and G. Su, "Thermodynamics of spin-1/2 kagomé Heisenberg antiferromagnet: Algebraic paramagnetic liquid and finite-temperature phase diagram," *Sci. Bull.*, vol. 63, no. 23, p. 1545, 2018.

[147] A. Kshetrimayum, M. Rizzi, J. Eisert, and R. Orús, "Tensor network annealing algorithm for two-dimensional thermal states," *Phys. Rev. Lett.*, vol. 122, p. 070502, Feb 2019.

[148] P. Czarnik, J. Dziarmaga, and P. Corboz, "Time evolution of an infinite projected entangled pair state: An efficient algorithm," *Phys. Rev. B*, vol. 99, p. 035115, 2019.

[149] S.-J. Ran, B. Xi, C. Peng, G. Su, and M. Lewenstein, "Efficient quantum simulation for thermodynamics of infinite-size many-body systems in arbitrary dimensions," *Phys. Rev. B*, vol. 99, p. 205132, 2019.

[150] A. Wietek, P. Corboz, S. Wessel, B. Normand, F. Mila, and A. Honecker, "Thermodynamic properties of the Shastry-Sutherland model throughout the dimer-product phase," *Phys. Rev. Res.*, vol. 1, p. 033038, 2019.

[151] P. Czarnik and P. Corboz, "Finite correlation length scaling with infinite projected entangled pair states at finite temperature," *Phys. Rev. B*, vol. 99, no. 24, p. 245107, 2019.

[152] P. Czarnik, A. Francuz, and J. Dziarmaga, "Tensor network simulation of the Kitaev-Heisenberg model at finite temperature," *Phys. Rev. B*, vol. 100, no. 16, p. 165147, 2019.

[153] J. L. Jiménez, S. P. G. Crone, E. Fogh, M. E. Zayed, R. Lortz, E. Pomjakushina, K. Conder, A. M. Läuchli, L. Weber, S. Wessel, A. Honecker, B. Normand, C. Rüegg, P. Corboz, H. M. Rønnow, and F. Mila, "A quantum magnetic analogue to the critical point of water," *Nature (London)*, vol. 592, p. 370, 2021.

[154] P. Czarnik, M. M. Rams, P. Corboz, and J. Dziarmaga, "Tensor network study of the $m = \frac{1}{2}$ magnetization plateau in the Shastry-Sutherland model at finite temperature," *Phys. Rev. B*, vol. 103, p. 075113, 2021.

[155] L. Vanderstraeten, J. Haegeman, and F. Verstraete, "Simulating excitation spectra with projected entangled-pair states," *Phys. Rev. B*, vol. 99, p. 165121, 2019.

[156] B. Ponsioen and P. Corboz, "Excitations with projected entangled pair states using the corner transfer matrix method," *Phys. Rev. B*, vol. 101, p. 195109, 2020.

[157] C. Hubig and J. I. Cirac, "Time-dependent study of disordered models with infinite projected entangled pair states," *SciPost Phys.*, vol. 6, p. 31, 2019.

[158] C. Hubig, A. Bohrdt, M. Knap, F. Grusdt, and J. I. Cirac, "Evaluation of time-dependent correlators after a local quench in iPEPS: Hole motion in the $t - J$ model," *SciPost Phys.*, vol. 8, p. 21, 2020.

[159] A. Kshetrimayum, M. Goihl, and J. Eisert, "Time evolution of many-body localized systems in two spatial dimensions," *Phys. Rev. B*, vol. 102, p. 235132, 2020.

[160] A. Kshetrimayum, H. Weimer, and R. Orús, "A simple tensor network algorithm for two-dimensional steady states," *Nat. Commun.*, vol. 8, no. 1, p. 1291, 2017.

[161] T. Nishino and K. Okunishi, "A density matrix algorithm for 3d classical models," *J. Phys. Soc. Jpn.*, vol. 67, no. 9, p. 3066, 1998.

[162] A. García-Sáez and J. I. Latorre, "Renormalization group contraction of tensor networks in three dimensions," *Phys. Rev. B*, vol. 87, p. 085130, 2013.

[163] P. Teng, "Generalization of the tensor renormalization group approach to 3-D or higher dimensions," *Phys. A: Stat. Mech. Appl.*, vol. 472, p. 117, 2017.

[164] T. Nishino, K. Okunishi, Y. Hieida, N. Maeshima, and Y. Akutsu, "Self-consistent tensor product variational approximation for 3D classical models," *Nucl. Phys. B*, vol. 575, no. 3, p. 504, 2000.

[165] T. Nishino, Y. Hieida, K. Okunishi, N. Maeshima, Y. Akutsu, and A. Gendiar, "Two-dimensional tensor product variational formulation," *Prog. Theor. Phys.*, vol. 105, no. 3, p. 409, 2001.

[166] A. Gendiar and T. Nishino, "Latent heat calculation of the three-dimensional $q = 3$, 4, and 5 Potts models by the tensor product variational approach," *Phys. Rev. E*, vol. 65, p. 046702, 2002.

[167] A. Gendiar, N. Maeshima, and T. Nishino, "Stable optimization of a tensor product variational state," *Prog. Theor. Phys.*, vol. 110, no. 4, p. 691, 2003.

[168] A. Gendiar and T. Nishino, "Phase diagram of the three-dimensional axial next-nearest-neighbor Ising model," *Phys. Rev. B*, vol. 71, p. 024404, 2005.

[169] L. Vanderstraeten, B. Vanhecke, and F. Verstraete, "Residual entropies for three-dimensional frustrated spin systems with tensor networks," *Phys. Rev. E*, vol. 98, p. 042145, 2018.

[170] S.-J. Ran, A. Piga, C. Peng, G. Su, and M. Lewenstein, "Few-body systems capture many-body physics: Tensor network approach," *Phys. Rev. B*, vol. 96, p. 155120, 2017.

[171] S. S. Jahromi and R. Orús, "Universal tensor-network algorithm for any infinite lattice," *Phys. Rev. B*, vol. 99, p. 195105, 2019.

[172] S. S. Jahromi and R. Orús, "Thermal bosons in 3d optical lattices via tensor networks," *Sci. Rep.*, vol. 10, no. 1, p. 19051, 2020.

[173] M. S. J. Tepaske and D. J. Luitz, "Three-dimensional isometric tensor networks," *Phys. Rev. Res.*, vol. 3, p. 023236, 2021.

[174] T. Picot and D. Poilblanc, "Nematic and supernematic phases in kagome quantum antiferromagnets under the influence of a magnetic field," *Phys. Rev. B*, vol. 91, p. 064415, 2015.

[175] T. Picot, M. Ziegler, R. Orús, and D. Poilblanc, "Spin-S kagome quantum antiferromagnets in a field with tensor networks," *Phys. Rev. B*, vol. 93, p. 060407(R), 2016.

[176] D. Nagaj, E. Farhi, J. Goldstone, P. Shor, and I. Sylvester, "Quantum transverse-field Ising model on an infinite tree from matrix product states," *Phys. Rev. B*, vol. 77, p. 214431, 2008.

[177] A. Nagy, "Simulating quantum systems on the Bethe lattice by translationally invariant infinite-tree tensor network," *Ann. Phys. (N. Y.)*, vol. 327, no. 2, p. 542, 2012.

[178] W. Li, J. von Delft, and T. Xiang, "Efficient simulation of infinite tree tensor network states on the bethe lattice," *Phys. Rev. B*, vol. 86, p. 195137, 2012.

[179] S. Depenbrock and F. Pollmann, "Phase diagram of the isotropic spin-$\frac{3}{2}$ model on the $z = 3$ bethe lattice," *Phys. Rev. B*, vol. 88, p. 035138, 2013.

[180] T. Nishino, K. Okunishi, and M. Kikuchi, "Numerical renormalization group at criticality," *Phys. Lett. A*, vol. 213, no. 1, p. 69, 1996.

[181] P. Hasenfratz and F. Niedermayer, "Finite size and temperature effects in the AF Heisenberg model," *Z. Phys. B*, vol. 92, p. 91, 1993.

[182] A. Albuquerque, F. Alet, P. Corboz, P. Dayal, A. Feiguin, S. Fuchs, L. Gamper, E. Gull, S. Gürtler, A. Honecker, R. Igarashi, M. Körner, A. Kozhevnikov, A. Läuchli, S. Manmana, M. Matsumoto, I. McCulloch, F. Michel, R. Noack, G. Pawłowski, L. Pollet, T. Pruschke, U. Schollwöck, S. Todo, S. Trebst, M. Troyer, P. Werner, and S. Wessel, "The

ALPS project release 1.3: Open-source software for strongly correlated systems," *J. Magn. Magn. Mater.*, vol. 310, no. 2, Part 2, p. 1187, 2007.

[183] B. Bauer, L. D. Carr, H. G. Evertz, A. Feiguin, J. Freire, S. Fuchs, L. Gamper, J. Gukelberger, E. Gull, S. Guertler, A. Hehn, R. Igarashi, S. V. Isakov, D. Koop, P. N. Ma, P. Mates, H. Matsuo, O. Parcollet, G. Pawłowski, J. D. Picon, L. Pollet, E. Santos, V. W. Scarola, U. Schollwöck, C. Silva, B. Surer, S. Todo, S. Trebst, M. Troyer, M. L. Wall, P. Werner, and S. Wessel, "The ALPS project release 2.0: Open source software for strongly correlated systems," *J. Stat. Mech.: Theory Exp.*, vol. 2011, no. 05, p. P05001, 2011.

[184] P. Anders, E. Gull, L. Pollet, M. Troyer, and P. Werner, "Dynamical mean field solution of the Bose-Hubbard model," *Phys. Rev. Lett.*, vol. 105, p. 096402, 2010.

[185] B. Capogrosso-Sansone, N. V. Prokof'ev, and B. V. Svistunov, "Phase diagram and thermodynamics of the three-dimensional Bose-Hubbard model," *Phys. Rev. B*, vol. 75, p. 134302, 2007.

[186] G. Semerjian, M. Tarzia, and F. Zamponi, "Exact solution of the Bose-Hubbard model on the Bethe lattice," *Phys. Rev. B*, vol. 80, p. 014524, 2009.

[187] P. C. G. Vlaar and P. Corboz, "Efficient tensor network algorithm for layered systems," *Phys. Rev. Lett.*, vol. 130, p. 130601, 2023.

[188] R. Coldea, D. A. Tennant, A. M. Tsvelik, and Z. Tylczynski, "Experimental realization of a 2D fractional quantum spin liquid," *Phys. Rev. Lett.*, vol. 86, p. 1335, 2001.

[189] Y. Shimizu, K. Miyagawa, K. Kanoda, M. Maesato, and G. Saito, "Spin liquid state in an organic mott insulator with a triangular lattice," *Phys. Rev. Lett.*, vol. 91, p. 107001, 2003.

[190] R. Rawl, L. Ge, H. Agrawal, Y. Kamiya, C. R. Dela Cruz, N. P. Butch, X. F. Sun, M. Lee, E. S. Choi, J. Oitmaa, C. D. Batista, M. Mourigal, H. D. Zhou, and J. Ma, "$Ba_8CoNb_6O_{24}$: A spin-$\frac{1}{2}$ triangular-lattice Heisenberg antiferromagnet in the two-dimensional limit," *Phys. Rev. B*, vol. 95, p. 060412(R), 2017.

[191] Y. Cui, J. Dai, P. Zhou, P. S. Wang, T. R. Li, W. H. Song, J. C. Wang, L. Ma, Z. Zhang, S. Y. Li, G. M. Luke, B. Normand, T. Xiang, and W. Yu, "Mermin-Wagner physics, (H, T) phase diagram, and candidate quantum spin-liquid phase in the spin-$\frac{1}{2}$ triangular-lattice antiferromagnet $Ba_8CoNb_6O_{24}$," *Phys. Rev. Mater.*, vol. 2, p. 044403, 2018.

[192] H. Kageyama, K. Yoshimura, R. Stern, N. V. Mushnikov, K. Onizuka, M. Kato, K. Kosuge, C. P. Slichter, T. Goto, and Y. Ueda, "Exact dimer ground state and quantized magnetization plateaus in the two-dimensional spin system $SrCu_2(BO_3)_2$," *Phys. Rev. Lett.*, vol. 82, p. 3168, 1999.

[193] S. Miyahara and K. Ueda, "Exact dimer ground state of the two dimensional Heisenberg spin system $SrCu_2(BO_3)_2$," *Phys. Rev. Lett.*, vol. 82, p. 3701, 1999.

[194] Y. Singh and P. Gegenwart, "Antiferromagnetic Mott insulating state in single crystals of the honeycomb lattice material Na_2IrO_3," *Phys. Rev. B*, vol. 82, p. 064412, 2010.

[195] K. W. Plumb, J. P. Clancy, L. J. Sandilands, V. V. Shankar, Y. F. Hu, K. S. Burch, H.-Y. Kee, and Y.-J. Kim, "$\alpha - RuCl_3$: A spin-orbit assisted Mott insulator on a honeycomb lattice," *Phys. Rev. B*, vol. 90, p. 041112, 2014.

[196] C. Wessler, B. Roessli, K. W. Krämer, B. Delley, O. Waldmann, L. Keller, D. Cheptiakov, H. B. Braun, and M. Kenzelmann, "Observation of plaquette fluctuations in the spin-1/2 honeycomb lattice," *npj Quantum Mater.*, vol. 5, no. 1, p. 85, 2020.

[197] P. Sengupta, A. W. Sandvik, and R. R. P. Singh, "Specific heat of quasi-two-dimensional antiferromagnetic Heisenberg models with varying interplanar couplings," *Phys. Rev. B*, vol. 68, p. 094423, 2003.

[198] B. Sriram Shastry and B. Sutherland, "Exact ground state of a quantum mechanical antiferromagnet," *Physica B+C*, vol. 108, no. 1, p. 1069, 1981.

[199] S. Wessel, I. Niesen, J. Stapmanns, B. Normand, F. Mila, P. Corboz, and A. Honecker, "Thermodynamic properties of the Shastry-Sutherland model from quantum Monte Carlo simulations," *Phys. Rev. B*, vol. 98, no. 17, p. 174432, 2018.

[200] G. Vidal, "Entanglement renormalization," *Phys. Rev. Lett.*, vol. 99, p. 220405, 2007.

[201] T. Barthel, C. Pineda, and J. Eisert, "Contraction of fermionic operator circuits and the simulation of strongly correlated fermions," *Phys. Rev. A*, vol. 80, p. 042333, 2009.

[202] Z.-C. Gu, F. Verstraete, and X.-G. Wen, "Grassmann tensor network states and its renormalization for strongly correlated fermionic and bosonic states." arXiv:1004.2563 [cond-mat.str-el], 2010.

[203] C. V. Kraus, N. Schuch, F. Verstraete, and J. I. Cirac, "Fermionic projected entangled pair states," *Phys. Rev. A*, vol. 81, p. 052338, 2010.

[204] P. C. G. Vlaar and P. Corboz, "Tensor network study of the Shastry-Sutherland model with weak interlayer coupling." arXiv:2302.07894 [cond-mat.str-el], 2023.

[205] K. Onizuka, H. Kageyama, Y. Narumi, K. Kindo, Y. Ueda, and T. Goto, "1/3 magnetization plateau in $SrCu_2(BO_3)_2$ - stripe order of excited triplets -," *J. Phys. Soc. Jpn.*, vol. 69, no. 4, p. 1016, 2000.

[206] K. Kodama, M. Takigawa, M. Horvatić, C. Berthier, H. Kageyama, Y. Ueda, S. Miyahara, F. Becca, and F. Mila, "Magnetic superstructure in the two-dimensional quantum antiferromagnet $SrCu_2(BO_3)_2$," *Science*, vol. 298, no. 5592, p. 395, 2002.

[207] M. Takigawa, K. Kodama, M. Horvatić, C. Berthier, H. Kageyama, Y. Ueda, S. Miyahara, F. Becca, and F. Mila, "The 18-magnetization plateau state in the 2D quantum antiferromagnet $SrCu_2(BO_3)_2$: Spin superstructure, phase transition, and spin dynamics studied by high-field NMR," *Phys. B Condens. Matter*, vol. 346-347, p. 27, 2004.

[208] F. Levy, I. Sheikin, C. Berthier, M. Horvatić, M. Takigawa, H. Kageyama, T. Waki, and Y. Ueda, "Field dependence of the quantum ground state in the Shastry-Sutherland system $SrCu_2(BO_3)_2$," *EPL*, vol. 81, no. 6, p. 67004, 2008.

[209] S. E. Sebastian, N. Harrison, P. Sengupta, C. D. Batista, S. Francoual, E. Palm, T. Murphy, N. Marcano, H. A. Dabkowska, and B. D. Gaulin, "Fractalization drives crystalline states in a frustrated spin system," *Proc. Natl. Acad. Sci. U.S.A.*, vol. 105, no. 51, p. 20157, 2008.

[210] M. Jaime, R. Daou, S. A. Crooker, F. Weickert, A. Uchida, A. E. Feiguin, C. D. Batista, H. A. Dabkowska, and B. D. Gaulin, "Magnetostriction and magnetic texture to 100.75 Tesla in frustrated $SrCu_2(BO_3)_2$," *Proc. Natl. Acad. Sci. U.S.A.*, vol. 109, no. 31, p. 12404, 2012.

[211] M. Takigawa, M. Horvatić, T. Waki, S. Krämer, C. Berthier, F. Lévy-Bertrand, I. Sheikin, H. Kageyama, Y. Ueda, and F. Mila, "Incomplete devil's staircase in the magnetization curve of $SrCu_2(BO_3)_2$," *Phys. Rev. Lett.*, vol. 110, p. 067210, 2013.

[212] Y. H. Matsuda, N. Abe, S. Takeyama, H. Kageyama, P. Corboz, A. Honecker, S. R. Manmana, G. R. Foltin, K. P. Schmidt, and F. Mila, "Magnetization of $SrCu_2(BO_3)_2$ in ultrahigh magnetic fields up to 118 T," *Phys. Rev. Lett.*, vol. 111, p. 137204, 2013.

[213] S. Haravifard, D. Graf, A. E. Feiguin, C. D. Batista, J. C. Lang, D. M. Silevitch, G. Srajer, B. D. Gaulin, H. A. Dabkowska, and T. F. Rosenbaum, "Crystallization of spin superlattices with pressure and field in the

layered magnet $SrCu_2(BO_3)_2$," *Nat. Commun.*, vol. 7, no. 1, p. 11956, 2016.

[214] T. Nomura, P. Corboz, A. Miyata, S. Zherlitsyn, Y. Ishii, Y. Kohama, Y. H. Matsuda, A. Ikeda, C. Zhong, H. Kageyama, and F. Mila, "The Shastry-Sutherland compound $SrCu_2(BO_3)_2$ studied up to the saturation magnetic field." arXiv:2209.07652 [cond-mat.str-el], 2022.

[215] T. Momoi and K. Totsuka, "Magnetization plateaus of the Shastry-Sutherland model for $SrCu_2(BO_3)_2$: Spin-density wave, supersolid, and bound states," *Phys. Rev. B*, vol. 62, no. 22, p. 15067, 2000.

[216] Y. Fukumoto, "Magnetization plateaus in the Shastry-Sutherland model for $SrCu_2(BO_3)_2$: Results of fourth-order perturbation expansion with a low-density approximation," *J. Phys. Soc. Jpn.*, vol. 70, no. 5, p. 1397, 2001.

[217] S. Miyahara, F. Becca, and F. Mila, "Theory of spin-density profile and lattice distortion in the magnetization plateaus of $SrCu_2(BO_3)_2$," *Phys. Rev. B*, vol. 68, no. 2, p. 024401, 2003.

[218] J. Dorier, K. P. Schmidt, and F. Mila, "Theory of magnetization plateaux in the Shastry-Sutherland model," *Phys. Rev. Lett.*, vol. 101, no. 25, p. 250402, 2008.

[219] A. Abendschein and S. Capponi, "Effective theory of magnetization plateaux in the Shastry-Sutherland lattice," *Phys. Rev. Lett.*, vol. 101, no. 22, p. 227201, 2008.

[220] D. A. Schneider, K. Coester, F. Mila, and K. P. Schmidt, "Pressure dependence of the magnetization plateaus of $SrCu_2(BO_3)_2$," *Phys. Rev. B*, vol. 93, no. 24, p. 241107, 2016.

[221] T. Waki, K. Arai, M. Takigawa, Y. Saiga, Y. Uwatoko, H. Kageyama, and Y. Ueda, "A novel ordered phase in $SrCu_2(BO_3)_2$ under high pressure," *J. Phys. Soc. Jpn.*, vol. 76, no. 7, p. 073710, 2007.

[222] S. Haravifard, A. Banerjee, J. C. Lang, G. Srajer, D. M. Silevitch, B. D. Gaulin, H. A. Dabkowska, and T. F. Rosenbaum, "Continuous and discontinuous quantum phase transitions in a model two-dimensional magnet," *Proc. Natl. Acad. Sci. U.S.A.*, vol. 109, no. 7, p. 2286, 2012.

[223] M. E. Zayed, C. Rüegg, J. Larrea J., A. M. Läuchli, C. Panagopoulos, S. S. Saxena, M. Ellerby, D. F. McMorrow, T. Strässle, S. Klotz, G. Hamel, R. A. Sadykov, V. Pomjakushin, M. Boehm, M. Jiménez–Ruiz, A. Schneidewind, E. Pomjakushina, M. Stingaciu, K. Conder, and H. M.

Rønnow, "4-spin plaquette singlet state in the Shastry–Sutherland compound $SrCu_2(BO_3)_2$," *Nat. Phys.*, vol. 13, no. 10, p. 962, 2017.

[224] T. Sakurai, Y. Hirao, K. Hijii, S. Okubo, H. Ohta, Y. Uwatoko, K. Kudo, and Y. Koike, "Direct observation of the quantum phase transition of $SrCu_2(BO_3)_2$ by high-pressure and terahertz electron spin resonance," *J. Phys. Soc. Jpn.*, vol. 87, no. 3, p. 033701, 2018.

[225] S. Bettler, L. Stoppel, Z. Yan, S. Gvasaliya, and A. Zheludev, "Sign switching of dimer correlations in $SrCu_2(BO_3)_2$ under hydrostatic pressure," *Phys. Rev. Res.*, vol. 2, p. 012010, 2020.

[226] Z. Shi, S. Dissanayake, P. Corboz, W. Steinhardt, D. Graf, D. M. Silevitch, H. A. Dabkowska, T. F. Rosenbaum, F. Mila, and S. Haravifard, "Discovery of quantum phases in the Shastry-Sutherland compound $SrCu_2(BO_3)_2$ under extreme conditions of field and pressure," *Nat. Commun.*, vol. 13, no. 1, p. 2301, 2022.

[227] Y. Cui, L. Liu, H. Lin, K.-H. Wu, W. Hong, X. Liu, C. Li, Z. Hu, N. Xi, S. Li, R. Yu, A. W. Sandvik, and W. Yu, "Proximate deconfined quantum critical point in $SrCu_2(BO_3)_2$." arXiv:2204.08133 [cond-mat.str-el], 2022.

[228] A. Koga and N. Kawakami, "Quantum phase transitions in the Shastry-Sutherland model for $SrCu_2(BO_3)_2$," *Phys. Rev. Lett.*, vol. 84, p. 4461, 2000.

[229] Y. Takushima, A. Koga, and N. Kawakami, "Competing spin-gap phases in a frustrated quantum spin system in two dimensions," *J. Phys. Soc. Jpn.*, vol. 70, no. 5, p. 1369, 2001.

[230] A. Läuchli, S. Wessel, and M. Sigrist, "Phase diagram of the quadrumerized Shastry-Sutherland model," *Phys. Rev. B*, vol. 66, p. 014401, 2002.

[231] J. Y. Lee, Y.-Z. You, S. Sachdev, and A. Vishwanath, "Signatures of a deconfined phase transition on the Shastry-Sutherland lattice: Applications to quantum critical $SrCu_2(BO_3)_2$," *Phys. Rev. X*, vol. 9, p. 041037, 2019.

[232] A. Keleş and E. Zhao, "Rise and fall of plaquette order in the Shastry-Sutherland magnet revealed by pseudofermion functional renormalization group," *Phys. Rev. B*, vol. 105, p. L041115, 2022.

[233] J. Yang, A. W. Sandvik, and L. Wang, "Quantum criticality and spin liquid phase in the Shastry-Sutherland model," *Phys. Rev. B*, vol. 105, p. L060409, 2022.

[234] G. Radtke, A. Saúl, H. A. Dabkowska, M. B. Salamon, and M. Jaime, "Magnetic nanopantograph in the $SrCu_2(BO_3)_2$ Shastry-Sutherland lattice," *Proc. Natl. Acad. Sci. U.S.A.*, vol. 112, no. 7, p. 1971, 2015.

[235] D. I. Badrtdinov, A. A. Tsirlin, V. V. Mazurenko, and F. Mila, "$SrCu_2(BO_3)_2$ under pressure: A first-principles study," *Phys. Rev. B*, vol. 101, p. 224424, 2020.

[236] C. Boos, S. P. G. Crone, I. A. Niesen, P. Corboz, K. P. Schmidt, and F. Mila, "Competition between intermediate plaquette phases in $SrCu_2(BO_3)_2$ under pressure," *Phys. Rev. B*, vol. 100, p. 140413, 2019.

[237] K. Ueda and S. Miyahara, "A class of Heisenberg models with orthogonal dimer ground states," *J. Phys. Condens. Matter*, vol. 11, no. 17, p. L175, 1999.

[238] S. Miyahara and K. Ueda, "Thermodynamic properties of three-dimensional orthogonal dimer model for $SrCu_2(BO_3)_2$," *J. Phys. Soc. Jpn. Suppl. B.*, vol. 69, p. 72, 2000.

[239] C. Knetter, A. Bühler, E. Müller-Hartmann, and G. S. Uhrig, "Dispersion and symmetry of bound states in the Shastry-Sutherland model," *Phys. Rev. Lett.*, vol. 85, p. 3958, 2000.

[240] M. Moliner, I. Rousochatzakis, and F. Mila, "Emergence of one-dimensional physics from the distorted Shastry-Sutherland lattice," *Phys. Rev. B*, vol. 83, p. 140414, 2011.

[241] I. Hagymási, R. Schäfer, R. Moessner, and D. J. Luitz, "Possible inversion symmetry breaking in the $S = 1/2$ pyrochlore Heisenberg magnet," *Phys. Rev. Lett.*, vol. 126, p. 117204, 2021.

Contributions to publications

Below is an overview of my contributions to the publications that form the basis of this thesis. All the work was performed under supervision and together with dr. P. Corboz.

[1] P. C. G. Vlaar and P. Corboz. *Simulation of three-dimensional quantum systems with projected entangled-pair states,* Phys. Rev. B 103, 205137 (2021) (*Presented in Chapter 3*).

The algorithms were implemented by me. For the incorporation of the $U(1)$-symmetry, I used a library developed by dr. P. Corboz. I performed all the simulations of the Heisenberg and Bose-Hubbard models and wrote a first draft of the paper. The final version of the paper was the result of a collaborative effort between dr. P. Corboz and me.

[2] P. C. G. Vlaar and P. Corboz. *Efficient tensor network algorithm for layered systems,* Phys. Rev. Lett. 130, 130601 (2023) (*Presented in Chapter 4*).

I implemented the algorithms, again using the $U(1)$ symmetry library from dr. P. Corboz. I also performed all the simulations of the anisotropic Heisenberg and the Shastry-Sutherland models, where the initial 2D states for the simulations of the latter model were obtained by dr. P. Corboz. The final paper was a joint effort of dr. P. Corboz and me.

[3] P. C. G. Vlaar and P. Corboz. *Tensor network study of the Shastry-Sutherland model with weak interlayer coupling,* arXiv:2302.07894 [cond-mat.str-el] (2023) (*Presented in Chapter 5*).

All the simulations were performed by me, using initial 2D states provided by dr. P. Corboz. An initial draft for the paper was written by me, which was edited by both dr. P. Corboz and me to create the final version.

Summary

Tensor Network Algorithms for Three-Dimensional Quantum Systems

Understanding the phenomena arising in strongly-correlated quantum systems is one of the key endeavors in modern physics. The interactions in these systems give rise to many types of emerging behavior, such as superconductivity, exotic magnetic phases, and many types of collective excitations. Often the models used to describe these phenomena are too complex to study analytically and we therefore rely on numerical approaches.

Algorithms based on tensor networks constitute an important family of numerical techniques. The most prominent example of a tensor network state is the matrix product state (MPS), which is a one-dimensional wave function ansatz underlying the famous density matrix renormalization group (DMRG) algorithm. It has created substantial advancements in the study of one-dimensional quantum systems. A generalization of the MPS to higher dimensional systems is the projected entangled-pair state (PEPS). Although the algorithms for PEPS are much more involved than for MPS, they have become a successful tool for the study of two-dimensional quantum systems.

Although the power of tensor network methods has been clearly shown in one- and two-dimensional systems, it remains an open question whether they can be applied effectively to three-dimensional quantum systems. Extensions of tensor networks to three dimensions have been relatively unexplored, yet they could provide valuable insight into many open problems, e.g., in frustrated magnetism, ultra-cold atomic systems, and layered two-dimensional materials.

The goal of this thesis is to develop PEPS algorithms to study three-dimensional quantum systems. The main challenge in these algorithms is the evaluation of expectation values which require a contraction of the tensor network. Developing efficient contraction algorithms therefore is an important topic of this thesis. We will make use of infinite projected entangled-pair states (iPEPS), which are a type of PEPS that allow us to directly probe the thermodynamic limit.

In Chap. 3, we study methods to perform iPEPS simulations for general three-dimensional quantum systems. We propose two contraction approaches. The first approach is the cluster contraction. The main idea of this method is to only contract a small number of tensors exactly and to use an effective description for the rest of the tensor network. The main benefit of this approach is the low numerical cost compared to full contractions of the network, although its accuracy does have limitations. The second approach is the SU+CTM contrac-

tion. In this method, we perform a full contraction of the tensor network. The main idea of this algorithm is to first define and optimize a two-dimensional boundary iPEPS, such that the three-dimensional tensor network can be represented by a quasi-two-dimensional one. We can then evaluate this network using the two-dimensional corner transfer matrix renormalization group (CTM) method, which is a standard contraction approach for two-dimensional iPEPS. The SU+CTM method is more accurate than the cluster contraction, but it does have a significantly higher numerical cost. We benchmark the two approaches for the Heisenberg and the Bose-Hubbard models and we find a good agreement with quantum Monte Carlo and bosonic dynamical mean-field theory.

The attention in Chap. 4 shifts to a particular subset of three-dimensional systems that consist of two-dimensional layers with weak coupling between the planes. These systems are widely studied and highly relevant; prominent examples include the cuprate high-T_c superconductors and frustrated magnets on, e.g., triangular, honeycomb, Kagomé, or Shastry-Sutherland lattices. Many studies assume the effect of the interlayer coupling to be negligible such that they can be treated as two-dimensional systems, however the interlayer coupling can play an important role on the quantitative level. This chapter proposes a contraction algorithm for iPEPS, the layered corner transfer matrix renormalization group (LCTM), that allows us to study these systems. In the approach, we decouple the layers away from the center such that they can be contracted using the two-dimensional CTM method. In the center, we keep the layers connected in order to capture the most relevant interlayer correlations. The approach has a significantly lower numerical cost than the SU+CTM approach proposed in Chap. 3 for general three-dimensional iPEPS networks. We assess the accuracy of the approach by studying the anisotropic Heisenberg model, where we find a good agreement with contractions by the SU+CTM method and with quantum Monte Carlo results. We also analyze the dimer to Néel phase transition in the Shastry-Sutherland model (a two-dimensional frustrated spin model describing coupled orthogonal dimers) and show that our results are consistent with a series expansion study.

In Chap. 5, we apply the LCTM method to study the phase diagram of the Shastry-Sutherland model with a weak interlayer coupling in more detail. The model is physically remarkably well realized in the compound $SrCu_2(BO_3)_2$, although discrepancies exist. One of these is that the extent of the plaquette-singlet phase found in experimental studies of $SrCu_2(BO_3)_2$ is significantly smaller than predicted from theoretical studies of the Shastry-Sutherland model. A possible explanation is the effect of the interlayer coupling in the compound. In our study, we perform simulations around the regime relevant to experiments and find that the extent of the plaquette phase decreases quickly already at a weak interlayer coupling. We also obtain an estimate for the interlayer coupling

in $SrCu_2(BO_3)_2$ of $J''/J \sim 0.027$ at ambient pressure.

With this thesis, we hope to show the potential of tensor networks for the accurate study of three-dimensional strongly-correlated quantum systems. There are many ways in which the algorithms can still be improved by performing more accurate contractions and optimizations of the iPEPS ansatz. But already in their current form, tensor networks can be a powerful tool to provide insight into many problems in three-dimensional quantum systems, especially into models that are difficult to study using quantum Monte Carlo due to the negative sign problem.

Samenvatting

Tensornetwerkalgoritmen voor Driedimensionale Kwantumsystemen

Een van de belangrijkste inspanningen in de moderne natuurkunde is het begrijpen van de verschijnselen die zich voordoen in sterk gecorreleerde kwantumsystemen. De interacties in deze systemen zorgen voor een grote variëteit aan emergent gedrag, zoals supergeleiding, exotische magnetische fasen en vele soorten collectieve excitaties. Vaak zijn de modellen die gebruikt worden om deze fenomenen te beschrijven te complex om analytisch te bestuderen waardoor we afhankelijk zijn van numerieke methoden.

Methoden gebaseerd op tensornetwerken vormen een belangrijke groep van numerieke technieken. Het meest bekende voorbeeld van een tensornetwerk *Ansatz* is de *matrix product state* (MPS), een *Ansatz* voor de golffunctie in eendimensionale systemen die ten grondslag ligt aan het bekende *density matrix renormalization group* (DMRG) algoritme. De DMRG-methode heeft geleid tot belangrijke doorbraken in onderzoek naar eendimensionale kwantumsystemen. Een variant van de MPS voor hoger-dimensionale systemen is de *projected entangled-pair state* (PEPS). Hoewel de algoritmen voor PEPS veel complexer zijn dan voor MPS zijn ze een succesvolle methode geworden voor de studie van tweedimensionale kwantumsystemen.

Alhoewel de kracht van tensornetwerkmethoden voor een- en tweedimensionale systemen duidelijk is aangetoond, blijft het een open vraag of ze ook gebruikt kunnen worden voor driedimensionale kwantumsystemen. Toepassingen van tensornetwerken in drie dimensies zijn nog schaars, maar ze hebben wel het potentieel om waardevolle inzichten te verschaffen in veel open vragen, bijvoorbeeld voor gefrustreerde magneten, ultrakoude atomaire systemen en voor materialen die opgebouwd zijn uit tweedimensionale lagen.

Het doel van dit proefschrift is om PEPS-algoritmen te ontwikkelen die deze driedimensionale kwantumsystemen kunnen simuleren. De grootste uitdaging voor deze algoritmen is de berekening van verwachtingswaarden, waarvoor een contractie van het tensornetwerk nodig is. Het ontwikkelen van efficiënte contractie algoritmen is daarom ook een belangrijk onderwerp in dit proefschrift. We maken gebruik van *infinite projected entangled-pair states* (iPEPS), een variant van PEPS waarmee de thermodynamische limiet direct gesimuleerd kan worden.

In hoofdstuk 3 ontwikkelen we methoden om iPEPS-simulaties uit te voeren voor algemene driedimensionale kwantumsystemen. We introduceren twee con-

tractiemethoden. De eerste is de clustercontractie. Het idee van deze methode is om slechts een klein aantal tensors exact samen te trekken en voor de rest van het tensornetwerk een benadering te gebruiken. Deze methode heeft het voordeel dat de numerieke kosten relatief laag zijn in vergelijking met volledige contracties van het netwerk, alhoewel de nauwkeurigheid van de contractie beperkingen heeft. De tweede methode die we voorstellen is de SU+CTM-contractie. Dit algoritme voert een volledige contractie van het tensornetwerk uit. De methode begint door een tweedimensionale iPEPS-rand te definiëren en te optimaliseren, zodat het driedimensionale tensornetwerk gerepresenteerd kan worden door een quasi-tweedimensionaal netwerk. We kunnen dit netwerk vervolgens samentrekken met behulp van de tweedimensionale *corner transfer matrix renormalization group* (CTM) methode, wat een veel gebruikt algoritme is voor tweedimensionale iPEPS-simulaties. De SU+CTM-methode is nauwkeuriger dan de clustercontractie, maar heeft wel aanzienlijk meer rekenkracht nodig. We testen de nauwkeurigheid van de twee methoden door simulaties te doen van het Heisenberg- en het Bose-Hubbard-model en we vinden een goede overeenkomst met kwantum Monte Carlo en *bosonic dynamical mean-field theory*.

De focus verschuift in hoofdstuk 4 naar een subgroep van driedimensionale systemen die bestaan uit tweedimensionale lagen met een zwakke koppeling tussen de lagen. Er wordt veel onderzoek gedaan naar dergelijke systemen; prominente voorbeelden zijn de cupraat hogetemperatuursupergeleiders en gefrustreerde magneten op driehoekige-, honingraat-, Kagomé- of Shastry-Sutherland-roosters. Om de eigenschappen van deze modellen te beschrijven wordt vaak aangenomen dat het effect van de koppeling tussen de lagen verwaarloosbaar klein is, zodat ze als tweedimensionale systemen behandeld kunnen worden. Deze koppeling kan desondanks kwantitatief een belangrijke rol spelen. In dit hoofdstuk introduceren we een contractiealgoritme voor iPEPS waarmee deze systemen bestudeerd kunnen worden, de *layered corner transfer matrix renormalization group* (LCTM). In deze methode ontkoppelen we de lagen overal behalve in het centrum, zodat ze kunnen worden samengetrokken met behulp van de tweedimensionale CTM-methode. In het midden blijven de lagen verbonden zodat de meest relevante correlaties tussen de lagen mee worden genomen. De methode heeft een veel lagere numerieke kosten dan het SU+CTM-algoritme dat in hoofdstuk 3 wordt voorgesteld voor algemene driedimensionale iPEPS-netwerken. We beoordelen de nauwkeurigheid van de methode door simulaties te doen van het anisotrope Heisenberg-model. We vinden een goede overeenkomst met SU+CTM-contracties en met kwantum Monte Carlo-resultaten. We analyseren ook de faseovergang van de dimeer-singlet naar Néel fasen in het Shastry-Sutherland-model (een tweedimensionaal gefrustreerd spinmodel dat gekoppelde orthogonale dimeren beschrijft) en we laten zien dat onze resultaten consistent zijn met een *series expansion* studie.

In hoofdstuk 5 gebruiken we de LCTM-methode om het fasediagram van het Shastry-Sutherland-model met een zwakke koppeling tussen de lagen nader te bestuderen. Het materiaal $SrCu_2(BO_3)_2$ kan opmerkelijk nauwkeurig beschreven worden door dit model, hoewel er afwijkingen zijn. Een van deze afwijkingen is dat de omvang van de plaquette-singlet-fase in experimentele metingen van $SrCu_2(BO_3)_2$ significant kleiner blijkt te zijn dan voorspeld op basis van theoretische studies van het Shastry-Sutherland-model. Een mogelijke verklaring is het effect van de koppeling tussen de lagen in het materiaal. We voeren simulaties uit van het model rond de koppelingen die relevant zijn voor $SrCu_2(BO_3)_2$ en we vinden dat de omvang van de plaquettefase al snel afneemt bij een zwakke koppeling tussen de lagen. We maken ook een schatting van de koppeling tussen de lagen in $SrCu_2(BO_3)_2$ en komen op $J''/J \sim 0,027$ bij atmosferische druk.

Met het werk in dit proefschrift tonen we de potentie van tensornetwerken aan voor de nauwkeurige studie van driedimensionale sterk gecorreleerde kwantumsystemen. Er zijn vele mogelijke manieren waarmee de algoritmen nog verbeterd zouden kunnen worden, in het bijzonder door nauwkeurigere contracties en optimalisaties van de iPEPS-netwerken uit te voeren. Maar ook in hun huidige vorm kunnen tensornetwerken een krachtig hulpmiddel zijn om inzicht te verwerven in veel onbeantwoorde vragen over driedimensionale kwantumsystemen, met name voor modellen die moeilijk te bestuderen zijn met behulp van kwantum Monte Carlo vanwege het negatieve tekenprobleem.

Acknowledgements

In this final section, I would like to thank some people without whom I would not have been able to produce this thesis and who have supported me throughout.

First and most of all, I would like to thank Philippe. It does not feel long ago that I was still a student in your numerics course. It sparked my interest in numerics and was the start of the long journey that would follow over the next five years. Thank you for your enthusiasm, your insights, and your patience. Whenever I ran into a problem I could always walk into your office to discuss and you would invariably come up with creative suggestions to tackle them. I also appreciated it that there was also always space to talk about other things as well. It was not always easy, especially during the pandemic, and without your continuous support and encouragement, this thesis would have looked very different.

Also, thank you to J-S for being my co-promotor and for your insights and useful suggestions during the various meetings we had.

I would also like to thank the other members of the group over the years, Ido, Schelto, Juan, Yining, Sangwoo, Natalia, Matthias, Juraj, and Boris. Thank you for the good atmosphere, the discussions, the useful suggestions, and the fun conversations.

Furthermore, I would like to thank the various people I shared our dark, overcrowded, but cozy office with during the PhD, Daniël, Geert, Yuan, Ward, Alberto, Suvendu, Lieuwe, Karina, and Eric. Bart dK, we started at the same time and have been officemates almost throughout. I will certainly miss your wit and your warm personality. Rebekka, thank you for the open conversations about the upsides and downsides of PhD life.

Also, thanks to the other people, present and former, from the condensed matter group, Jans, Neil, Bart vV, Sergio, Wouter, Jiri, and all the others. It was a pleasure to be part of a group with such diverse, inspiring, and ambitious individuals. Thanks as well to Kareljan, Jasper, and Vladimir for sharing your expertise. Also, thanks to the secretaries for all your help over the years, in particular Astrid and Rose.

Ik wil ook mijn familie en vrienden bedanken. Lieve papa, mama en Elise, dit is het einde van een lange weg die vaak ook voor jullie niet bekend was. Bedankt voor al jullie steun door de jaren heen en dat ik altijd op jullie kon terugvallen. Joyce, Jolijn, Tessa, Colin, Perry, Koen, en Esther bedankt voor alle uitjes en spelletjesmiddagen. Ook wil ik Diko bedanken voor de regelmatige culturele uitstapjes.

And finally, Dat. Thank you for supporting me throughout. The last year of my PhD was not the easiest for me, thank you for always being there. I am very happy that we finally moved into our own apartment together and I am looking forward to starting this new phase of my life with you!